Atomistic Simulation of Dislocation Core Structures in B2 NiAl

by

Zhao-Yang Xie

Dissertation submitted to the faculty of the
Virginia Polytechnic Institute and State University
in partial fulfillment of the requirements for the degree of

DOCTOR OF PHILOSOPHY

in

Materials Engineering Science

APPROVED:

D. Farkas, Chairperson

R. S. Gordon

R. W. Hendricks

W. T. Reynolds Jr.

R. Kriz

A. O. Aning

December, 1993

Blacksburg, Virginia

Atomistic Simulation of Dislocation Core Structures in B2 NiAl

by

Zhao-Yang Xie

Committee Chairperson: D. Farkas

Department of Materials Science and Engineering

(Abstract)

A systematic study of the core structures of ⟨100⟩, ⟨110⟩, and ⟨111⟩ dislocations in B2 NiAl has been conducted using atomistic simulations with an embedded atom method (EAM) potential. New flexible boundary conditions and a new method of graphic representation of dislocation core structure have been employed. The main findings are the following:

Core structures: There are no planar core structures of the dislocations found in B2 NiAl. The core spreading of ⟨100⟩ dislocations in NiAl can occur along a variety of planes depending on dislocation slip plane and line orientation. Discrete lattice effects reduced the high strain levels from anisotropic elasticity solution at the dislocation core considerably and resulted in asymmetrical core structures. The core structure of the ⟨110⟩ dislocations is mutilayered with spreading on the {110} plane. The extent of the same strain level comparing with ⟨100⟩ and ⟨111⟩ dislocations is much larger. The complete ⟨111⟩ dislocations in NiAl are also highly non-planar and are stable with respect to splitting into exact $1/2\langle 111\rangle$ partials as well as to alternative splittings that correspond to the stable fault in the vicinity of the antiphase boundary (APB), in both {110} and {112} planes. *Peierls stresses:* Peierls stresses of the dislocations have been calculated and have been compared for their relative ease of motion. *Local disordering effects:* The local disordering effects on the core structure are found to be significant only in the immediate vicinity of the point defect. *Compositional deviation from stoichiometry:* The simulation results of ⟨100⟩, ⟨110⟩, and ⟨111⟩dislocations in off stoichiometric NiAl show that the core structures became more extended than the ones in the stoichiometric NiAl. The core structures are not only dependent on the overall composition but also on their local atomic arrangement near the core region. When compositional deviation from stoichiometry is introduced, the response to the applied stress is different for the various slip systems. The Peierls stresses for the usually easiest moving ⟨100⟩{110} dislocations increased and for

the $\langle 100 \rangle \{ 100 \}$ dislocations decreased, and the latter are expected to be more active in the deformation processes.

The practical implications of these results are that it seems very difficult to modify the alloy behaviors through local changes in stoichiometry and ordering state. The best way to improve the ductility of B2 NiAl is to stabilize $\langle 111 \rangle$ slip through the addition of alloying elements that can lower the APB energy.

Acknowledgments

One of the most pleasant features of writing this dissertation is the opportunity it presents for acknowledging the assistance and support received during the course of the work leading to the dissertation.

Sincere thanks must go to Dr. Roberto Pasianot who helped me start. Many E-mail communications with him were essential to implement the dipole relaxation in the current simulation codes.

I express my appreciation to Profs. D. Farkas, R. S. Gordon, R. W. Hendricks, W. T. Reynolds Jr., R. Kriz, and A. O. Aning who have served on my committee, to Prof. Farkas, Committee Chair, for her constant support and invaluable advice, to Prof. Gordon, Department Chairman, for the encouragement and motivation through the changes of the Department under his leadership, to Prof. Hendricks for refreshing my knowledge of solid state physics and shocking me by the implementation of a trans-pacific fiber optic communication system (on an exam), and introducing LaTeX as a standard for graduate thesis writing at Virginia Tech (even though I did not use his well-known vpithesis template), to Prof. Reynolds for his always available reference library and for keeping my interests in phase transformation keen, to Prof. Kriz for letting me see beyond three dimensions through visualization, and to Prof. Aning for reminding me the other extreme - making materials totally disordered - when I am working on perfect crystal.

Help from many fellow graduate students are also appreciable. Christophe Vailhe's γ surface calculation provided very useful information, among which two figures have been adapted with little work. Jhewn-Kuang Chen and Chang-Hong Wu were always ready when I fell into a fantastic time-sink trying to figure out how some *free* software worked. Kevin Ternes checked the English in the manuscript to ensure its acceptance to native speakers. The responsibility for any errors or shortcomings is of course entirely mine.

My wife, Yang-Sheng, and my daughter, Sherry, were patient. Their sacrifices were great during this writing effort. I regret my periodic absence from family life, and I will try to make up for the lost time.

Publications

1. Z. Xie and D. Farkas, Core Structures of Dislocations in Off Stoichiometric NiAl and Peierls Stress Calculation, to be submitted to, *Phil. Mag.* (Chapter 6)

2. Z. Xie and D. Farkas, Atomistic Structures and Lattice Effects of Vacancies in Ni-Al Intermetallics, accepted by *J. Mater. Res.* (Chapter 6)

3. R. Pasianot, Z. Xie, D. Farkas, and E. J. Savino, Computer Simulation of the Core Structures of ⟨100⟩ Dislocations in Ordered B2 NiAl, in press, *Modelling and Simulation in Materials Science and Engineering* (Chapter 4)

4. Z. Xie, C. Vailhe, and D. Farkas, Computer Simulation of the Core Structures of Metastable ⟨111⟩ Dislocations in NiAl, *Mater. Sci. Eng. A* **170**, pp. 59-65, 1993 (Chapter 5)

5. R. Pasianot, Z. Xie, D. Farkas, and E. J. Savino, Representation of Atomistic Dislocation Core Structure, *Scripta Met. et Mater*, **28**(3), pp. 319-324, 1993 (Chapter 3)

6. Z. Xie, R. Kriz, and D. Farkas, Visualization of Dislocation Core Structure and Motion in Ordered Alloys, *EPD Congress, 1993*, TMS, 1992, pp. 679-685 (Chapter 3)

7. D. Farkas and Z. Xie, Possibilities of Slip Modification in B2 NiAl, in *High-Temperature Ordered Intermetallic Alloys V*, Eds: I. Baker *et al.*, Proc. Mater. Res. Soc. Symp. vol. 288, 1992, pp.435-441 (Chapter 6)

8. R. Pasianot, E.J. Savino, Z. Xie, and D. Farkas, Simple Flexible Boundary Conditions for the Atomistic Simulation of Dislocation Core Structure and Motion, in *Materials Theory and Modelling*, Eds: P.D. Bristowe *et al.*, Proc. Mater. Res. Soc. Symp. vol. 291, 1992, pp.85-91 (Chapter 2)

9. Z. Xie and D. Farkas, Structure and Energetics of Vacancies , Antisites, and Di-vacancy Complexes in Ni-Al System, in *High-Temperature Ordered Intermetallic Alloys V*, Eds: I. Baker *et al*, Proc. Mater. Res. Soc. Symp. vol. 288, 1992, pp.305-311 (Chapter 6)

Contents

List of Tables

List of Figures

Chapter 1

Introduction

1.1 Properties of the Nickel Aluminium Ordered Alloy

The high strength and low ductility exhibited by ordered intermetallic compounds have been known of since the beginning of the 20th century. The strong tendency for chemical ordering in ordered intermetallics stems from the strong bonding between the dissimilar constituent atoms, which results in high stability of superlattice crystal structures, reduced atomic mobility at elevated temperatures, and reduced dislocation mobility and thus increased resistance to plastic deformation at elevated temperatures. Frequently associated with this intrinsic source of high temperature strength, however, is the inherent brittleness exhibited by polycrystalline ordered intermetallics at room temperature.

The anomalous temperature dependence of yield and flow strengths observed in certain ordered intermetallics of relatively high ordering energy, e.g. Ni_3Al , has been the basis for the superior mechanical properties of modern super alloys. The discovery that the room temperature ductility of Ni_3Al is dramatically improved by a small boron addition and hypostoichiometric deviation [1, 2] renewed interest in ordered intermetallic alloys for high-temperature structural applications. Ordered intermetallic alloys are one of the few classes of materials (with ceramics and composites) that have the potential to be used in demanding structural applications, including many critical components in advanced energy conversion systems for service at elevated temperatures and in hostile environments. For ordered intermetallics to be used at their full potential, however, it is necessary to solve the problems associated with their brittleness. Thus,

much research is needed on the mechanical properties of this important class of materials.

As can be found in recent (1984 - 1993) symposium proceedings and review articles [3, 4, 5, 6, 7, 8, 9], significant advances have occurred in our understanding of the fundamental mechanisms of strength and ductility in ordered intermetallic alloys. There are two principal reasons for the recent advances: (a) state-of-the art experimental techniques and (b) innovative computational methods for theoretical analyses. Some key questions with respect to intrinsic strengthening mechanisms at elevated temperatures and inherent brittleness at various temperatures (such as poor impact resistance at high temperatures) are, however, still not fully resolved. Examination of the past five High Temperature Ordered Intermetallic Alloys proceedings of Materials Research Society (MRS) indicates an active and still growing interest in this field, as can be seen in Fig. 1.1. Fig. 1.1 indicates that the vast majority of work in the past ten years on intermetallics has involved nickel and titanium aluminides. Of these systems the effort on NiAl and TiAl is expanding. Clearly, intermetallic alloys represent a vibrant field research which should continue into the future.

The first recorded reference to the compound NiAl appeared in a phase diagram study published in 1908, where the unusually high melting temperature of this phase was noted. Subsequent research has identified NiAl as an ordered intermetallic material which posesses low density, good oxidation resistance, and metal-like electrical and thermal conductivity. These properties have made NiAl an attractive material for a wide range of engineering applications, including electronic metallizations in advanced semiconductor heterostructures, high temperature environmental coatings, surface catalysts, and high-current vacuum circuit breakers. However, the largest current effort is to understand and develop alloys based on the ordered intermetallic compound NiAl for high temperature applications in advanced aerospace structures and propulsion systems. Significant benefits are anticipated due to the low density, high melting temperature, high thermal conductivity, attractive stiffness, and environmental resistance of NiAl. Extensive research and development [11, 12] has focused on alloying, processing, and microstructural control to modify and improve the mechanical behavior of NiAl for these applications.

In addition to its attractiveness as an engineering material, NiAl also exhibits a range of

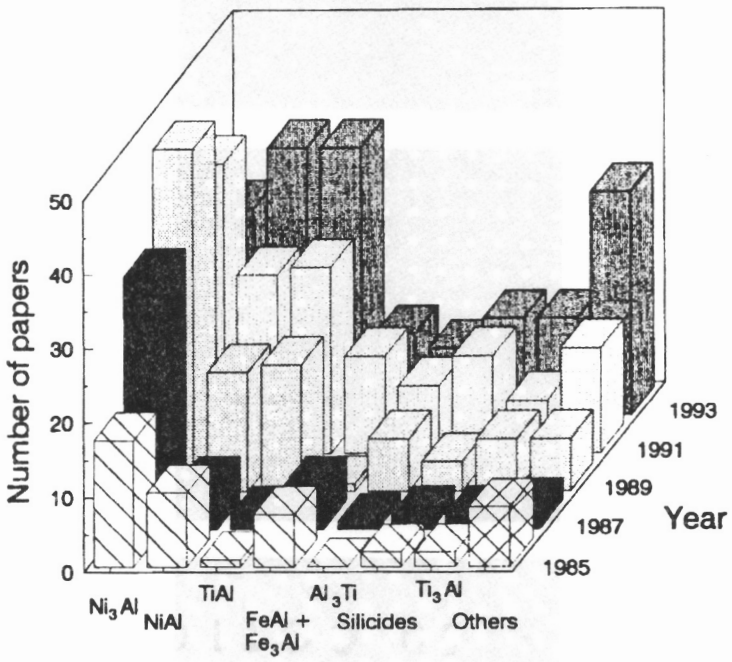

Figure 1.1: Major areas of work on intermetallics as indicated by number of papers published in the five MRS High Temperature Ordered Intermetallic Alloys proceedings [10].

interesting physical characteristics, including a simple crystal structure, a highly ordered lattice, a wide compositional range of stability, a variable defect structure, a reversible shape memory effect, and anisotropic elastic and plastic behavior. These have made NiAl a popular compound for the study of basic scientific phenomena in ordered alloys. The electronic structure of NiAl has been the focus of activity for nearly 25 years, and the results of self-consistent calculations have been compared to measurements of electrical resistivity, optical emissivity, magnetoresistance, and magnetic susceptibility. Interest in the martensitic transformation of Ni-rich NiAl has resulted in a determination of the elastic constants as a function of composition and temperature. The influence of thermal and constitutional vacancies on a broad range of physical and mechanical properties has been addressed. The surface sciences community has identified unusual and unexpected atomic relaxations for low-index surfaces using techniques such as ion scattering, low energy electron diffraction, and scanning tunneling microscopy. The primary slip system in NiAl can be suppressed by control of the orientation in single crystal specimens, and the anisotropic flow behavior and deformation mechanisms have been studied for a wide range of compositions within the single phase field.

The Ni-Al binary equilibrium phase diagram exhibits a wide single phase field, and the stoichiometric composition melts congruently at 1911°K (Figure 1.2) [13]. NiAl possesses the ordered cubic B2 crystal structure (Strukturbericht designation) with space group Pm3m, CsCl prototype (the Pearson symbol cP2), which consists of two interpenetrating primitive cubic cells, where Al atoms occupy the cube conners of one sublattice and Ni atoms occupy the cube conners of the second sublattice. Figure 1.3 shows the crystal structure along with the three important crystallographic directions [100], [110], and [111]. The repetition of the B2 unit cell according to the Bravais lattice produces a perfect ordered NiAl crystal structure. Significant long range order has been observed up to the melting temperature by an investigation of the X -ray intensity of {100} superlattice peaks in single crystals of NiAl, and short-range order has been reported in molten NiAl based on measurements of density and kinematic viscosity [12]. The B2 structure is also stable for large deviations from stoichiometry, and significant long-range order is reported for both Ni-rich and Al-rich compositions. An order-disorder transformation has been suggested to occur in NiAl above 873 K [12], but it is likely that the

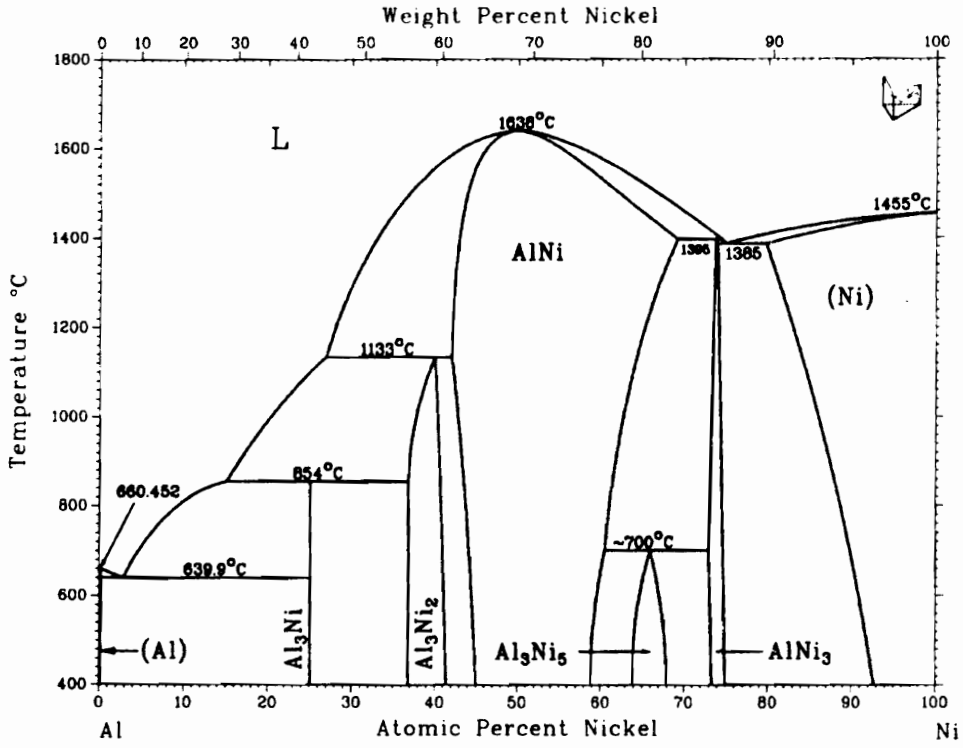

Figure 1.2: The Ni-Al binary phase diagram

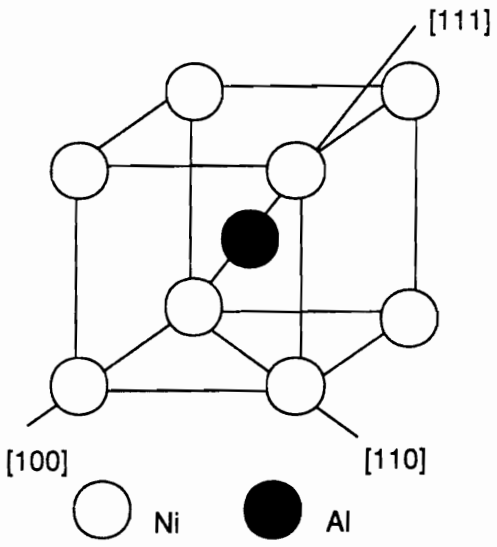

Figure 1.3: The B2 crystal structure.

exothermic peak reported by these authors resulted from the removal of supersaturated vacancies which were quenched in from the homogenization heat treatment. The lattice constant of the stoichiometric composition at room temperature (RT) is 2.887Å.

1.2 Computer Simulation of Defects in Crystalline Solids

Computer-driven atomistic simulation methods are an increasingly important role in the investigation of the structure and properties of materials. For any real system to be studied, researchers normally approach the problem in two ways: one is to do experiments on the real system and come up with experimental results; the other is to make models and construct approximate theory for the model systems, then conclude by making theoretical predictions. Computer simulations play a valuable role in providing essentially exact results for the model systems which would otherwise only be solvable by approximate methods, or might be quite intractable in statistical mechanics. In this sense computer simulation is a test of theories. The results of computer simulation may also be compared with those of real experiments. Eventually, if the model is a good one, the simulator may offer insights to the experimentalist, and assist in the interpretation of new results. Computer simulations actually play a dual role – as a bridge between models and theoretical predictions on one hand, and between models and experimental results on the other. The relationship of experiment, simulation, and theory is shown in Figure 1.4.

The process of carrying out an atomistic calculation are the process that essentially consists of (1) selecting an "appropriate" interaction; (2) setting up the atomic geometry in some initial configuration (typically that predicted by elasticity theory for the given defect); (3) establishing an appropriate boundary condition (such as fixing certain atoms outside the central relaxed region at their initial positions); (4) then iteratively moving the atoms until they reach equilibrium positions (minimizing, for example, total system potential energy, or until the maximum net force on any atom is sufficiently small), for static solutions, or, for dynamic solutions, following the atomic position changes. The forth step entails 3N coupled nonlinear equations (corresponding to the equation of motion for the N atoms being relaxed in 3D space) and may be solved by any of an assortment of numerical techniques (Newton-Raphson,

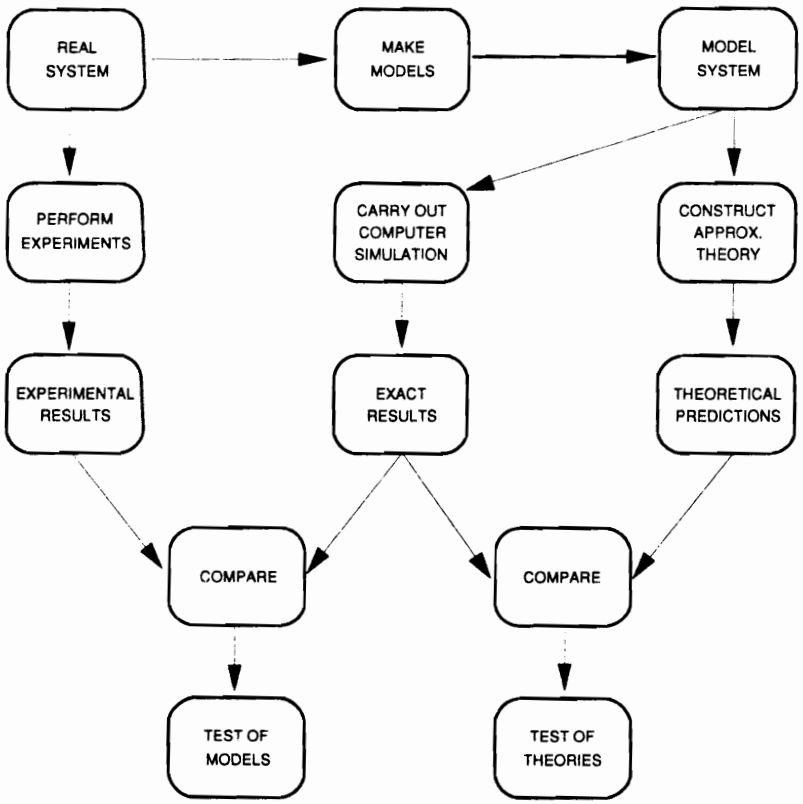

Figure 1.4: The connection between experiment, computer simulation, and theory.

conjugate gradient, etc.).

The entire simulation process involves the minimization of the system energy. Interatomic potentials play a crucial role in the simulation. The validity of the interatomic potentials actually determines the validity of the final configuration. The statement "we could model that for you if we only had an accurate interatomic potential for that material" has been around for many years in the materials community amongst those who are theoretically or numerically inclined.

1.2.1 Interatomic Potentials

The general requirements for an interatomic potential are that it be both accurate enough to permit a broad range of experiments with a reasonable expectation that the results will be physically meaningful, and simple enough to do so within the computer budget. For atomistic calculation, a mathematical model is simply an equation of all of the atoms for a given atomic arrangement so that the energy can be computed. In practice, it is normally only the difference in energy between two sets of atomic positions, or configurations, that is of interest, which leads to considerable simplifications in the calculations.

A first principal treatment of the interatomic potentials of the systems to be studied here (up to 8000 atoms) is unrealistic even for today's fastest computers. Instead simplified models for the interatomic interaction are employed. The description of the interaction (or potential) can have very different origins. The potential can be derived completely from theoretical considerations, with very little input of empirical data. It can be semi-empirical: the functional form is based on theoretical concepts and is parameterized to reproduce experimental observations. Thirdly, the potential can be fully empirical in the sense that it has been fit to a large number of experimental parameters. Some of the experimental parameters that can be used for fitting are: cohesive energy, elastic constants, planar fault energies, vacancy formation energy, etc.

For metallic systems, the traditional approach has been to use pairwise potentials [14], either fitted empirically to bulk thermodynamic data or derived from pseudopotentials. Pairwise potentials describe the energy of an atom as the sum of the interaction energies of the atom with its neighbors. The value of the interaction energy depends only on the distance between

two atoms. Unless the anisotropic elastic constants in a cubic crystal satisfy the Cauchy relation C12= C44, the crystal cannot be correctly described by an equilibrium central pair potential model alone. It can be remedied by the addition of an energy term that depends explicitly on the volume of the system [15]. The physical basis of this volume dependent term is attributable to the background electron gas in which the ions are embedded. The electron density that each ion senses is dependent on the volume of the crystal. However, this approach is implemented by deriving (or fitting) a pair potential for a particular volume, so that simulations are valid only for a particular density of the system; deviations from this density require a different pair potential. This type of potential is acceptable if the density fluctuations in the simulation are small, but it is clearly inappropriate for defects such as vacancy clusters, crack tips, or free surfaces, and dislocations since the different atoms sense very different "volumes". This presents a problem, since many important physical processes take place in these defective regions.

A practical solution to this problem has recently been presented by Daw and Baskes [15]. They proposed writing the energy of the system as a pairwise potential plus a term for each atom (the "embedding energy") that is a function of the local electron density that the atom senses due to nearby atoms. Simulation results using these potentials show dramatic improvement over pair potentials, with only about twice the computational effort. In essence, the embedding energy provides a local "volume" term for each atom, so that large variations in local atom density can be described accurately.

Using an approach similar to the embedded atom method, potentials have been fit to a number of fcc metals. Voter and Chen [16] have presented an alternative parameterization which differs from previous methods primarily in the use of an attractive pairwise interaction and the incorporation of properties of the diatomic molecule in the empirical fit. A potential for the $L1_2$ ordered alloy Ni_3Al was developed by Voter and Chen [16], consisting of potentials for fcc Ni and Al, along with an appropriate Ni-Al cross potential. These potentials have been used extensively to simulate grain boundaries and relaxed surface structures. The following outlines the development of these potentials.

In the embedded atom approach, the energy of an n-particle homonuclear system is written

as

$$E = \frac{1}{2} \sum_{i,j(i \neq j)}^{n} \phi(r_{ij}) + \sum_{i}^{n} F(\bar{\rho}_i) \tag{1.1}$$

where r_{ij} is the distance between atom i and j, ϕ is a pairwise potential, F is the embedding function, and $\bar{\rho}_i$ is the density at atom i due to all its neighbors,

$$\bar{\rho}_i = \sum_{j \neq i}^{n} \rho(r_{ij}). \tag{1.2}$$

The pairwise potential is taken to be a Morse potential,

$$\phi(r) = D_M\{1 - \exp[-\alpha_M(r - R_M)]\}^2 - D_M \tag{1.3}$$

The three parameters, D_M, R_M, and α_M, define the depth, distance to the minimum, and a measure of the curvature near the minimum, respectively. The density function, $\rho(r)$, is taken as

$$\rho(r) = r^6[e^{-\beta r} + 2^9 e^{-2\beta}], \tag{1.4}$$

where β is an adjustable parameter. This was chosen for describing first row transition metals in periodic table, but was found to work well for a number of fcc metals. It has been shown that the cohesive energy of most metals can be scaled to a simple universal function, which is known as Rose's equation of state [16]

$$E_U(a^*) = -E_0(1 + a^*)e^{-a^*}, \tag{1.5}$$

where a^* is a reduced distance variable and E_0 is the depth of the function at the minimum ($a^* = 0$). $F(\bar{\rho})$ is specified by requiring that the energy of the fcc crystal obey Eq. 1.5 as the lattice constant is varied. The appropriate scaling is obtained by taking E_0 as the equilibrium cohesive energy of the solid (E_{coh}), and defining a^* by

$$a^* = (a/a_0 - 1)/(E_{coh}/9B\Omega)^{1/2}, \tag{1.6}$$

where a is the lattice constant, a_0 is the equilibrium lattice constant, B is the bulk modulus, and Ω is the equilibrium atomic volume. Knowing E_{coh}, a_0, B, the embedding function is defined requiring that the energy of the crystal match the energy equations from Eq. 1.5 and Eq. 1.1 for all values of a^*. By fitting $F(\bar{\rho})$ in this way, the potential is appropriate for a large range of densities. Note that because a^* cannot be expressed neatly as a function of $\bar{\rho}$, the construction of $F(\bar{\rho})$ is performed numerically once $\phi(r)$ and $\rho(r)$ are known.

In order to use this potential in molecular dynamics and molecular statics simulations, all the functions and their first derivatives with respect to the nuclear coordinates, should be continuous. As a consequence, these functions are forced to decrease smoothly to zero at a cutoff distance, r_{cut} , which is used as a parameter in the fitting procedure. In this way, the potential always gives a perfect fit to the experimental values of E_{coh}, a_0, and B for any choice of the other functions. Having specified the functional forms for $F(\bar{\rho})$, $\phi(r)$, and $\rho(r)$, the remaining five parameters, $R_M, D_M, \alpha_M, \beta, a$, and r_{cut} are determined by considering that h.c.p. and b.c.c. crystal structures are less stable than f.c.c. and by minimizing the deviation between the calculated and the experimental values of the following : the three cubic elastic constants, the vacancy formation energy, the bond length and the bond energy of the diatomic molecule.

For an alloy system, Eq. 1.1 is replaced as

$$E = \frac{1}{2} \sum_{i,j i \neq j}^{n} \phi_{t_i,t_j}(r_{ij}) + \sum_{j(\neq i)}^{n} F_{t_j}(\bar{\rho}_i)$$

$$\bar{\rho}_i = \sum_{j \neq i}^{n} \rho_{t_j}(r_{ij}) \tag{1.7}$$

where the subscripts t_i and t_j indicate atom types. For the binary Ni-Al alloy, the functions $\phi_{NiNi}, \phi_{NiAl}, \phi_{AlAl}, \rho_{Ni}, F_{Ni}$andF$_{\text{Al}}$ are needed. All of these except ϕ_{NiAl} are known from the pure Ni, Al fits. Inspection of Eq. 1.1 shows that the energy of pure metal is invariant with respect to scaling of ρ, if $F(\bar{\rho})$ is modified correspondingly. However, the energy of the alloy system is not invariant to this scaling, so that scaling factor $s_{Ni(Al)}$ can be optimized in the alloy fit without affecting the single component potentials. The invariance to the addition of a linear term to $F(\bar{\rho})$ gives two more fitting parameters $g_{Ni(Al)}$. Assuming a

Morse potential with variable cutoff distance for $\phi_{NiAl}(r)$, there are a total of seven parameters (D_M, R_M, α_M, r_{cut}, s_{Ni}, g_{Ni}, andg_{Al}) to be optimized in the fit to measured alloy properties. All these parameters are fitted to the Ni_3Al lattice constant, cohesive energy, elastic constants (C11, C12 and C44), ordering energy, vacancy formation energy (ΔE^f_{1v}), (111) and (100) antiphase boundary (APB) energies, the super intrinsic stacking fault (SISF) energy, and the lattice constant and cohesive energy of B2 phase NiAl as shown in Table 1.1. Table 1.2 shows the potential parameters optimized from the fit to experimental data. The overall potential is appropriate for diatomic Ni, diatomic Al, fcc Ni, fcc Al, Ni3Al and B2 NiAl.

The actual potentials used in our simulation were provided by Voter and Chen, and were tabulated into seven tables corresponding to ϕ_{NiNi}, ϕ_{NiAl}, ϕ_{AlAl}, ρ_{Ni}, ρ_{Al}, F_{Ni} and F_{Al}. The interactions of each atom with its neighbors were evaluated within the potential cutoff distance by the subroutine of energy calculation which checks the atom type, the distance between neighboring atoms, then returns the numerical values from potential tables. The total energy of system is obtained through Eqn. 1.7. In this work, Voter and Chen's Ni-Al potentials have been employed throughout.

1.2.2 Simulation Technique

Energy minimization of a system of N atoms would in principle imply the detection of the absolute minimum, taking into account the appropriate, boundary conditions, of the function $E(r_1, r_2, ..., r_N)$, the energy in the 3N-dimensional coordinate space. In the context of defect calculations, this process is also called relaxation. In practice, this problem cannot be solved for most systems, and approximate methods are used. There is of course a choice of several well tried approaches [17]. These methods divide into three main groups (1) those which evaluate only the function itself (search procedures), (2) those which also evaluate the first derivatives of the function (e.g. steepest descents, conjugate gradient method), and (3) those which evaluate second derivatives as well (variable metric or modified Newton-Raphson methods).

In the simplest search procedure one seeks the minimum of the energy function by a cycle of linear searches in the variables of the problem, $r_1, ..., r_N$. This is equivalent to the successive relaxation of equivalent shells of atoms as applied to point defect studies. However the

Table 1.1: Metal properties used by Voter and Chen to fit the Ni-Al potential.

Ni_3Al properties	expt.	calc.
a_o(Å)	3.567[a]	3.573
E_{coh}(eV)	4.57[b]	4.59
$C_{11}(10^{12}erg/cm^3)$	2.30[c]	2.46
$C_{12}(10^{12}erg/cm^3)$	1.50[c]	1.37
$C_{44}(10^{12}erg/cm^3)$	1.31[c]	1.23
ΔE^f_{1v} (eV)	1.6·0.2[d]	1.64(Ni), 1.87(Al)
SISF(111) (mJ/m^2)	10·5[e]	13
APB(100) (mJ/m^2)	140·14[e]	83
APB(111) (mJ/m^2)	180·30[e]	142
B2 NiAl properties		
a_o(Å)	2.88[f]	2.87
E_{coh}(eV)	4.51[b]	4.38

Table 1.2: Potential parameters optimized by Voter and Chen from the fit to experimental data.

	Ni	Al	Ni-Al	
D_M(eV)	1.5335	3.7760	3.0322	s_{Al} = 0.61723
R_M(Å)	2.2053	2.1176	2.0896	g_{Ni} = 6.5145 eV Å^3
α_M(Å^{-1})	1.7728	1.4859	1.6277	g_{Al} = -0.2205 eV Å^3
r_{cut}(Å)	4.7895	5.5550	5.4639	
β(Å^{-1})	3.6408	3.3232		

convergence of this method is known to be unsatisfactory, although in the present application computation times can be reduced (N/2 times) by not evaluating the total energy function at each step but only that part involving the shell of atoms being relaxed. Various improvements of this direct search procedure have been developed, of which the most widely used is probably that of Powell [18]. The general idea here is that of a linear transformation to new variables at the end of each cycle which by incorporating the results of that cycle defines new "less strongly coupled" variables. This "conjugate direction" method retains the advantage of not requiring derivatives, but converges satisfactorily. Even so the required number of evaluations of the energy increases as the square of the number of variables, N, therefore, these search procedures are convenient for small scale simulations.

Methods which utilize derivatives of the energy function, i.e. the forces on the atoms, in general converge faster than search methods, the number of iterations being reduced by a factor N. The calculation of the function's derivatives at any point specifies a local optimum direction of search. The choice of a suitable step length in this direction may be made according to several criteria. Thus a linear search may be made to minimize the energy and the various shells of atoms may be relaxed independently or collectively when the method is simply the application of the method of steepest descent. Alternatively, the problem may be related to molecular dynamics. Bullough and co-workers [18] used the calculated forces to solve the Newtonian equations of motion for the atoms in the relaxed region and then quenched out the kinetic energy as it passed through a maximum. This method is claimed to have the advantage of avoiding local minima (i.e. metastable configurations) but it is not clear that in this it is demonstrably better than other gradient methods. In this method, the step length is related to the time step chosen in the iterative solution of the Newtonian equations and this may be chosen to improve convergence. They have the advantage of requiring relatively little storage.

It is known, however, that the convergence of the regular steepest descent method is poor and it is also well established in general that it is possible to gain substantially improved convergence within the limitations of this class of methods using the conjugate gradient method suggested by Fletcher and Reeves [17]. It has apparent advantages in circumstances where a large store is not available. This has been implemented by Norgett, Perrin and Savino [19] to

defect problems. It has been known that the conjugate gradient method is the most efficient method for the lattice statics calculations.

Variable metric method derived from the Newton-Raphson method differs from the conjugate gradient in the way that it stores and updates the information that is accumulated [17]. Instead of requiring intermediate storage on the order N, the number of dimensions, it requires a matrix of size $N \times N$. Generally for any moderate N, this is an entirely trivial disadvantage. For a crystal lattice involving pairwise interactions, Hessian matrix, the inverse of second derivatives, can be simplified by a technique proposed by Lidiard and Norgett considering each second derivative involves only one pair of atoms. For the case beyond pairwise potentials, the calculation and inversion of the matrix of second derivatives is far too time consuming. On the other hand, there are no overwhelming advantages that the variable metric methods hold over the conjugate gradient techniques, except perhaps a historical one [17].

In our computer simulations, a conjugate gradient method is applied. The computer simulation codes used in this study are based on the original DEVIL code developed by Norgett, Perrin and Savino in 1972 [19]. Every atom in the three dimensional simulation interacts with all its neighbors. These interactions are described by the embedded atom method interatomic potentials. The total energy of the crystal is the sum of the atomic interactions. Starting with a well chosen initial configuration, the energy minimum was reached in an iteration process. The presence of the defect induces forces on the atoms which are allowed to move in order to drive the system to a new equilibrium configuration corresponding to a minimum in the energy of the defect lattice. In a single iteration step, the resultant force from its neighbors on every atom was calculated and after that each atom was displaced in the direction of the force. The energy is computed at each iteration. The new configuration of the energy computation is defined according to the conjugate gradient method. The gradient of the energy function indicates the direction of steepest descent. This is the direction in which the rate of energy decrease is maximum. Between two steps, the atoms are moved in the direction for which the energy decrease is maximum. The following displacements are limited to the directions perpendicular to the previous move. When the forces on each atom are below a small specified value or after a certain number of iterations, the iteration was considered to be complete. At

this point the system was considered to be in equilibrium. The number of iterations required to reach equilibrium varied from several tens to several hundreds.

1.3 Dissertation Organization

This work presents an atomistic study of the core structure of dislocations in B2 NiAl. The entire research proceeds as a sequence of simulation-representation-interpretation.

There are two kinds of boundary conditions in lattice statics (that is, rigid versus flexible). Although the relaxed atomic region can be very large with modern computing capacity, the rigid boundary condition still remains a question. If a yield stress is sought, then the back stress from a rigid boundary can overwhelm and mask the true stress for dislocation motion. An improved boundary condition was developed by Pasianot *et al.* [20] and is described in Chapter 2.

Since the existence of periodicity along dislocation line, the actual representation of dislocation core reduces to a two dimensional problem. The most popular method is the differential displacement maps as proposed by Vitek *et al.* [21]. Their method is convenient for simple dislocations, for complex dislocations it is very difficult to identify the crystallographic planes in which the dislocation core spreads. A method using strain invariants to represent the core structure is introduced in Chapter 3.

Results of core structures of dislocations with Burgers vectors $\langle 100 \rangle$, $\langle 110 \rangle$, and $\langle 111 \rangle$ are presented in Chapter 4 and Chapter 5. The core structure and slip characteristics are affected substantially by local disorder such as vacancy, antisite defects at the core range and by alloy stoichiometry. Chapter 6 contributes on these subjects. Finally, Chapter 7 is a summary which correlates core structures and Peierls stresses and attempts to provide insight as to how the core structure influences the mechanical properties of B2 NiAl.

Chapter 2

Simulation Methods*

2.1 Boundary Conditions

Boundary conditions play essential roles in the calculation of extended defects because of the restriction of computer time and storage. An inherent difficulty in boundary conditions is the proper description of the transition from the lattice to the continuum. Two types of boundary conditions have been devised in the literature: rigid and flexible. In the first class, atoms far away from the dislocation core and surrounding it (the boundary atoms) are held fixed at the atomic positions given by elasticity theory, while the core atoms move independently such as to minimize the potential energy of the simulation block. For the second class, the geometrical description is the same but particular recipes are applied to relax mismatch forces between core atoms and boundary atoms.

Fixed codes generally require bigger atomic arrays (and consequently more computing time) than flexible codes. This is specially true for studies of dislocation motion under stress; a small simulation block for a fixed code may hinder motion or give a roughly overestimated value for the Peierls stress. Besides, flexible codes are better suited to describe core non-linear effects such as volume expansion and dislocation climb.

Flexible boundary codes for the atomistic simulation of dislocations and other defects have

*Based on "Simple Flexible Boundary Conditions for the Atomistic Simulation of Dislocation Core Structure and Motion" by R. Pasianot, E.J. Savino, Z. Xie, and D. Farkas, in *Materials Theory and Modelling*, Eds: P.D. Bristowe et al, Proc. Mater. Res. Soc. Symp. vol. 291, 1992, pp.85-91. The codes used in the present simulation were mainly developed by R. Pasianot

been developed in the past mainly by Sinclair [22], Gehlen et at. [23], and Sinclair et al. [24]. Green functions (continuum or discrete) or surface traction forces were used to relax the boundary atoms. A much simpler approach is followed here. Core and mobility effects at the boundary are accounted for by a dipole tensor centered at the dislocation line, whose components constitute six more parameters of the minimization process.

The initial atomic geometry in the computer simulation of dislocation is typically that predicted by elasticity theory for a given dislocation. Therefore, the calculation of elastic field of a straight dislocation in anisotropic crystalline solids is necessary for the simulation. Recent progress has led to better organization of the elasticity problem for such calculations. The Stroh theory [25] gives a better description of the elastic field of straight dislocation in anisotropic materials. However, the theory is formally based on the premise that there is no external force or constant force at the dislocation core. When the mobility under external applied stress is considered, the situation becomes serious and un-realistic critical stress could be obtained.

The general method for finding the elastic solution is similar to the multipole expansion method in electrostatics. Generally the solutions of the response of resource function $\bar{u}(r)$ to a force source $f(r')$ are

$$\bar{u}(r) = \oint G(r, r') f(r') dr' \tag{2.1}$$

where $G(r, r')$ is Green function.

We first begin with the Stroh theory considering the existence of a force distribution around the core. Then, by introducing the dipole moment tensor, a closed form of solution is obtained, which provides an improved basis for theoretical treatment. After incorporating the solution into the statics simulation code DEVIL [19], a comparison of the simulation results for simple dislocation is followed.

For the sake of consistency with the literature, the customary notation is used here[26]. The objective is to find the elastic field $\bar{u}$ at a point far from the origin of the coordinate system due to a force distribution in the neighborhood of the origin. Sinclair, in an elegant investigation [22], considered the general result for the elastic field in a hollow cylindrical region of continuous and anisotropic matter. According to Eshelby et al. [27], this field is

given by

$$\bar{u} = \sum_{\alpha=1}^{6} \bar{A}_\alpha f_\alpha(z_\alpha) \tag{2.2}$$

where

$$f_\alpha(z_\alpha) = \frac{D_\alpha}{\pm 2\pi i} \ln(z_\alpha) + \sum_{m=-\infty}^{\infty} C_{\alpha n} z_\alpha^n \tag{2.3}$$

and

$$z_\alpha = x_1 + p_\alpha x_2 \tag{2.4}$$

$\bar{A}_\alpha$ are complex vectors depending on the elastic constants and the cylinder axis orientation, p_α are the roots of the so called "sextic equation", x_1, and x_2 are the cartesian coordinates of the point considered (perpendicular to the cylinder axis) D_α and $C_{\alpha n}$ are complex numbers determined to satisfy boundary conditions. As a convention, numbers with sub-index α are present in complex conjugate pairs. Finally, the + (-) sign in Eq. 2.3 is used when $Im(p_\alpha) > 0 (Im(p_\alpha) < 0)$.

The first term in Eq. 2.3 is named "Volterra field", it defines the dislocation as a defect with a discontinuity of a Burgers vector in its elastic field; the second term may be called "core field" and it provides the freedom needed to satisfy additional boundary conditions at the inner and outer surfaces of the cylindrical region. Sinclair's approach was to consider the coefficients of the negative powers in the core field, as parameters of the displacement field of the boundary atoms. They were included as variables of the energy minimization process, and determined such as to get null forces across the boundary region. At about the same time, Gehlen and co-workers [23] proposed a different approach. They treat the mismatch forces between core and boundary atoms, as traction forces applied on a hollow cylinder of circular cross-section. A standard elastic solution for this problem was used to adjust the positions of the boundary atoms. Later, an even more sophisticated procedure was developed by Sinclair et al. [24]. In this case, mismatch forces were relaxed by applying Green functions (continuous and discrete, isotropic or anisotropic) appropriate for line-forces.

Here, we develop a method based on Eqs. 2.2 and 2.3 for the elastic response of the simulated lattice outside the core region, in which the core field is interrupted at the first term (n = -1). In the next section, we show that the resulting field corresponds to the Volterra solution

plus a line of dipole forces at the origin. The six components of the dipole strength are obtained through the energy minimization process, and a consistent solution for the displacements of the boundary atoms is applied.

In addition to the simplicity of the approach, it reasonably accounts for the non-linear contributions to the dislocation field on one side, and allows for a consistent calculation of the lattice intrinsic (Peierls) energy barrier for dislocation motion on the other. As a by-product of this analysis we obtain a relationship between the dislocation line position and the values of the dipole strength, which is of great help in the atomistic simulations that involve the application of stress. Finally, as an example, the case of [100] edge dislocations in NiAl, with and without applied shear stress, is treated.

2.2 Dipole Moments

In this section we follow Stroh's formalism for straight dislocations in anisotropic continuous media [25], as presented in the book by Hirth and Lothe [26]. In this formalism, the elastic field of a dislocation which is acted upon by a line-force is given as

$$\bar{u} = \frac{1}{2\pi i} \sum_{\alpha=1}^{6} \bar{A}_\alpha D_\alpha \ln z_\alpha \tag{2.5}$$

where

$$\pm \sum_{\alpha=1}^{6} \bar{A}_\alpha D_\alpha = \bar{b} \tag{2.6}$$

$$\pm \sum_{\alpha=1}^{6} \bar{L}_\alpha D_\alpha = -\bar{f} \tag{2.7}$$

The last two equations indicate that the Burgers circuit has a discontinuity b and that there is an external force f per unit length along the core. From these two equations, it can be determined that

$$D_\alpha = \pm\{\bar{L}_\alpha \cdot \bar{b} - \bar{A}_\alpha \cdot \bar{f}\} \tag{2.8}$$

and

$$z_\alpha = \bar{x} \cdot (\bar{x}_1 + p_\alpha \bar{x}_2) \tag{2.9}$$

$\bar{f}$ is the line-force, $\bar{x}_1$, and $\bar{x}_2$ are unit vectors perpendicular to each other and to the dislocation line ($\bar{x}_3$). L_α are complex vectors that depend on the elastic constants and line orientation. A_α and p_α have the same meaning as in Eqs. 2.2 to 2.4. Positive sign + corresponds to $Imp_\alpha > 0$; − to $Imp_\alpha < 0$.

Numbering α = 1, 2, 3 for $Imp_\alpha > 0$ and 4, 5, 6, for $Imp_\alpha < 0$, and remembering they are complex conjugate numbers respectively, Eq. 2.5 can be written as

$$\bar{u}(\bar{x}) = \bar{u}_v(\bar{x}) + \bar{u}_c(\bar{x}) \tag{2.10}$$

where

$$\bar{u}_v = \frac{1}{\pi} Im\{\sum_{\alpha=1}^{3} (\bar{L}_\alpha \cdot \bar{b}) \bar{A}_\alpha \ln \eta_\alpha\} \tag{2.11}$$

$$\bar{u}_c = -\frac{1}{\pi} Im\{\sum_{\alpha=1}^{3} (\bar{A}_\alpha \cdot \bar{f}) \bar{A}_\alpha \ln \eta_\alpha\} \tag{2.12}$$

$\bar{u}_v$ and $\bar{u}_c$ will be identified, respectively, as the Volterra and core fields mentioned before.

If $\bar{u}_c$ is due to a line-force distribution over the core area, Eq. 2.12 is replaced by the following

$$\bar{u}_c = -\frac{1}{\pi} Im\{\sum_{\alpha=1}^{3} (\frac{\bar{A}_\alpha}{z_\alpha(\bar{x})} [\bar{A}_\alpha \cdot \bar{\bar{\lambda}} \cdot (\bar{x}_1 + p_\alpha \bar{x}_2)]\} \tag{2.13}$$

where the dipole strength tensor, $\bar{\bar{\lambda}}$, is given by the following surface integral extended to the core vicinity

$$\lambda_{ij} \equiv \int f_i(\bar{x}) x_j d^2 \bar{x} \tag{2.14}$$

The matrix representation of this tensor in the coordinate system $(\bar{x}_1, \bar{x}_2, \bar{x}_3)$ is given by six real numbers according to

$$\bar{\bar{\lambda}} = \begin{pmatrix} \lambda_{11} & \lambda_{12} & 0 \\ \lambda_{21} & \lambda_{22} & 0 \\ \lambda_{31} & \lambda_{32} & 0 \end{pmatrix} \tag{2.15}$$

The above form is completely general; if there are symmetry conditions present, the number of null elements may increase.

We note that u_c must be identical to the 1/z powers in the core field of Eq. 2.2. The

latter terms depend on three complex numbers $C_{1,-1}$, $C_{2,-1}$, and $C_{3,-1}$, that can be put in a one-to-one correspondence with the six real numbers of the present formulation. Therefore, the 1/z powers in the core field can always be represented by a dipole moment tensor centered at the dislocation line.

When the origin of the dislocation Volterra field is shifted by a small distance, $\delta\bar{x}$, the argument of the logarithmic term, z_α, changes by $z_\alpha - \delta z_\alpha$, with $\delta z_\alpha = \delta x_1 + p_\alpha \delta x_2$. Assuming $|\delta z_\alpha| \ll |z_\alpha|$, this procedure introduces terms of the type 1/z and therefore gives rise to the corresponding dipole moments. The linking relation is

$$-(\bar{L}_\alpha \cdot \bar{b})(\delta x_1 + p_\alpha \delta x_2) = \bar{A}_\alpha \cdot \bar{\bar{\lambda}} \cdot (\bar{x}_1 + p_\alpha \bar{x}_2) \tag{2.16}$$

Therefore, the resulting dipole tensor strength has two contributions: one due to a shift of the Volterra field from a minimum lattice energy configuration, solved in Eq. 2.16; and the second due to anharmonic atomic displacements at the dislocation core. If this second contribution is calculated for a configuration free of stress, Eq. 2.16 can be used to deduce the dislocation displacement under stress and, therefore, give a Peierls-type representation of the energy barrier for dislocation motion.

2.3 Geometrical Setup in the Simulation

The computer simulations of dislocation cores were performed following the same procedure in Ref. [19]. The sense vector of the dislocation was always aligned along the z-axis with periodic boundary conditions along this axis. A cylindrical region with a diameter of 10 nm was constructed in the x-y plane and the atoms in this region were displaced from their equilibrium (perfect lattice) positions as given by the anisotropic elasticity theory for the given Burgers vector, line direction and slip plane normal. In the present method the model system is divided into several regions as shown in Figure 2.1. Each atom mantle has at least a width of the interatomic potential range so that the atoms in one region only interact with the atoms in the nearest neighbor regions. The atoms in region I are allowed to move according to their cartesian coordinates $\{\bar{x}\}$, whereas the positions of the atoms in region II are arranged through

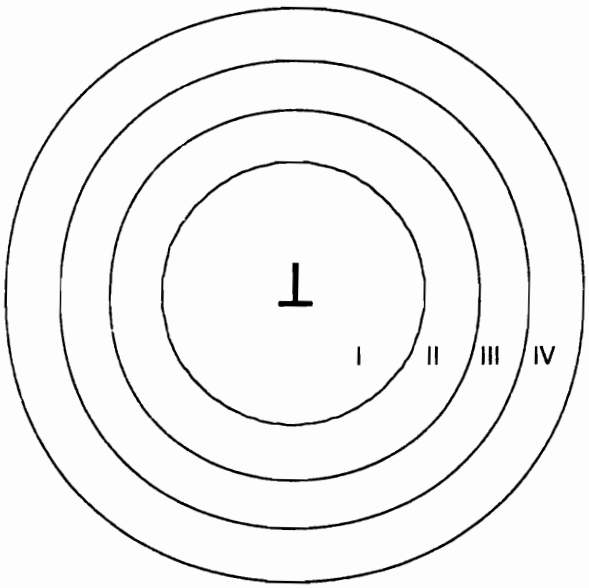

Figure 2.1: Concentric regions about a dislocation for the simulation.

dipole moments. In other words, there are two kinds of fields in region II: $\bar{u}_v$ and $\bar{u}_c$. $\bar{u}_v$ is fixed and $\bar{u}_c$ is a function of dipole moments. The dipole moments are not minimization variables. They are calculated from the force moments in region II after each iteration in region I and are used to correct the mismatch forces at the boundary. The simulation program is set to find the coordinates $\bar{x}$ and the dipole moment tensor during minimization process.

In order to find the configuration with minimum energy, coordinates and dipole moments should be varied simultaneously, this is sophisticated from the point of view of programming, however. Practically, the program is arranged in such a way that coordinates are varied first while $\bar{\bar{\lambda}}$ remains constant (such as null) until some convergence criteria is reached. Then, $\bar{x}$ remains constant and $\bar{\bar{\lambda}}$ is varied, and so on. Mismatch forces created at the interface between region I and II in the first step are offset during the relaxation of the second step through the variation of the core field $\bar{u}_c$. Region III is needed to calculate the force and energy in region II properly. Region IV is designed for the force calculation in region III, which is a feature of an EAM potential (not needed for a pairwise potential) that considers the way in which forces and electronic density are linked. Atoms within a distance of 1.1 nm (twice the cut-off distance of the potential) from the boundary of the cylinder were fixed while the rest of the atoms were relaxed by minimizing potential energy.

The relaxed cores obtained in the present simulations were less than 1.5 nm in dimension or extent (see Chapter 4), except in the case of the <111> edge dislocation where the core was much wider on the (110) plane(see Chapter 5). For this dislocation a cylindrical region of diameter 15 nm was used. Actually, when the diameter of the unconstrained cylinder is larger than twice the dimension of the core, the cylinder size has a negligible effect on relaxations at the core. Such a result is expected from the principle of St. Venant (Hirth and Lothe 1984 [26]).

In the atomistic simulation of dislocation motion under stress, i.e., the calculation of the Peierls stress, an atomic array of circular cross-section containing the dislocation in the relaxed unstressed state with the periodicity along the dislocation line is subjected to a pure shear stress of the type

$$\sigma_{ij} = \tau(n_i\beta_j + n_j\beta_i) \tag{2.17}$$

where $\bar{n}$ is a unit vector perpendicular to the slip plane, β is a unit vector pointing along the Burgers vector, and τ is the magnitude of the applied stress. The stress of Eq. 2.17 is translated into the corresponding homogeneous strain via Hookes' law and this, in turn, generates the corresponding atomic displacements which are permanently applied to the boundary atoms.

The potential energy of the inner atoms is then minimized by moving their coordinates independently until the forces are below a certain level. At the end of this stage the forces on the boundary atoms are calculated and the force moment tensor evaluated as

$$M_{ij} = \sum_{l} g_i(l) r_j(l) \tag{2.18}$$

where g(l) and r(l) are the force and coordinate of atom "l". M_{ij} is symmetrical in the indexes (12), (21) and is equal to the λ_{ij} of Eq. 2.14 after dividing by the length of the period along the dislocation line. The dipole tensor so obtained is introduced into Eq. 2.13 and the boundary atoms are displaced accordingly. This corrected boundary constitutes a new condition for the energy minimization of the inner atoms, and the whole process is iterated until a convergence criteria is fulfilled. Dislocation displacement is evidenced by a sudden increase of the dipole tensor components in Eq. 2.16, which is solved for $\delta x_2 = 0, \delta x_1 = 1$, with direction $\bar{x}_1$ parallel to the slip plane. Also, a graphical method [28] is employed for the representation of dislocation cores, which will appear in the next chapter. When fully relaxed, the resultant configuration was examined for any change in the location of the core. If the core was displaced from its unstressed location, the dislocation was taken to have moved. Starting with the relaxed unstressed core each time, the stress imposed was varied and the resulting configuration relaxed and examined for dislocation motion. Using a binary search, the minimum stresses to initiate motion were determined. Finally, it must be pointed out that the simulations presented here involve molecular statics calculations which implies that the temperature of the simulation is 0°K. By definition, thermally activated processes were not captured by such simulations suggesting that only an idealized mobility for uniform motion of the dislocation line was simulated.

2.4 Examples

We apply the above procedure to [100] edge dislocations in B2 NiAl slipping on (010) and (011) planes. The computations are carried out using fixed and flexible boundaries, with atomic array sizes ranging from 15 to 45 Å of inner cross-section radius. In this work, Voter and Chen's interatomic potential as described in Chapter 1 is being used. The program can be run in various computer platforms, such as the IBM 3090, the IBM RISC 6000, and even the IBM PCs. The calculations for the biggest sizes using flexible boundary take about one hour of computing time in IBM PC 486/33 with the Lahey FORTRAN compiler.

For (011) slip, the results for the Peierls stress show that fixed boundary runs converge quickly to the value given by the flexible runs, which remains approximately constant through the series of array sizes tried: about $0.36 \times 10^{-2}\mu$, with μ being the Voigt's average of elastic constants.

The situation for (010) slip is different. The fixed boundary simulation gives no reliable result. This is so even for the smallest flexible runs. A sudden drop of the critical stress (at an array size of about 35 $\mathring{A}$ of inner radius or 1000 free moving atoms) is verified in the flexible runs: from 2.4 to $1.1 \times 10^{-2}\mu$ remaining unchanged by further increasing the array size.

These results can be understood as the following. The $\{011\}$ planes of B2 alloy are the most compact planes of the structure, all of them possess the same chemical composition, and the dislocation does not undergo severe transformations while crossing the Peierls barrier. In contrast to (010) slip, the stacking sequence of the planes along [010] directions of the alloy, imposes two symmetric core structures that differ in their stoichiometry (see Chapter 4); one is Al rich, which is the one considered here, and the other is Ni rich. Here the dislocation core undergoes severe density changes while crossing the Peierls barrier, and small simulation sizes may hinder the transformation.

Another interesting point† is that, for the two dislocations illustrated here, the Peierls energy is due to atomic shifting in the compact (011) planes independently of the slipping on (011) or (010) planes. This is shown in Figure 2.2, where the two cores, under stresses slightly below

†First noticed by R. Pasianot and E. J. Savino

Table 2.1: Peierls stress for [100](011) edge dislocation in the unit of μ, the Voigt average of elastic constants.

	Size		
	15 Å (242)	26 Å (728)	45 Å (2178)
Fixed	0.50 - 0.52	0.42 - 0.44	0.40 - 0.42
Flexible	0.32 - 0.33	0.33 - 0.35	0.35 - 0.37

Table 2.2: Peierls stress for [100](010) edge dislocation in the unit of μ, the Voigt average of elastic constants.

	Size		
	15 Å (172)	29 Å (643)	45 Å (1548)
Fixed	3.4 - 3.5	2.9 - 3.0	2.7 - 2.9
Flexible	2.2 - 2.3	2.4 - 2.5	1.0 - 1.2

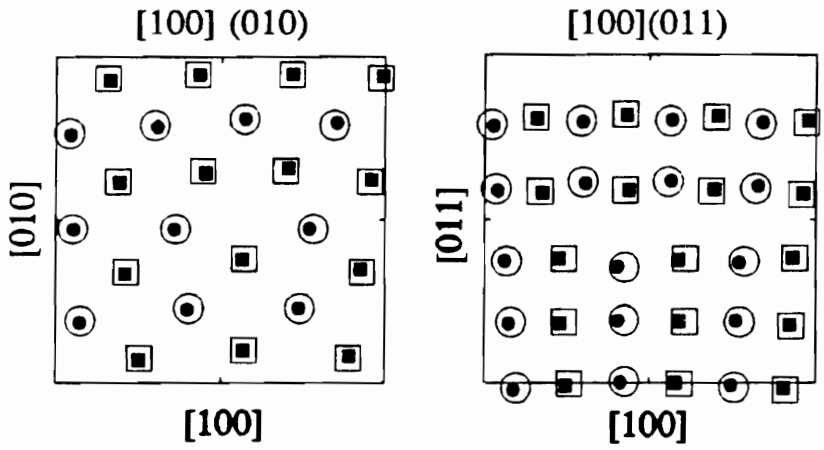

Figure 2.2: Core configurations for (010) slip (left) and (011) slip (right). ○: Ni atoms, □: Al atoms. Open symbols are for the unstressed state, closed smaller symbols correspond to a stress slightly below the critical value.

their critical stress, are compared with the unstressed configuration.

2.5 Concluding Remarks

An important improvement to the simulation codes used in the present work is that the boundary atoms can be displaced according to the field given by a dipole moment tensor created at the elastic center of the dislocation . The total energy of the block of atoms is then minimized with respect to the coordinates of all the atoms in the free move zone and the mismatch forces are offset by the components of the dipole moment tensor. These codes permitted the use of smaller atomic arrays than rigid boundary codes, gave better descriptions of core non-linear effects, and allowed fair assessments of the Peierls stress for dislocation motion.

Chapter 3

Atomistic Representation of Dislocation Core Structures *

The purposes of the atomistic simulation of dislocations are to obtain information on core structures and their relationship to the various crystallographic planes in crystals and to analyze the shape of the core in relation with the mechanisms of dislocation motion. In general, it is found that if the dislocation core is spread along the glide plane, the dislocation will glide easily at relatively low Peierls stresses. It is therefore very important to be able to obtain a clear representation of the dislocation core structure, namely its shape and crystallographic orientation.

In previous works [28, 29, 30] a graphical method to view dislocation core structures resulting from atomistic computer simulation haved been introduced. This chapter will give the details of this new method and compare its advantages with respect to other methods commonly used in the literature for the representation of the core structure obtained from atomistic computer simulation.

---

*Based on "Representation of Atomistic Dislocation Core Structure", by R. Pasianot, Z. Xie, D. Farkas, and E. J. Savino, in *Scripta Met. et Mater*, **28**(3), pp. 319-324, 1993, and "Visualization of Dislocation Core Structure and Motion in Ordered Alloys", by Z. Xie, R. Kriz, and D. Farkas, in *EPD Congress, 1993*, TMS, 1992, pp. 679-685

3.1 Strain Invariants

In the framework of continuum mechanics, the geometrical state of a body that undergoes deformation is characterized by strain tensor [31]; particularly, for small deformation, the strain tensor is defined as

$$\epsilon_{ij} = \frac{1}{2}(\frac{\partial u_i}{\partial x_j} + \frac{\partial u_j}{\partial x_i}) \tag{3.1}$$

where u_i and u_j are the components of the displacement vector field that links the deformed state with the reference state, and x_i and x_j are cartesian coordinates. The above quantity is the centerpiece of the theory of continuous media as is demonstrated in any standard textbook. The same concept may be applied to atomistic computer simulation studies involving a large number of atoms, such as a dislocation. The main output from the simulation consists of the displacements from the perfect lattice positions for each atom in the core region. There is a clear need to systematize a large mass of discrete data and search for the quantities which can best characterize the core of dislocation.

For this purpose a finite difference scheme is applied to evaluate the derivatives of Eq. 3.1 at the atom positions. Fig 3.1 gives an example for the calculations of an fcc-based crystal. The derivatives can be carried out as

$$\frac{\partial u_z}{\partial x} = \frac{1}{6a}(\sum_{i=1}^{5} u_z(i) - \sum_{i=1}^{18} u_z(i)) \tag{3.2}$$

The numbers refer to the labels shown in Fig. 3.1. The reference atom (O) is located at the center of a cube of edge "a" (the lattice parameter),and the displacements at the face centers are obtained by averaging over their six first neighbors; the derivatives are computed using a centered finite difference scheme on these displacements. A similar process can be developed for other crystal structures. A code has been written to facilitate the calculation for bcc- and fcc-based crystal structures.

Care must be taken in selecting the neighboring displacements of a given atom that enter the calculation; if the difference with the central atom displacement, projected onto the burgers vector (b), is bigger than $b/2$ (less than $-b/2$), then b is subtracted (added) to it and the result entered in Eq 3.2. This is analogous to what happens in the continuum theory where stresses

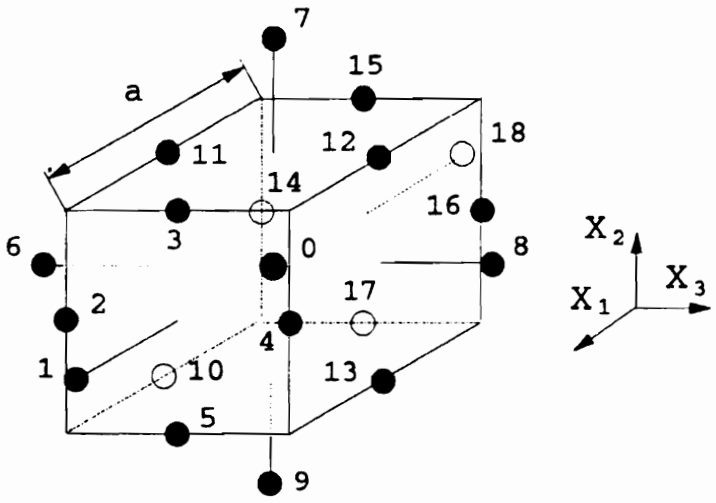

Figure 3.1: Finite difference scheme used for an fcc based structure

and strains are continuous across the branch cut that generates the dislocation, concentrating the higher strains in the core region. With the derivatives of Eq 3.2 the tensor of Eq 3.1 is calculated at each lattice point belonging to the plane perpendicular to the dislocation line. A complete picture requires, therefore, six two-dimensional (2-D) figures that may be obtained using standard graphical software. Contraction can be used to simplify the representation of strain tensor. The adequate scalar quantities associated to ϵ_{ij} should not change with rotation of the coordinate axis about dislocation line direction. Assuming the dislocation line along axes z , the strain tensor is written as

$$\epsilon = \begin{pmatrix} \epsilon_{xx} & \epsilon_{xy} & \epsilon_{xz} \\ \epsilon_{yx} & \epsilon_{yy} & \epsilon_{yz} \\ \epsilon_{zx} & \epsilon_{zy} & \epsilon_{zz} \end{pmatrix} \tag{3.3}$$

Considering rotations about z, the upper-left 2×2 submatrix is transformed like a 2-D matrix. $(\epsilon_{xz}, \epsilon_{yz})$ is transformed like a 2-D vector, and ϵ_{zz} stays unchanged. The most obvious invariant of a 2-D vector is the square of its length, we define therefore

$$Y1 = 2(\epsilon_{xz}^2 + \epsilon_{yz}^2) \tag{3.4}$$

where the factor 2 has been introduced for having the proper scale when compared with the other invariants defined below. For a 2-D matrix a number of choices are possible, we define

$$\begin{aligned} Y2 &= \epsilon_{xx}^2 + \epsilon_{yy}^2 + \epsilon_{zz}^2 \\ Y2' &= 2\epsilon_{xy}^2 + \frac{1}{2}(\epsilon_{xx} - \epsilon_{yy})^2 \end{aligned} \tag{3.5}$$

$Y2$ is the so called norm of a matrix, whereas $Y2'$ is the norm of the matrix in which the hydrostatic part, $(\epsilon_{xx} + \epsilon_{yy})/2$, has been subtracted.

Provided one can assure an unique solution, namely, there is no symmetry-related (energetically equivalent) core structures, an important feature can be obtained from the above definition. If the xy plane is a mirror plane or z is an even fold symmetry axis, particularly for an isotropic medium, $Y1$ is attributed only by screw components and $Y2$ (or $Y2'$) by edge

components. In fact elasticity theory [31] shows that only under these conditions an edge dislocation produces no displacements of type u_z, and a screw one produces no displacements of type u_x or u_y. On the other hand, if there are several energetically equivalent core structures, the validity of this argument can be justified on the actual symmetry and the values of Y1 and Y2.

3.2 Comparison with Differential Displacement Maps

A point to note regarding the present method is that it is unable to directly identify either the Burgers vector of a dislocation or its possible dissociation into partials after relaxation. In fact, this is a common feature of the methods available so far. The Burgers vector is an *ad hoc* element whose choice is varied until a consistent picture is obtained. Fig 3.2 illustrates the point for the case of a 1/2[110] screw superpartial in Ni_3Al ($L1_2$ structure) as obtained from a computer simulation run [28]. A complex stacking fault dissociation, analogous to Shockley dissociation in fcc metals, has been proposed in the literature[32]. Fig 3.2(a) is a contour line plot of Y1 assuming no dissociation, whereas in Fig 3.2(b) a Shockley like splitting was assumed. The latter is the most adequate picture because of the neat separation between the two regions of highest strain.

The picture of the "structure-less" core of the elastic solution is important in identifying core structure elements. An elastic solution of the well known three-fold symmetry core of the 1/2[111] screw dislocation in bcc metals [32] would have six-fold symmetry when viewed in the strain invariant contour plot, see Fig. 5.1 in Chapter 5. Fig 3.3 is for a simple [100] edge dislocation on a cubic plane of the B2 NiAl intermetallic alloy. Two dimensional contours make it very easy to detect high and low gradient (based on the spacing of contours) and the precise orientation of the gradient (perpendicular to the contours). For high deformation levels it is very difficult to see core spreading in any particular plane, whereas for lower levels the core spreads on $\{110\}$ planes as does the elastic solution of the problem.

A closely related method was applied by Basinsky *et al* as early as 1971 [33]. They calculated local stresses instead of strains, and explored the vector properties of shear stresses. They also represented displacement difference between the simulated result and the elastic solution result

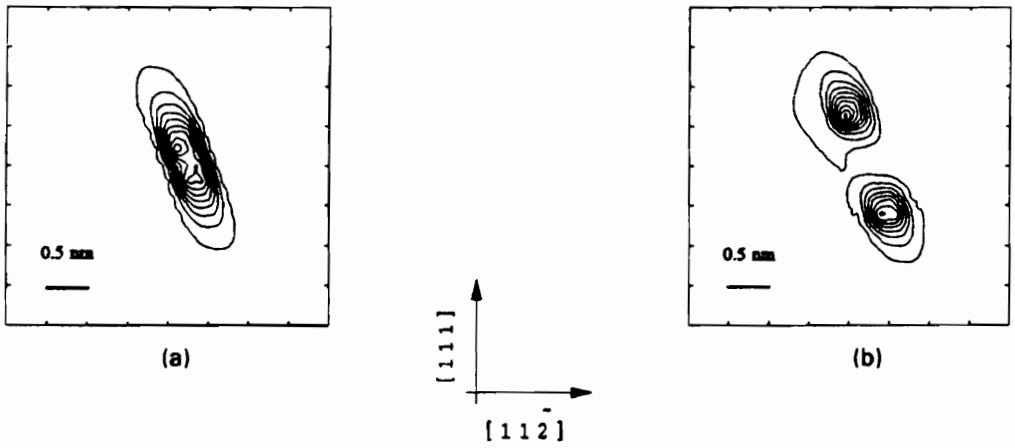

Figure 3.2: Contour plot of invariant Y1 for a 1/2[110] screw superpartial dislocation in Ni_3Al. (a) assuming no dissociation, (b) assuming Shockley type splitting

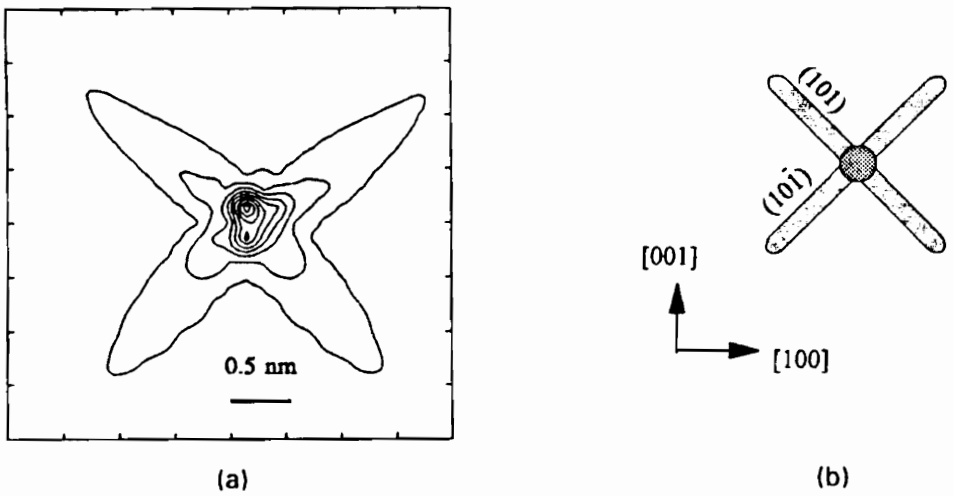

Figure 3.3: [100] edge dislocation in B2 NiAl. (a) Contour plot of invariant Y2, (b) crystallographic planes of core spreading

[34]. However, the most popular method is the differential displacement maps ("arrow plot") as introduced by Vitek *et al* [35]. We will concentrate next on the comparison of the strain invariant method with this method. In brief, the latter method consists of a set of three graphs, for the general dislocation case, corresponding to displacements on the three coordinate axes. Arrows are drawn in each graph between two neighboring atoms with magnitude proportional to their difference in displacement. A similar procedure to ours is applied when this difference is bigger in size than $b/2$. The direction of the arrow is indicated for the nearest neighbor pair of atoms considered.

The arrow plot method has some drawbacks. The first relates to its graphical representation, namely, only high deformation levels are evidenced and the lower ones appear almost all the same. For a simple dislocation this method is quite simple and successful, like the pure edge dislocation in Figure 3.1, where displacements occur in only one direction. For mixed dislocations that can spread in several planes, it would require in general three different plots corresponding to displacements in the three different coordinates. As the dislocation line index increases, the arrow pictures may show a clumsy appearance. This point is shown in Fig. 3.4, where arrows joining atoms at different levels along the z axis cross each other. The situation becomes critical when complex core structures are considered. Fig 3.4 is for the case of a [100] Burgers vector and a dislocation line in [120] direction in B2 NiAl, where the two methods are compared. The present strain invariant method clearly shows that there is core spreading along $\{123\}$ type planes, which is hardly evidenced by the arrow method.

There is another more serious point related to the purely conventional nature of the arrow method. Though it may succeed in giving a qualitative picture, the represented quantities are not tied to any physical magnitude. They have no tensorial character and no theory can be built upon them.

3.3 Relation of Core Shape and Lattice Crystallography

We can represent the three dimensional crystal lattice as projected onto the plane perpendicular to the dislocation line. In the case of alloys different symbols can be used to represent different types of atoms and different sizes of the symbols can indicate the distance of the

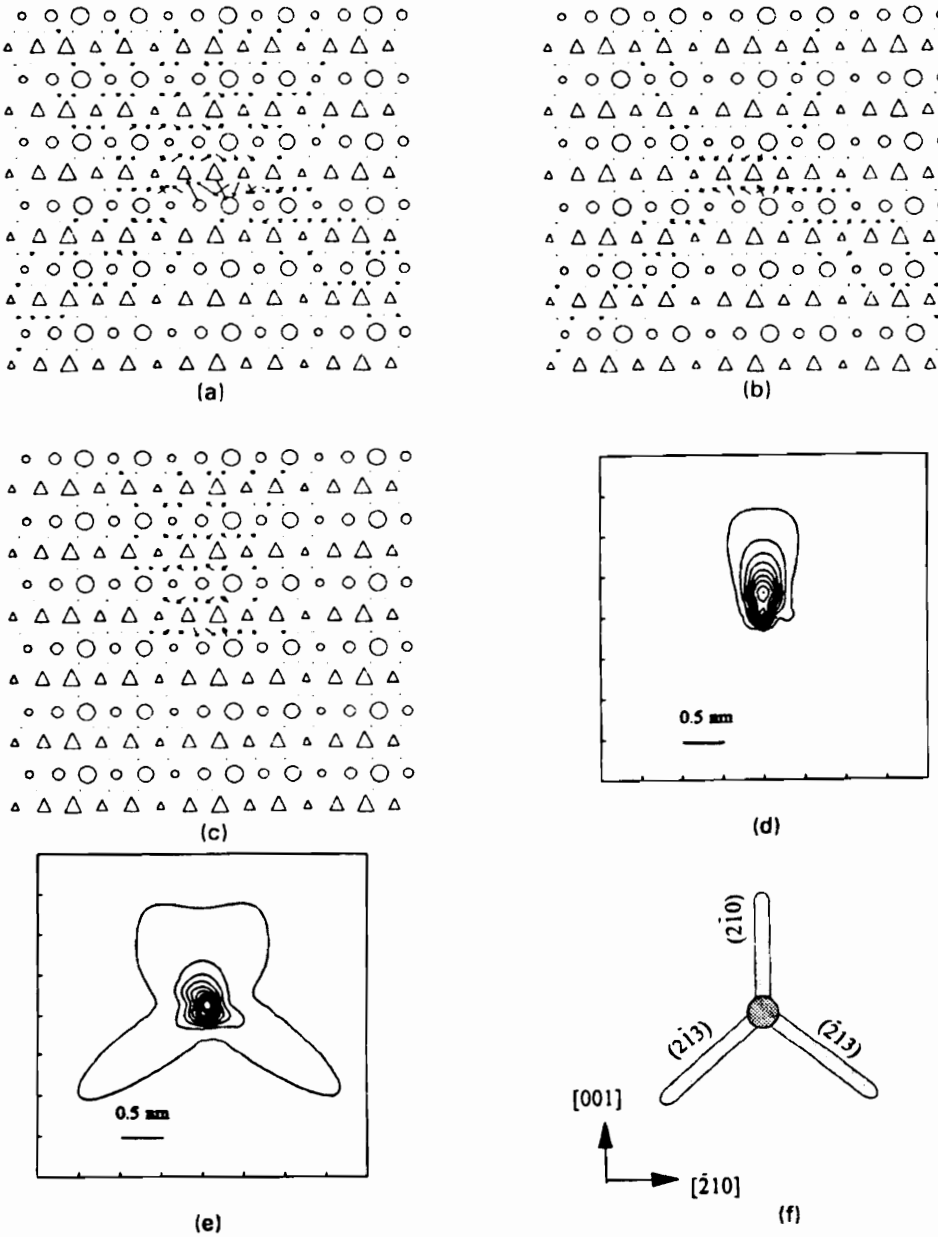

Figure 3.4: Representation of a mixed dislocation in NiAl using (a) - (c) differential displacements, (e) and (d) two invariants of the strain tensor, (f) crystallographic directions and planes. Circles represent Al atoms and triangles represent Ni atoms

represented plane from the plane of the paper.

Commercial visual tools, for example, PV-WAVE, can be used to get graphs of invariants, and then Adobe Photoshop used to superpose the crystal lattice onto the graphs. In this way, crystallographical direction, screw, and edge component can be shown at the same time. An example is shown in Figure 3.5. In the figure, one of these two invariants can be represented as a contour plot and the other can be mapped to shades of gray or, ideally , color.

3.4 Concluding Remarks

An advantage of the present method is the easy identification of core spreading corresponding to the various crystallographic planes and directions. Theoretically important is that it is derived from a continuum mechanics concept. Therefore, it is more suited to bridge the gap between a discrete atomic picture and continuum models, which were so well developed for dislocations. It is also open to analysis of the core structure using other possible invariants, as visualization techniques for second order tensors will allow. The methods also allow the visualization of the motion of dislocation under applied stresses in a video form, where stresses are cast into time[30].

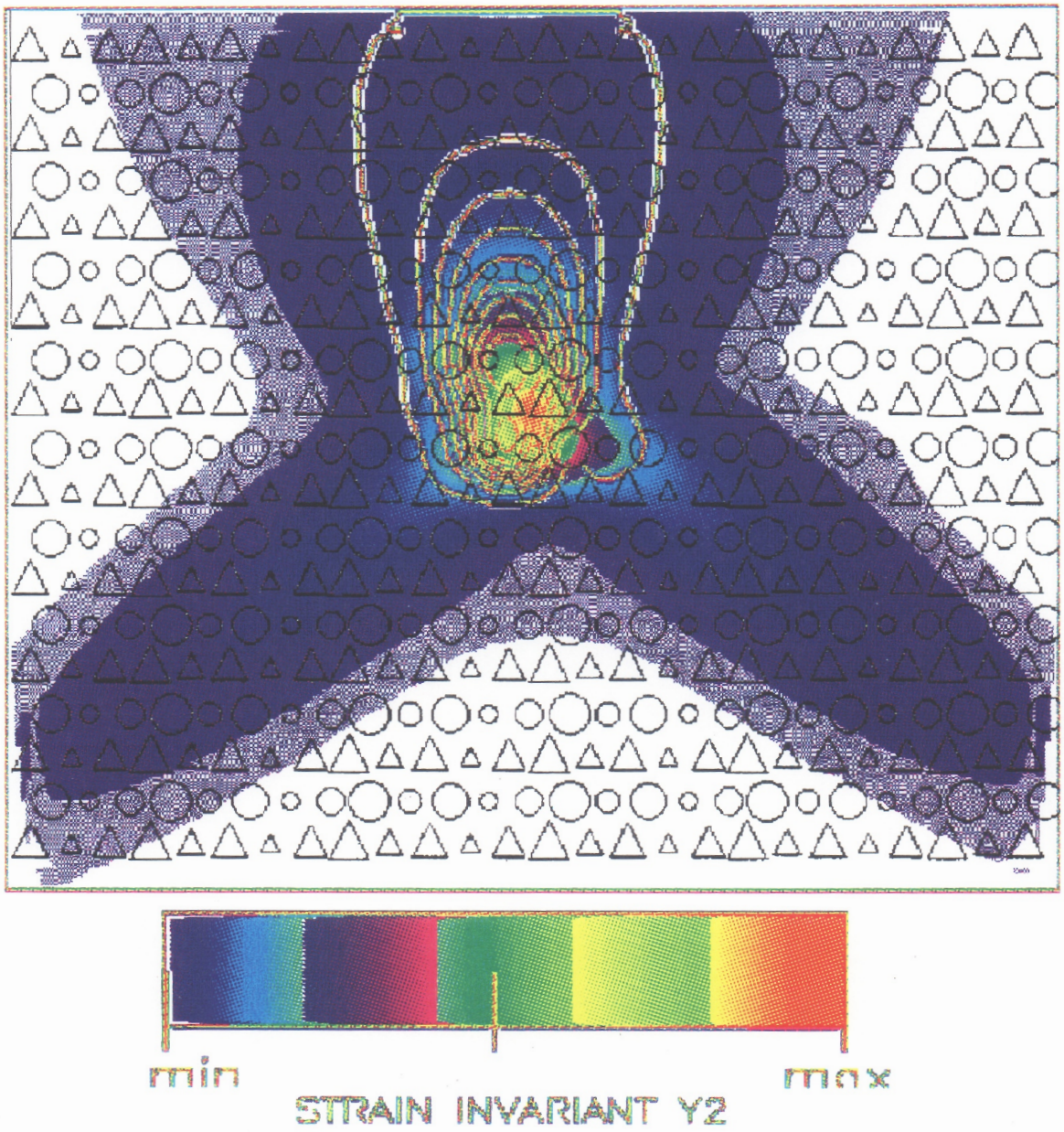

Figure 3.5: Visualization of the same mixed dislocation of Figure 3.4, two invariants of the strain tensor and the projected lattice are plotted. Y1 is represented as contour plots and Y2 is mapped to color, circles represent Al atoms and triangles represent Ni atoms

Chapter 4

Core Structure of ⟨100⟩ and ⟨110⟩ Dislocations in NiAl *

4.1 Slip Systems in NiAl

The deformation mechanisms and mechanical properties of NiAl have been studied extensively not only because of NiAl's potential in high temperature applications, but also because of the attractiveness of NiAl as a model system for deformation in a high symmetry ordered cubic compound. It has been well-established that deformation occurs principally by the motion of ⟨100⟩ dislocations in polycrystals and single crystals loaded along non-⟨100⟩ axes (defined as "soft" crystals [37, 38, 39, 40, 41, 42, 43, 44]). For "soft" orientations, the yield strength is relatively low above room temperature (RT) and increases moderately below RT [42].

Alternate slip vectors are observed in single crystals stressed along ⟨100⟩ axes (defined as "hard" crystals), since there is no resolved shear stress on (100) dislocations in these crystals [42, 45, 43]. Although ⟨110⟩ dislocations have a lower line energy [38], a smaller Burgers vector, and a higher Schmid factor than ⟨111⟩ dislocations, ⟨111⟩ slip is preferred in "hard" single crystals deformed in compression below 400°C [44, 43]. This implies that the critical resolved shear stress (CRSS) for ⟨110⟩ glide is higher than the CRSS for ⟨111⟩ dislocations below 400°C. Yielding in the "hard" orientation at RT occurs at a stress approximately ten

*Based on "Computer Simulation of the Core Structures of ⟨100⟩ Dislocations in Ordered B2 NiAl", by R. Pasianot, Z. Xie, D. Farkas, and E. J. Savino, accepted by, *Modelling and Simulation in Materials Science and Engineering* [36]

times larger than in the "soft" orientation, and amounts to nearly 2% of the shear modulus [45]. In "hard" single crystals above 400°C, ⟨110⟩ dislocations begin to operate [46], and the yield strength decreases sharply with temperature [47]. Therefore, it can be inferred that the CRSS for ⟨110⟩ dislocations decreases significantly with temperature, and becomes smaller than the CRSS for ⟨111⟩ dislocations. The high yield strengths and strong temperature dependence of flow, particularly for non-⟨100⟩ dislocations suggest that dislocation motion is difficult and requires significant thermal activation.

Impeded dislocation mobility could be related to the core structure of the dislocations. The magnitudes of the Burgers vectors in NiAl (0.288 nm for ⟨100⟩, 0.407 nm for ⟨110⟩, and 0.499 nm for ⟨111⟩ dislocations) are quite large when compared to the Burgers vectors in typical b.c.c. and f.c.c. metals (0.250 nm for ⟨111⟩ dislocations in α-iron and 0.249 nm for ⟨110⟩ dislocations in γ-nickel). These large Burgers vectors may result in either large displacements at the core or complex dissociations. In other ordered intermetallic compounds with low to moderate fault energies (e.g.; Ni_3Al and TiAl which have $L1_2$ and $L1_0$, crystal structures, respectively), dislocations are found to dissociate into extended, non-planar core configurations that can dramatically affect the mobility of certain line directions [48]. In NiAl, the splitting of ⟨100⟩, ⟨110⟩, and ⟨111⟩ dislocations into partials has not been observed in weak beam studies after deformation [45], indicating that the fault energies are very high and suggesting that large strain fields exist at the cores.

The large values of the CRSS (especially for non-⟨100⟩ dislocations), the strong temperature dependence of flow, and the large Burgers vectors all suggest that significant non-planar displacements may be associated with dislocation core structures in NiAl.

In this chapter, the following important points regarding ⟨100⟩ and ⟨110⟩ dislocation behavior in the B2 structure NiAl are addressed:

- Changes in the core structure for different orientations of the dislocation line.
- Type of crystallographic plane favored for core spreading.
- Relation between elastic dislocation strain fields and computed core structures.

The simulation of core structures of ⟨111⟩ dislocations will appear in the next chapter.

For each dislocation the core shape is studied as resulting from the relaxed atomic coordinates by means of the two invariants discussed in Chapter 3. In each case the elastic solution is also studied and the corresponding figures of Y1, and Y2 are compared with the simulated ones. Different initial positions of the elastic center of the dislocation are routinely tested to insure that all non-equivalent possible core structures are found. The relative energies of the different possible structures for the same dislocation are studied when more than one core structure is found. The difference of core structures of these two dislocations may offer a fundamental explanation for the anisotopic mechanical properties of single crystals in the "hard" and "soft"' orientations.

A brief comment regarding the obtained results is in order. The contour lines of some pictures show a wavy appearance, for example, Fig. 4.3†(c), (d) and Fig. 4.4 c, d. This is especially true for the low level contours. Several sources are responsible for this effect. First, the numerical convergence of the minimization technique becomes poorer as Miller indices of the dislocation line increase; second, the strain tensor is computed numerically from the atomic coordinates employing a finite difference scheme on the points of a discrete mesh, and the graphical software interpolates among them to obtain a continuum-like representation. Even so, the main features of the plots are not hindered by these effects and an overall fair description of the configurations is obtained as a basis for discussing the physics, as shown below.

4.2 Results of the Core Structures of $\langle 100 \rangle \{001\}$ Slip System

Four orientations of the dislocation line are studied in this system. These are [010], [120], [110] and [210] ranging from pure edge to a relatively large screw component. The pure edge [100] dislocation is shown in Fig. 4.1. The simulation results, (b) and (c), follow closely the elastic result (a). Strains are approximately extended on $\{101\}$ type planes and, as expected, only edge-type strains are non-null. Also, the high strains of the elastic solution are smeared, relaxed, in the dislocation core of the simulated structures; this is particularly seen by comparing

†This format of the figures in this chapter was prepared by R. Pasianot

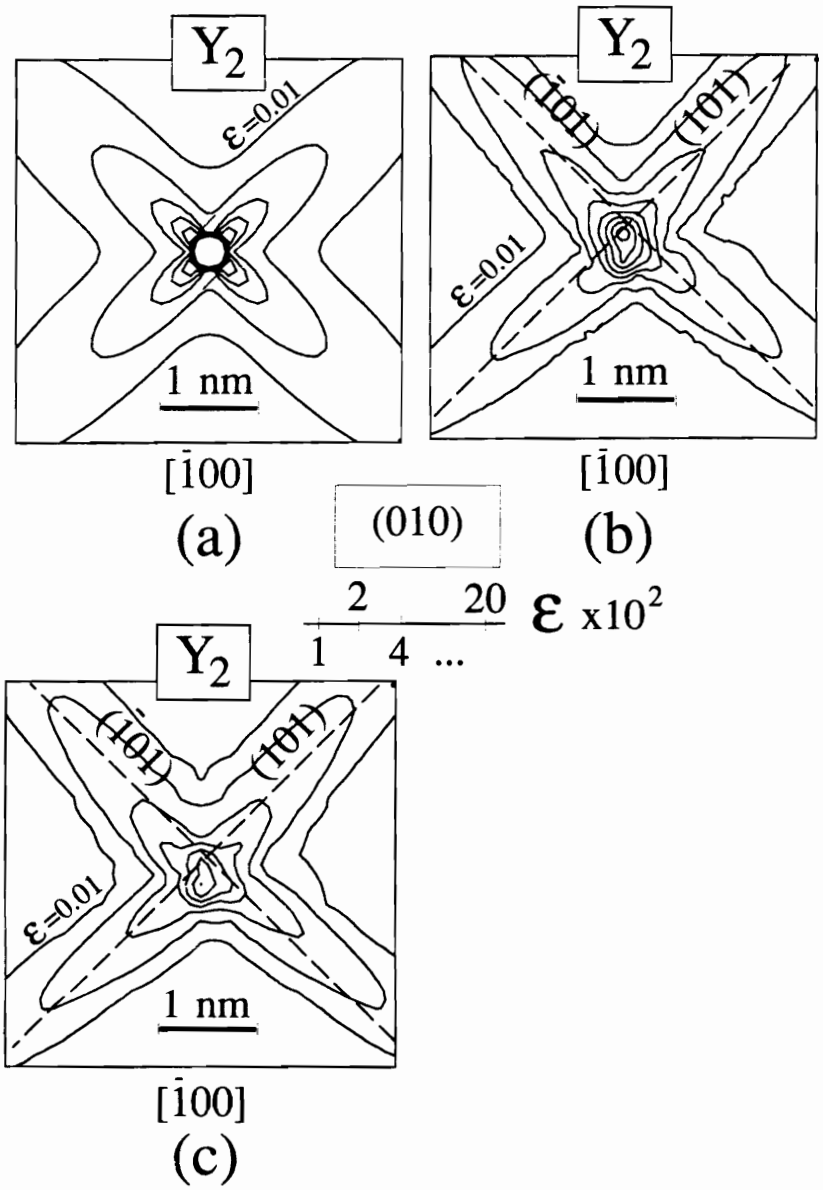

Figure 4.1: Pure edge [100] dislocation on (001) slip plane. (a) is the elastic result, (b) simulated Al-rich core, (c) simulated Ni-rich core. rms strain levels $\epsilon = \sqrt{Y}/2$ increase towards the figure center according to the series 1%, 2%, 4%,..., 20%.

the a= 0.02 contour level. Minor structural differences are found between the Ni rich core, Fig. 4.1 (c), and the Al-rich one, Fig. 4.1 (b), however the highest strain level calculated for the first case is somewhat lower than the one for the second. This is consistent with Al being a larger atom than Ni.

In Fig. 4.2 the core structure of a mixed dislocation oriented along [120] is shown. The simulated structures follow approximately the elastic results with the high strain levels relaxed at the core. A new feature appears in this case, namely, shear processes that are symmetric for the continuum elastic body are not for the discrete lattice structure. Therefore the screw-type symmetrically distributed shears Y1 of Fig. 4.2 (a) are transformed into the lower-energy asymmetrical shears of Fig. 4.2 (c). The same situation is encountered in the Y2 plot; edge-type shears in the simulated structure, Fig. 4.2 (d), are not symmetric with respect to the origin in contrast to the elastic result of Fig. 4.2 (b). Plane orientations near $\{213\}$ show this point most clearly. This is analogous to the twinning-antitwinning asymmetry already reported for the 1/2[111] screw dislocation in bcc metals (V. Vitek, 1974 [32]).

Fig. 4.3 shows the case of a mixed dislocation oriented along [110]. Here, the lattice structure does not distinguish between positive and negative screw-type shears on (110) and therefore Y2 is a symmetrical figure for both the elastic result, Fig. 4.3 (a), and the simulated structure, Fig. 4.3 (c). On the other hand, edge-type strains behave like those of Fig. 4.2 (i.e.; they are asymmetrically distributed on planes near $\{112\}$).

Finally, Fig. 4.4 shows the core structure of a mixed dislocation along [210]. This case is analogous to the one of Fig. 4.2 but with different proportions of screw and edge components. It is seen that the planes favoring strain spreading are also of the same type. The lobe appearing in the lower-central part of Fig. 4.4 (d) can be demonstrated to be due to "mixing" effects from the screw-type strains of Fig. 4.4 (c), and they are apparent here because of the large ratio of the screw to edge components.

4.3 Results of the Core Structures of $\langle 100 \rangle \{011\}$ Slip System

Three orientation lines are studied for this system: [011], [122] and [111]. Because $\{011\}$ planes are of the same chemical composition, there are no core structures of different local

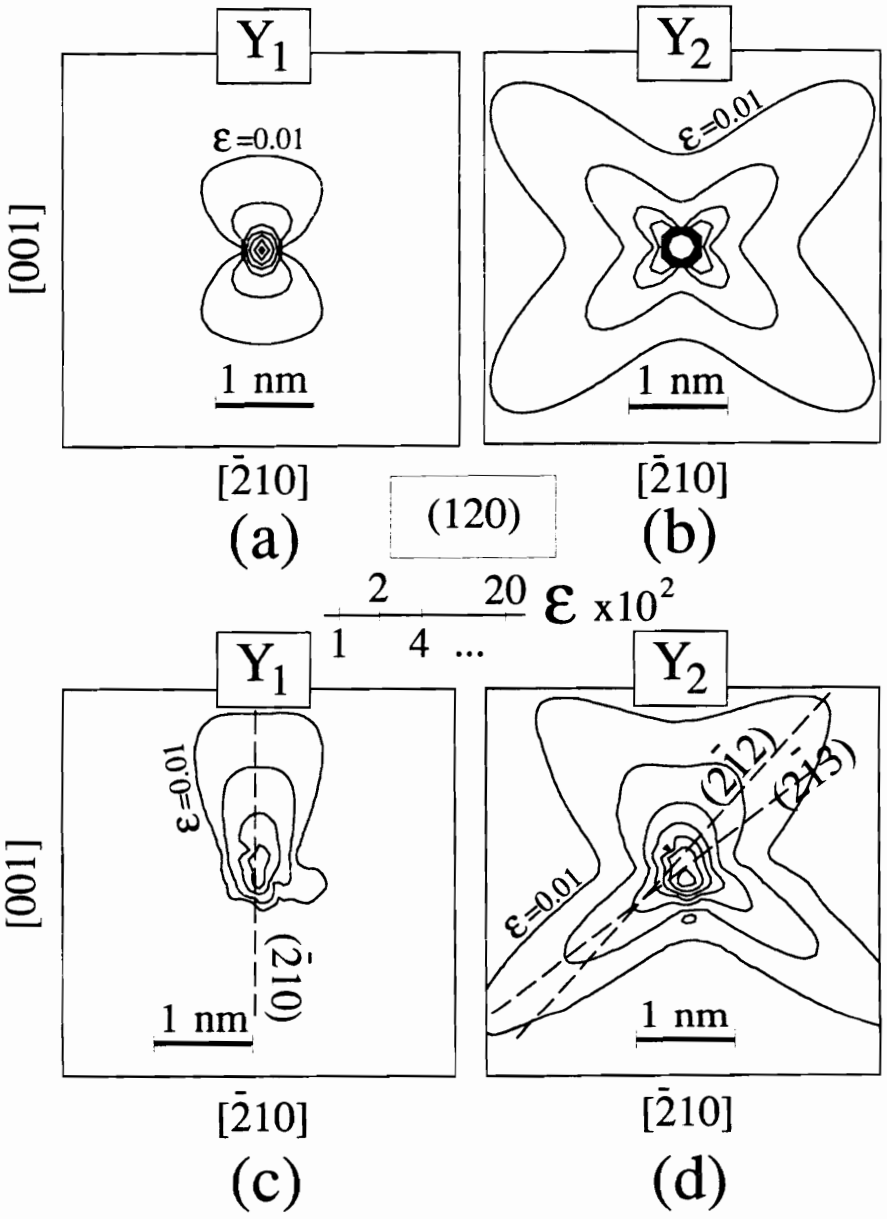

Figure 4.2: Mixed [100] dislocation along [120]. (a) and (b): elastic results, (c) and (d): simulated structures. rms strain levels same as Fig. 4.1. $(\bar{2}10)$, $(2\bar{1}2)$ and $(2\bar{1}3)$ plane traces are shown.

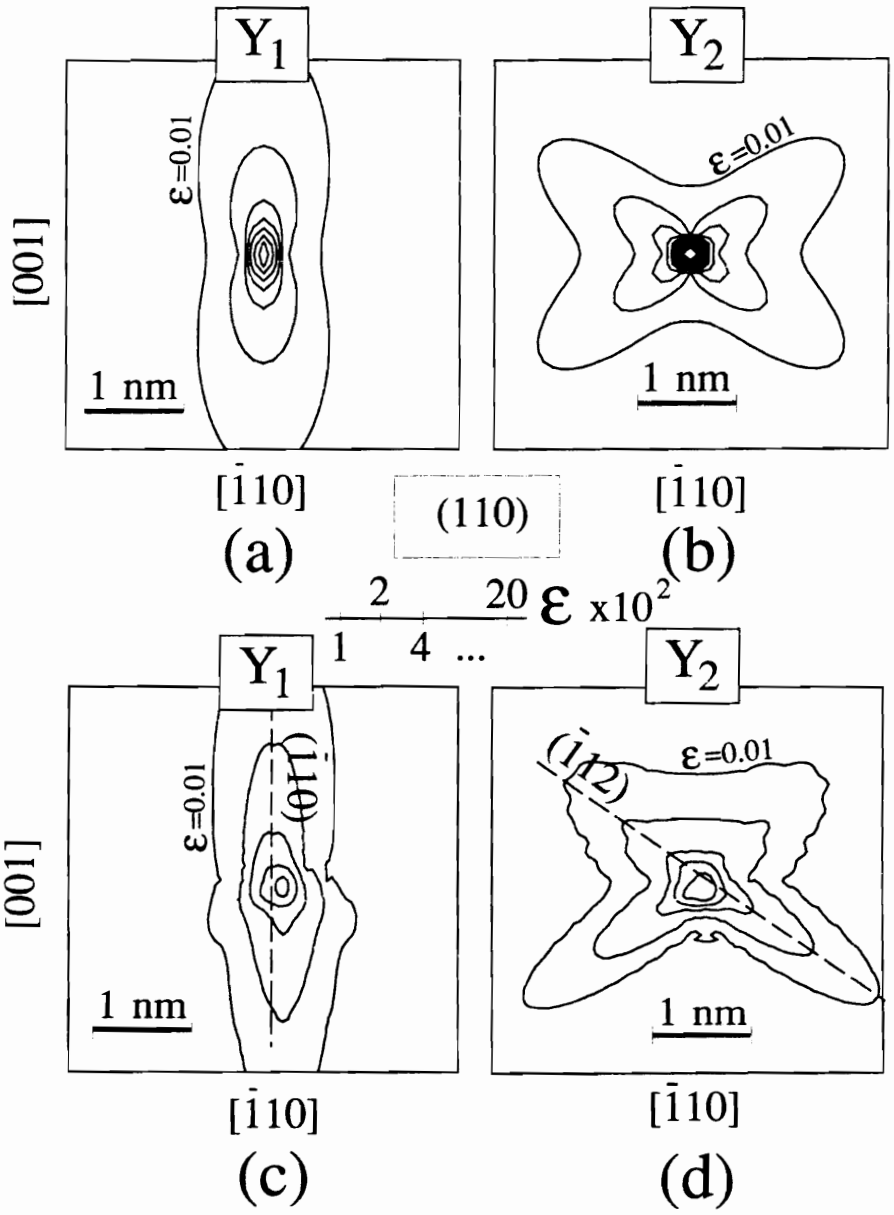

Figure 4.3: Mixed [100] dislocation along [110]. (a) and (b): elastic results, (c) and (d): simulated structures. rms strain levels same as Fig. 4.1. ($\bar{1}12$) plane trace is shown.

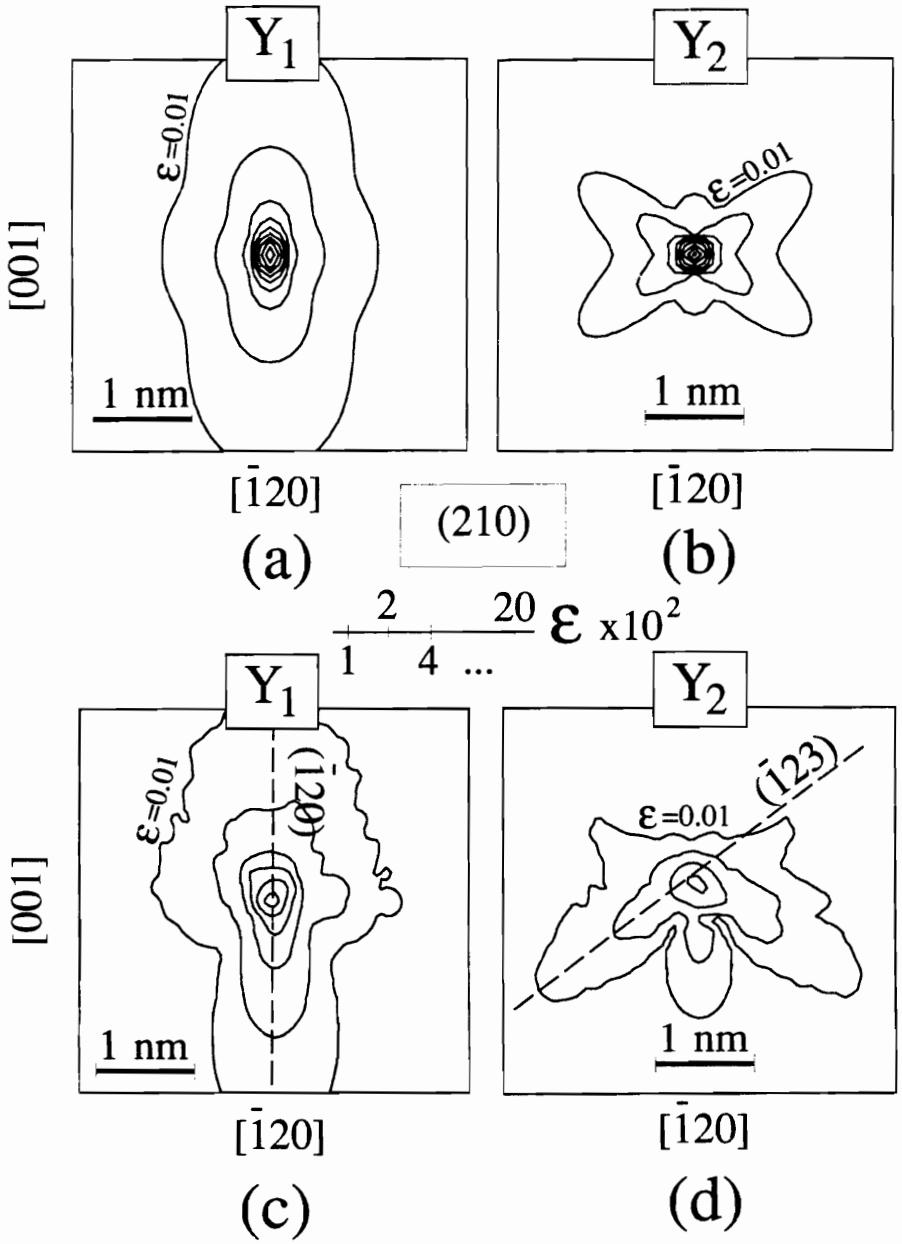

Figure 4.4: Mixed [100] dislocation along [210]. (a) and (b): elastic results, (c) and (d): simulated structures. rms strain levels same as Fig. 4.1.

stoichiometry in contrast to the above slip system.

Fig. 4.5 shows the structure of a pure edge dislocation along [011]. As expected, screw-type strains are absent in the simulated structure and the edge ones spread asymmetrically and approximately on {211} planes.

For the next two dislocations considered, as discussed in Chapter 3, elastic anisotropy "mixing" effects must be taken into account. Fig. 4.6 and 4.7 show the elastic calculations for the [122] and [111] orientations respectively. Labels (a) and (b) correspond to the screw component of the Burgers vectors and (c) and (d) to the edge one. In both cases, it is seen that the "mixing" effect of the screw component upon the Y2 invariant can be neglected. In contrast, the edge component will have a strong effect on Y1 pictures.

In Fig. 4.8 we show the calculations for the [122] line orientation. As expected, invariant Y2 from the elastic field, Fig. 4.8 (b), is very similar to that of Fig. 4.6 (d). On the other hand, the strains of Figs. 4.6 (a) and (c) contribute to those of Fig. 4.8 (a) in a different way; particularly, the strain lobes on (011) plane cancel out while others are enhanced. This cancellation is not effective in the simulated result of Fig. 4.8 (c), giving rise to core effects different from those considered up to here: there is a striking similarity between Fig. 4.8 (c) and (d). This indicates the edge-type strains are dominant, with the Y1 invariant being mainly a by-product of the elastic mixing. Also in this case, the twinning-antitwinning type asymmetry discussed previously is evident.

An analysis totally equivalent to the above can be made when the dislocation line is oriented along [111], with regards to both mixing effects (Fig. 4.7), and core structure (Fig. 4.9). Here, anisotropy mixing effects are already apparent in Fig. 4.9 (a). If these effects were absent the figure would posses six-fold symmetry due to the symmetry properties of the [111] axis.

γ surfaces are helpful in understanding dislocation core spreading. The gamma surfaces normally are computed by displacing one half of a crystal with respect to the other half, with a particular choice of the dividing plane. Relaxation is allowed only in the direction perpendicular to the fault plane. The surface is constructed by plotting the energy of the fault with respect to the fault displacement vector. The gamma surfaces were calculated for several crystallographic planes with particular interest in the vicinity of the perfect crystal.

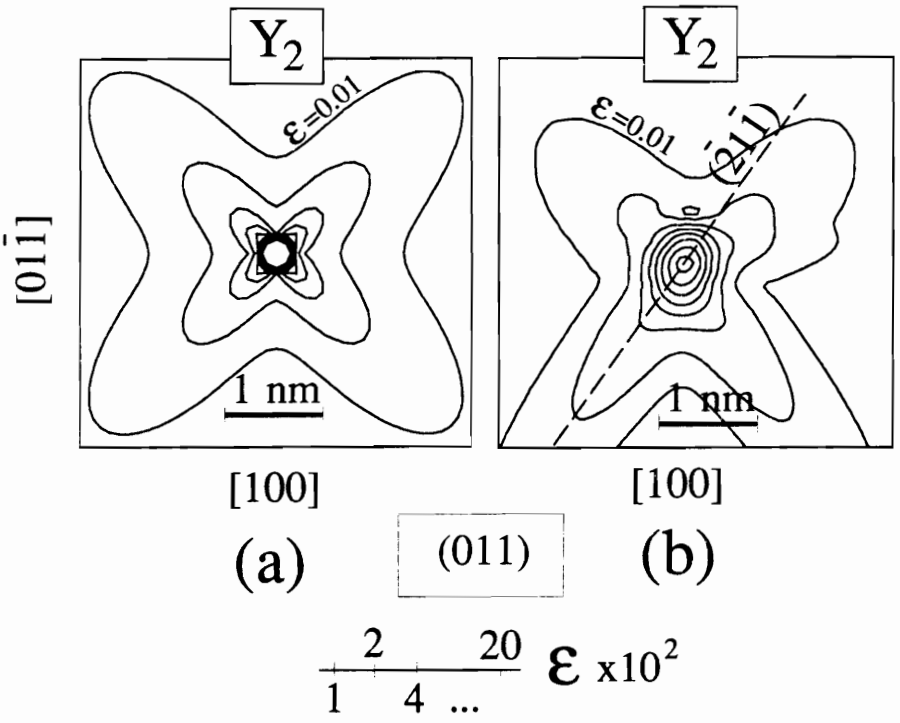

Figure 4.5: Pure edge [100] dislocation on $(01\bar{1})$ slip plane. (a): elastic result, (b): simulated structure. rms strain levels same as Fig. 4.1. $(\bar{2}1\bar{1})$ plane trace is shown.

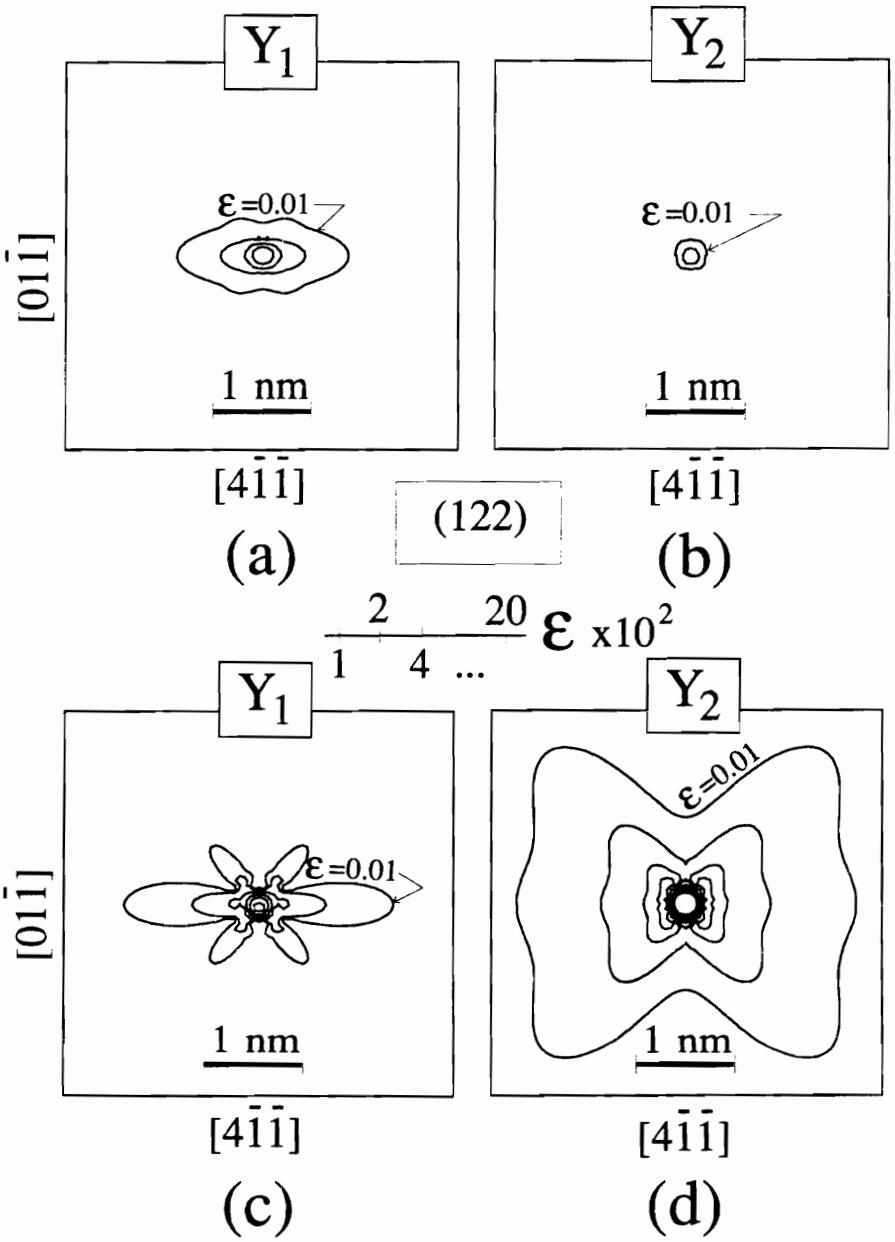

Figure 4.6: Elastic anisotropy effects for a [100] dislocation along [122]. (a) and (b) correspond to the screw component 1/9[122], (c) and (d) to the edge component 2/9[4$\bar{1}$1]. rms strain levels same as Fig. 4.1.

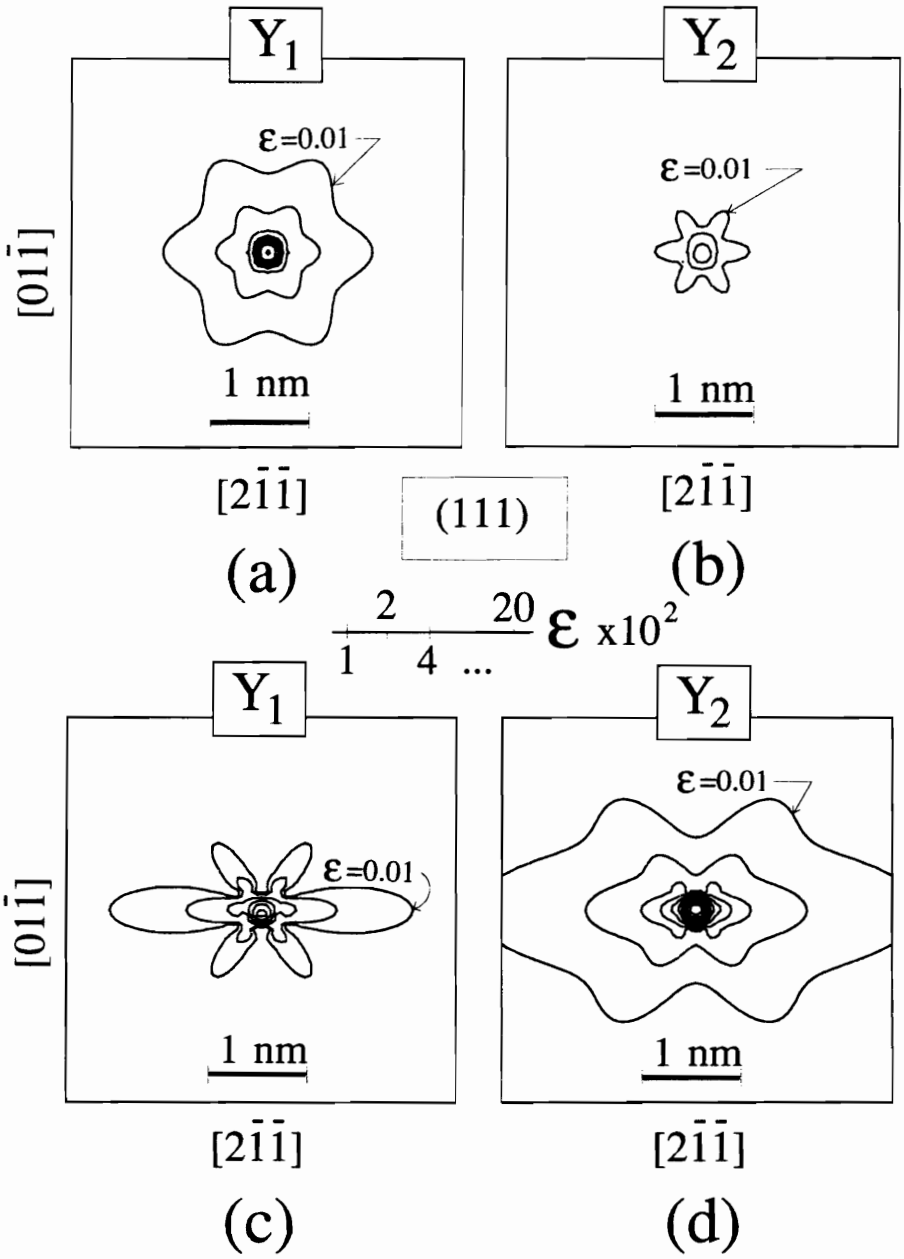

Figure 4.7: Elastic anisotropy effects for a [100] dislocation along [111]. (a) and (b) correspond to the screw component 1/3[111], (c) and (d) to the edge component 1/3[2$\bar{1}$1]. rms strain levels same as Fig. 4.1.

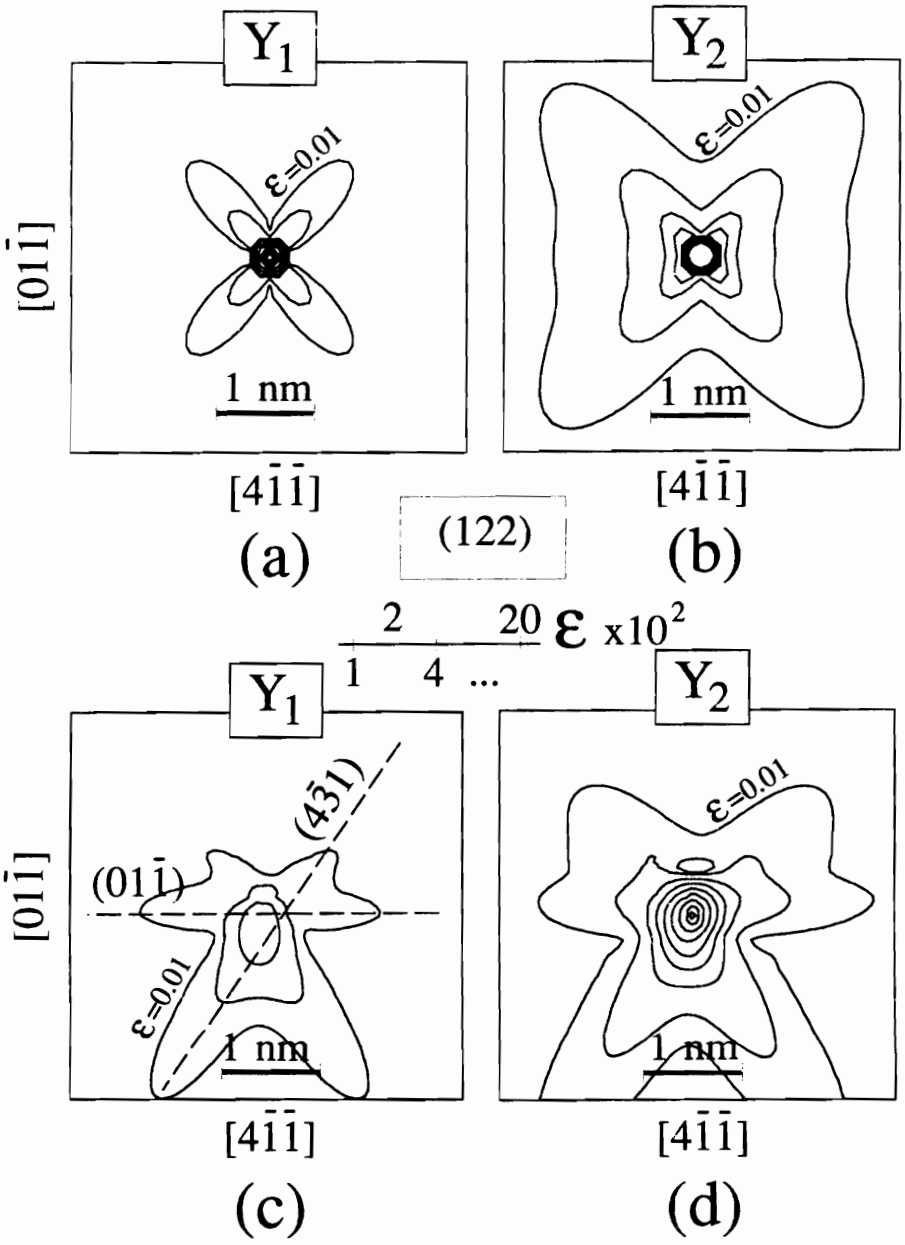

Figure 4.8: Mixed [100] dislocation along [122]. (a) and (b): elastic results, (c) and (d): simulated structures. rms strain levels same as Fig. 4.1. (01$\bar{1}$) and (43$\bar{1}$) plane traces are shown.

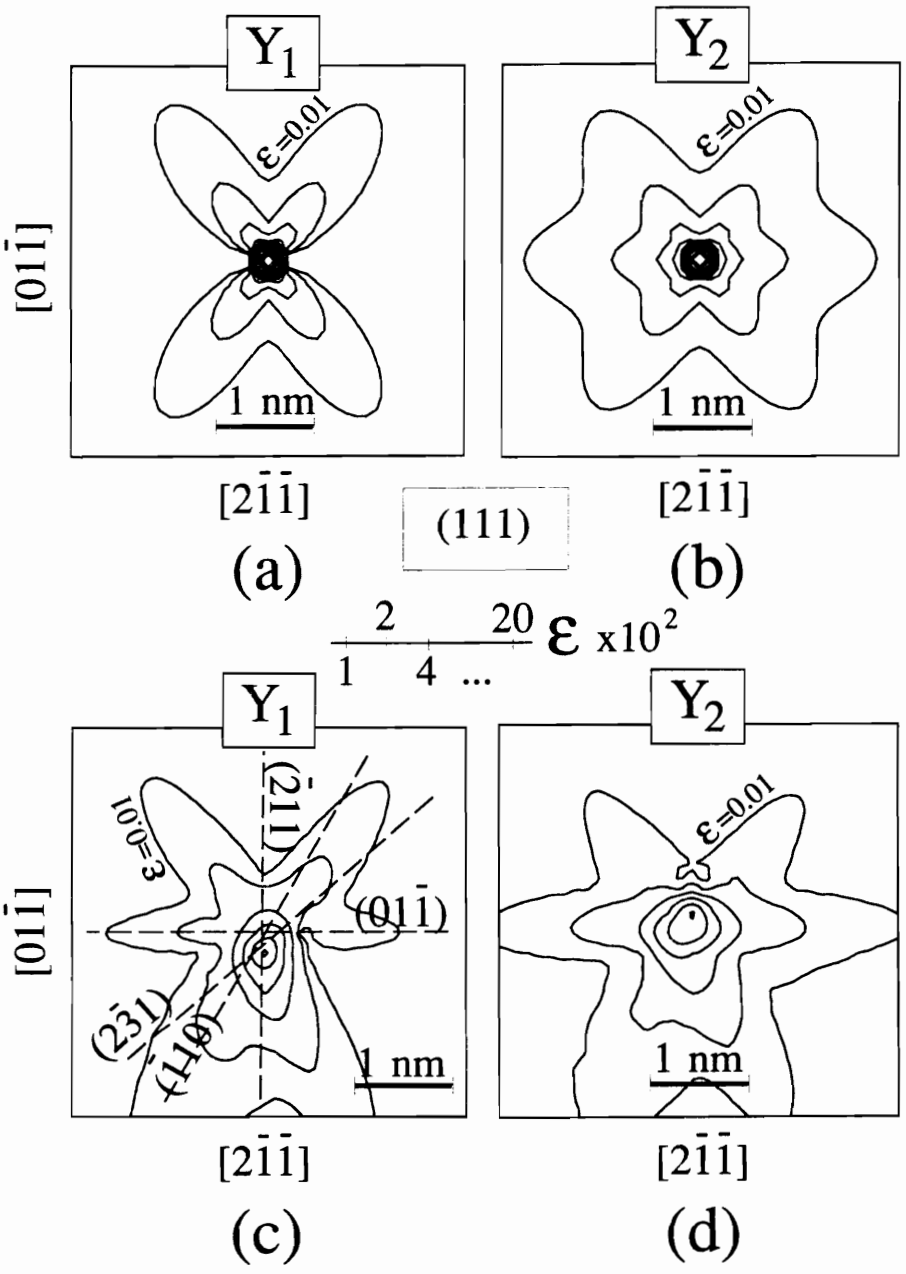

Figure 4.9: Mixed [100] dislocation along [111]. (a) and (b): elastic results, (c) and (d): simulated structures. rms strain levels same as Fig. 4.1. (01$\bar{1}$), ($\bar{1}$10), (2$\bar{3}$1) and ($\bar{2}$11) plane traces are shown.

In the calculations of gamma surfaces no stable minima were found other than that corresponding to the Anti-Phase Boundaries [49]. This means that no true dissociation of a $\langle 100 \rangle$ dislocation is expected. However, in the γ surfaces the directions for which the gamma surface increases less with the magnitude of the fault vector were identified in [49].

Table 4.1 is a reproduction from Ref. [50], which indicates the directions of lowest energy increase obtained for the different crystallographic planes. It is generally accepted that usually true dissociation of the core into partial dislocations occurs only when the gamma surface presents a minimum corresponding to a stable fault[32]. Dislocation core spreading, on the other hand, does not necessarily correspond to a true minimum in the gamma surface. However, the spreading of the dislocation cores along certain planes is expected to be along the directions of lowest energy increase in the γ surfaces. This is indeed true in most cases presented here (Table 4.1).

4.4 Results of the Core Structures of $\langle 110 \rangle \{011\}$ Slip System

The role of $\langle 110 \rangle$ dislocations in the deformation of NiAl has not been clearly established. $\langle 110 \rangle$ dislocation segments have been suggested to form as the sessile reaction product of mobile $\langle 100 \rangle$ dislocations [39], and have alternatively been reported [38, 39, 45] to contribute to the deformation of NiAl. The screw orientation has been suggested to be more mobile than the edge segment, and the slip plane has been determined to be $\{110\}$. The simulation result of a [110] screw dislocation is shown in Fig. 4.10, in which mixed effect is also present. It shows that the screw component of the strain field Y1 is mainly spread on the $(1\bar{1}0)$ plane, and that there is a nascent dissociation of the type $1/2[111] + 1/2[11\bar{1}]$ with a corresponding very narrow band of $(1\bar{1}0)$ APB in between. Simple elastic calculations are also in agreement with this finding. The edge component Y2 has some spreading on the (001) plane and this may preclude easy glide on the $(1\bar{1}0)$ plane. Indeed this configuration is able to stand the stress of about $8 \times 10^{-2}\mu$ without slipping. The core structure of the [110] edge dislocation is very similar to the screw orientation, as shown in Fig. 4.11. The mixing effect is negligible. The Peirels stress is almost same as the one for screw orientation (Table 4.2).

Table 4.1: Directions of lowest energy increase for γ surfaces in various planes[49]

γ surface planes	Directions of lowest energy increase	
(110)	$[1\bar{1}0]$	
(112)	$[\bar{1}\bar{1}1]$	↓
(123)	$[\bar{3}\bar{6}5]$	
(210)	$[1\bar{2}0]$	higher energy
(122)	$[2\bar{1}0]$	γ surfaces
(111)	$[11\bar{2}]$	
(100)	[010]	↓

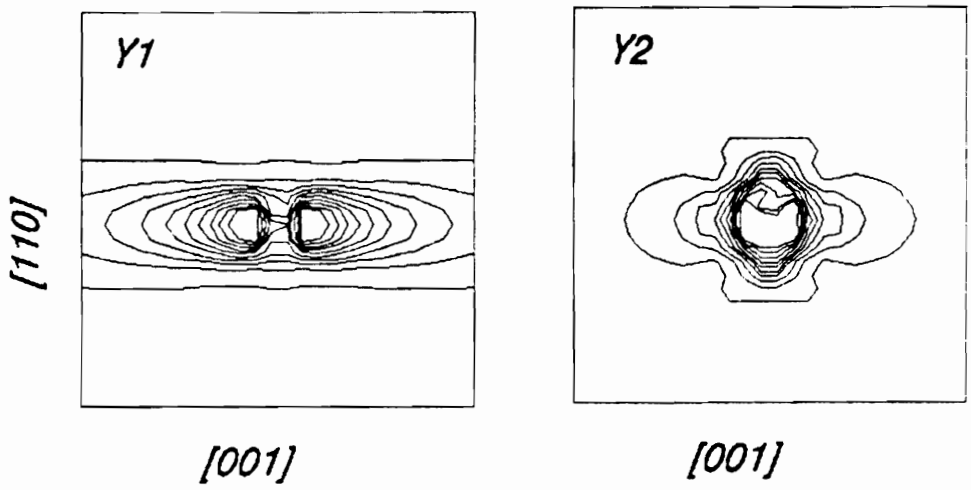

Figure 4.10: Pure screw ⟨110⟩ dislocation. Left: invariant Y1, right: invariant Y2 from mixing effect.

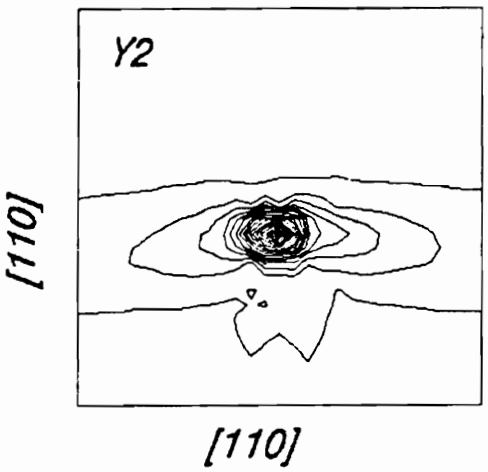

Figure 4.11: Pure edge ⟨110⟩ dislocation

4.5 Results of Peierls Stresses

The stresses were applied in correspondence to the burgers vector $\bar{b}$ and the line direction ξ of the dislocation according to Peach-Koehler formula [26]

$$\bar{F} = (\bar{b} \cdot \bar{\bar{\sigma}}) \times \bar{\xi} \tag{4.1}$$

where F is the force per unit length applied to the dislocation. The stress components that drive the edge and screw parts of mixed dislocations were taken as proportional to the respective components of the Burgers vector. If the dislocation line is located along the z axis and the slip plane is the zx plane the stress tensor is given by:

$$\bar{\bar{\sigma}} = \begin{pmatrix} 0 & \sigma_{12} & 0 \\ \sigma_{12} & 0 & \sigma_{23} \\ 0 & \sigma_{23} & 0 \end{pmatrix} \tag{4.2}$$

Peierls stresses were calculated for all the cores shown above and a few more orientations of the dislocation line. We would like to note that the values of Peierls stresses should be taken as only semi-quantitative. It is well known that the stresses calculated using atomistic simulation are usually higher than experimental values and although in the present work we have used an improved method for the treatment of the boundary conditions the values may still be generally too high. The importance of these calculations is in the analysis of the relative ease of motion of the various dislocations and not on the absolute values of the stresses necessary to move them. Table 4.2 shows a summary of the results for all the cases considered. For the sake of completeness, the table also includes the Peierls stresses for several $\langle 100 \rangle$ dislocations having more screw component than those pictured, as well as the values for the $\langle 111 \rangle$ dislocations which will be discussed in the next chapter.

Table 4.2: Computed Peierls stresses for stoichiometric NiAl

b	x	y	z	$\sigma(\times 10^{-2}\mu)$	$\sigma(MPa)$
[100]	[100]	[001]	[0$\bar{1}$0]	1.11	1387.5
[100]	[$\bar{2}$10]	[001]	[120]	0.63	790.0
[100]	[110]	[001]	[1$\bar{1}$0]	1.26	1570.0
[100]	[$\bar{1}$20]	[001]	[210]	1.89	2360.0
[001]	[100]	[010]	[001]	1.00	1250.0
[100]	[100]	[01$\bar{1}$]	[011]	0.36	450.0
[100]	[$\bar{4}$11]	[01$\bar{1}$]	[$\bar{1}\bar{2}\bar{2}$]	0.38	460.0
[100]	[$\bar{2}$11]	[01$\bar{1}$]	[111]	1.23	1540.0
[100]	[$\bar{1}$11]	[01$\bar{1}$]	[211]	0.66	830.0
[100]	[0$\bar{1}\bar{1}$]	[01$\bar{1}$]	[100]	0.31	380.0
[110]	[001]	[1$\bar{1}$0]	[110]	6.28	7860.0
[110]	[110]	[1$\bar{1}$0]	[00$\bar{1}$]	6.54	8180.0
[111]	[1$\bar{1}$0]	[11$\bar{2}$]	[111]	5.03	6290.0
[111]	[11$\bar{2}$]	[1$\bar{1}$0]	[111]	5.76	7202.4

4.6 Concluding Remarks

The core structures of the ⟨100⟩ and ⟨110⟩ dislocations in NiAl have been presented. By applying the method of representing strain tensor invariants extrapolated from the computer simulation, as described in Chapter 3, we have been able to discuss consistently the dislocation core structures. This method is able to separate discrete core effects from elastic ones, and easy to identify the crystallographics of the dislocation field for the discrete configurations.

The core spreading of ⟨100⟩ and ⟨110⟩ dislocations in NiAl, can occur along a variety of planes with a very high probability of non planar structures. The strain spreading is not necessarily along compact planes or relatively low Miller indices, however the nearest, low Miller indices, plane traces to each high strain lobe, are indicated in the figures. The planes involved depend on dislocation slip plane and line orientation. Also, the elastic solution generally determines the shape of the contour lines for the lattice strain field far from the dislocation core. However, the discrete character of the lattice imposes two main differences between "elastic" and "discrete" strains. First, as expected, the high strain levels imposed by the continuum solution at the dislocation core are lowered considerably in the relaxed structures. Secondly, for several cases among those studied, the strain in the simulated results extend asymmetrically with respect to the origin, in contrast to the symmetry of the elastic solution. This is a lattice effect analogous to the twinning-antitwinning asymmetry on glide reported earlier for the 1/2[111] screw dislocation in bcc metals (Vitek, 1974 [32]).

Chapter 5

Core Structure of Metastable ⟨111⟩Dislocations *

5.1 APB and Metastable Dislocations

For most orientations, NiAl deforms by ⟨100⟩ slip as discussed in Chapter 4. It is known that the ⟨100⟩ slip does not present five independent systems required for the material to be ductile (von Mises' criterion). A possible way to improve ductility in this material is to try to stabilize ⟨111⟩ slip. For this reason, a study of the core structure of ⟨111⟩ dislocations has been carried out. Since these dislocations are observed mostly in screw orientations, the focus of the study has been on the dislocations of pure screw character.

The experimental observations of deformations of NiAl reveal that the complete ⟨111⟩ dislocations exist in this material and there is no splitting into 1/2⟨111⟩ superpartials with an APB in between [41] [39] [40]. These observations are in agreement with the previous simulations of these dislocations [51]. The ⟨111⟩ dislocations are stable with respect to the dissociated configurations involving an APB.

The energetics and stability of the dissociated structure is largely influenced by the value of the APB energy. Another important factor in the understanding of the dislocation core structure is the shape of the γ surface in slip plane and the other possible planes for core spreading. In

*Based on Computer Simulation of the Core Structures of Metastable ⟨111⟩ Dislocations in NiAl, by Z. Xie, C. Vailhe, and D. Farkas, *Mater. Sci. Eng. A170*, 1993, pp. 59-65.

previous work [49] we have computed these γ surfaces in different planes including (110) and (112) with particular interest in the vicinity of the APB. The important features of the γ surfaces in these planes are the minimafound in the APB region, which are deviated from the $1/2\langle 111\rangle$ position in both planes. For the $\{110\}\gamma$ surface the $1/2\langle 111\rangle$ fault is an unstable maximum. Two minima occur on both sides of the $1/2a[1\bar{1}1]$ fault, deviated in the $[1\bar{1}0]$ direction. The γ surface in the (112) plane the minimum corresponding to the APB is shifted in the $[\bar{1}\bar{1}1]$ direction from the perfect $1/2a[\bar{1}\bar{1}1]$ position. In the present work, we studied the atomistic structures of the complete $\langle 111\rangle$ dislocation and the metastable dissociations of the complete $\langle 111\rangle$ dislocation into $1/2\langle 111\rangle$ partials and the alternative splitting suggested by the γ surface calculations to have a stable fault between the two partials.

5.2 Simulation of the complete $\langle 111\rangle$ screw dislocation

It is worthwhile to look at the shape of elastic solution of the $\langle 111\rangle$ dislocation for comparison. The shape of elastic solution for the $\langle 111\rangle$ core structure gives hexagonal symmetry and is extended in $\{110\}$ planes (Figure 5.1). In the relaxed structure, the six-fold symmetry of the elastic solution is broken. Two possible core structures are obtained for the complete $\langle 111\rangle$ dislocation after relaxation, depending upon the initial position of elastic center of the dislocation line. These two configurations are not energetically equivalent. The core structure for which the energy is the lowest is presented in Figure 5.2 (a) and the high energy one is presented in Figure 5.2 (b) . These figures represent the contour plot of the invariant Y1 of the strain tensor. The contour plot is superposed to a projection of the lattice. The circles and triangles indicate the presence of an atom in the [111] direction. The nickel and aluminum atoms are depicted by circles and triangles, respectively. Their sizes are proportional to their depth in the sequence of $\{111\}$ planes.

The two possible cores are extended over no more than a few nanometers. The high level deformation is spread approximately over 1nm and constitutes the center of the core. The low level deformation is the deformation around the center of the core and involves only small atomic displacements.

The low level deformation is very similar in these two configurations. It reveals the spreading

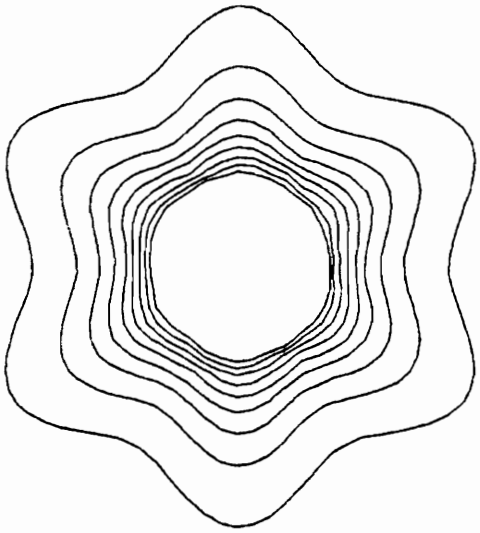

Figure 5.1: Elastic solution for the complete [111] screw dislocation. Crystallographic direction: horizontal - $[1\bar{1}0]$, vertical - $[11\bar{2}]$.

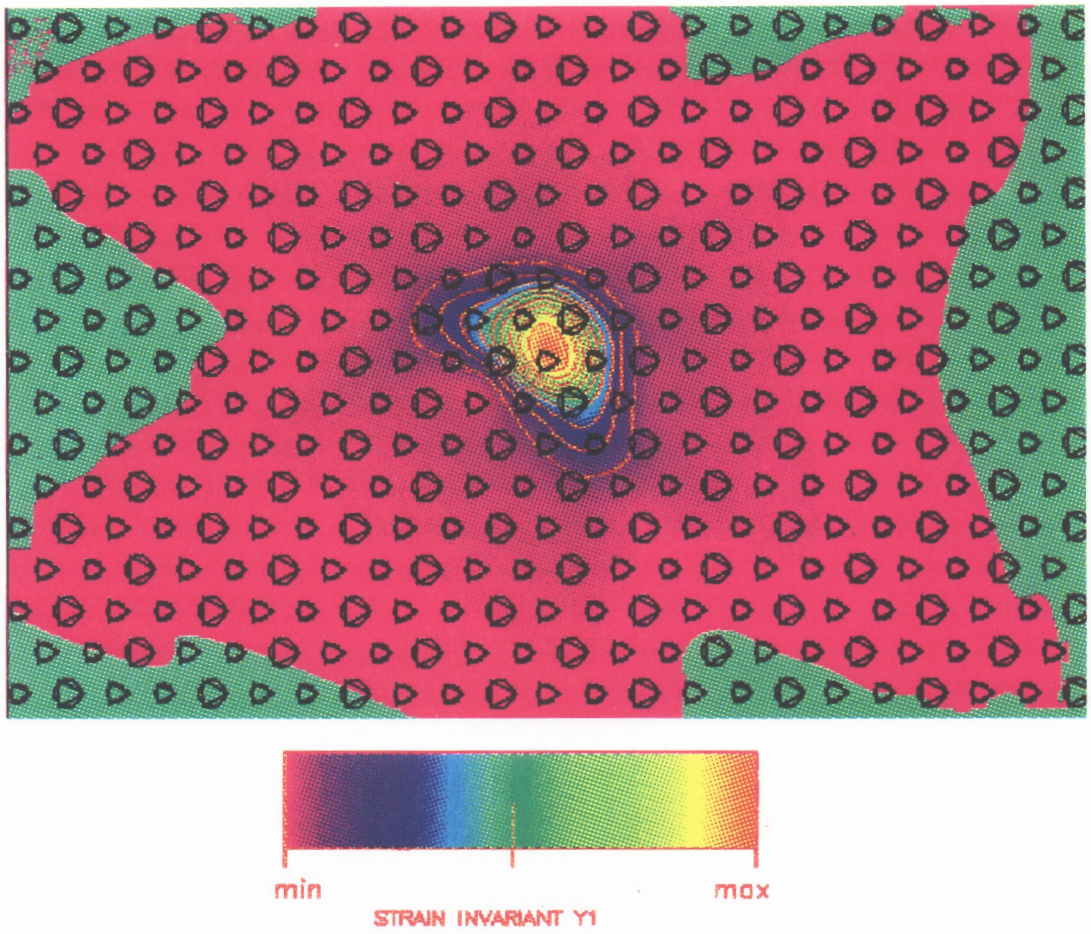

Figure 5.2(a)

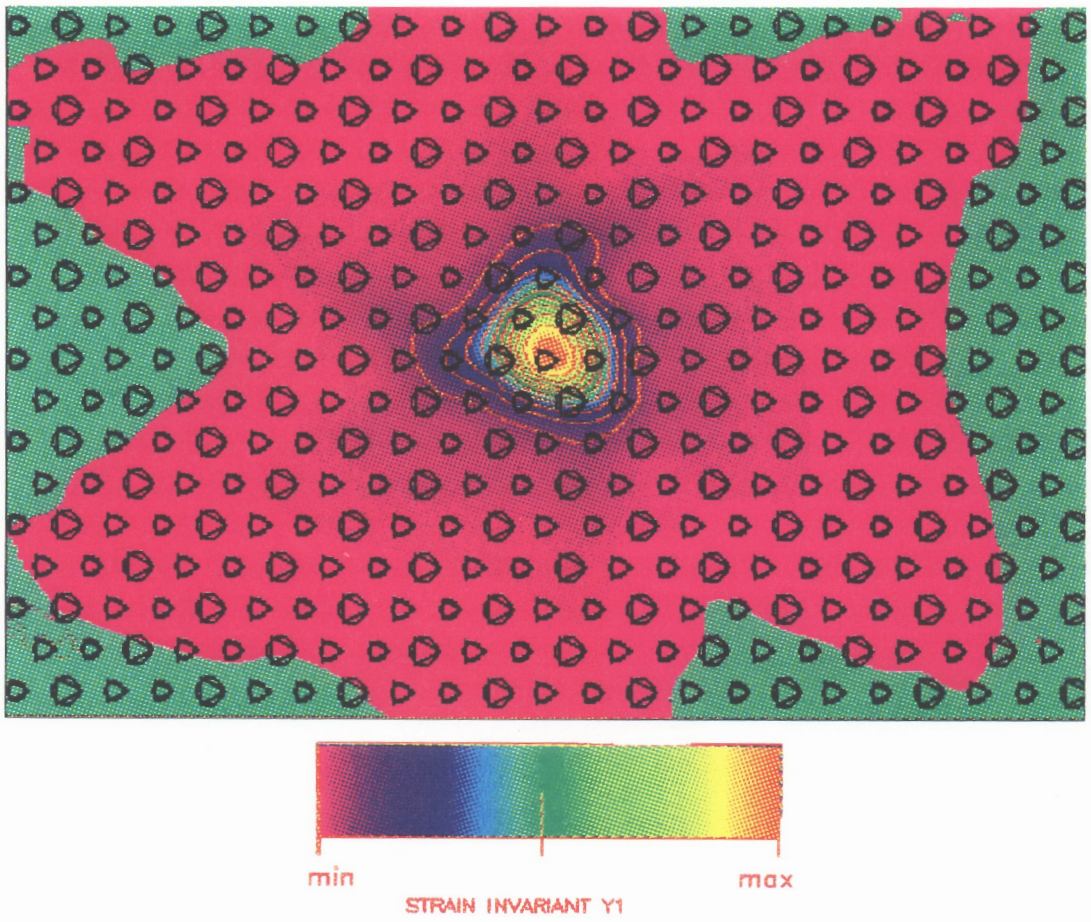

(b)

Figure 5.2: Core structure of the complete [111] dislocation (a) Lower energy structure (b) Higher energy structure. Crystallographic direction: horizontal axis - $[1\bar{1}0]$, vertical axis - $[11\bar{2}]$.

of the core in six $\{110\}$ planes in agreement with the elastic solution.

For the core spreading of the [111] screw dislocation, it is particularly interesting to analyze this structure in terms of the predictions of elasticity theory and the calculated γ surfaces [49]. The complete [111] dislocation has a complex core structure. The low level deformations in the outer regions of the core is spread along the $\{110\}$ planes, as revealed by the plot of the strain tensor invariant Y1. This agrees with the expectations based on a study of various possible γ surfaces and is also given by elasticity theory. The spreading of the center of the core presents different configurations. It is difficult to predict the spreading using the planar fault energy results because the energy of planar faults in the [111] direction in the $\{110\}$, $\{112\}$ and $\{123\}$ planes is very similar. This results in different possible configurations with very similar energy. The two different shapes of the high level deformation is the only factor which explains the energy difference between these two configurations.

The complexity of the high level deformation can be related to details of the γ surface in various planes. For planar faults in the $\langle 111 \rangle$ direction one can consider three possible low index planes i.e. the $\{110\}$, $\{112\}$ and $\{123\}$ planes. For a planar fault vector smaller than 0.08nm, faults in the $\langle 111 \rangle$ directions have a similar energy in each of these three planes [29].

The possibility of glissile dissociations of the $\langle 111 \rangle$ dislocation can be analyzed in terms of the simulated structures. The cores of the complete dislocations and those of the partials dissociated in $\{110\}$ type planes are highly non-planar and therefore sessile. The cores of the partials dissociated in $\{112\}$ type planes are more planar and therefore more glissile. Nevertheless, low level deformations have a tendency to be spread in $\{110\}$ type planes and this constitutes a non planar component of the core structure. In this case we point out an interesting analogy to the behavior of $L1_2$ alloys. In both cases there are two possible dissociation planes. These are $\{100\}$ and $\{111\}$ in the $L1_2$ and $\{110\}$ and $\{112\}$ in the B2 alloys. In the $L1_2$ alloys that present anomalous yield behavior the first of these planes presents the lower energy APB and no possible planar core structure for the partial dislocations. According to the present results for a B2 material there is also a non planar structure for dissociations in the $\{110\}$ planes that have the lower APB and a possible planar structure for the $\{112\}$ planes that have the higher APB energy. This would indicate that if $\langle 111 \rangle$ slip could

be stabilized one would expect anomalous yield behavior.

The calculated Peirels stresses of the $\langle 111 \rangle$ dislocations are $6.29 \times 10^{-2}\mu$) (7862.5MPa) for $\langle 111 \rangle (112)$ slip and $7.18 \times 10^{-2}\mu$) (9003.0MPa) for $\langle 111 \rangle (110)$ slip, respectively, as shown in Table 4.2 in Chapter 4.

5.3 Core Structures of the $1/2\langle 111 \rangle$ Metastable Superpartials Dissociated in a $\{110\}$ Plane

The $1/2\langle 111 \rangle$ superpartials have not been experimentally observed and as mentioned above these dislocations are expected to be unstable. The superpartials are simulated in order to study the factors which influence their stability. The simulations were carried out for two superpartials separated by different distances along the $\{110\}$ or $\{112\}$ planes.

The $1/2\langle 111 \rangle$ superpartials always present a low level deformation spreading in the $\{110\}$ planes. However, the center of the core is complex and presents some extension in the $\langle 110 \rangle$ and $\langle 112 \rangle$ directions depending upon the APB involved and the distance of separation.

Figures 5.3 presents the core structures of two superpartials separated by 1nm APB along a $\{110\}$ plane. The two superpartials are symmetric with respect the $\{112\}$ plane perpendicular to the APB. An alternative splitting of the complete dislocation in the $(1\bar{1}0)$ plane was also studied. This splitting is such that the fault corresponds to the stable faults in the $(1\bar{1}0)$ plane, as given by the γ surface. Figure 5.4 shows this alternative splitting. It is given by the reaction:

$$[111] \Rightarrow 1/10[445] + 2/10[110] + 1/10[445] \tag{5.1}$$

Figure 5.5 presents the superpartial core structures for this case.

5.4 Core Structures of the $1/2\langle 111 \rangle$ Metastable Superpartials Dissociated in a $\{112\}$ Plane

The two superpartials with a $\{112\}$ APB in between are not symmetric. The core structure

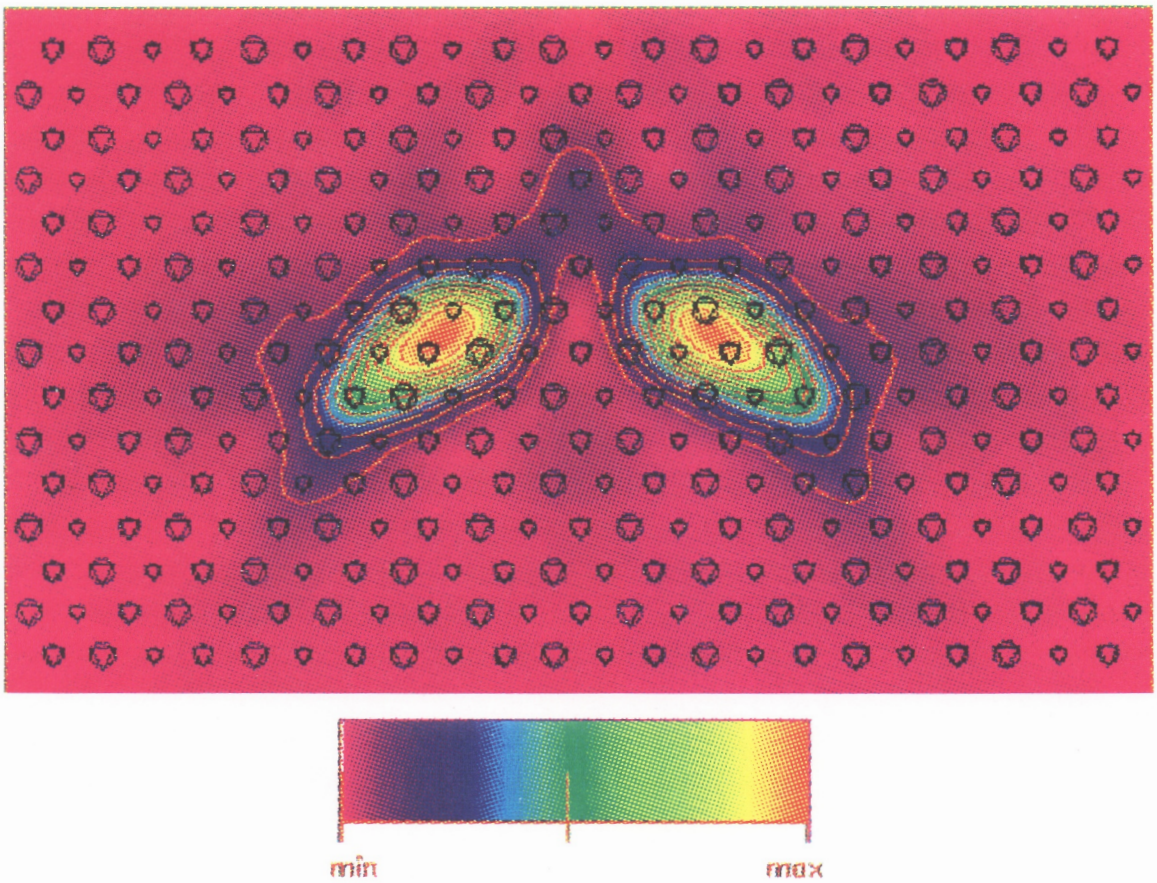

Figure 5.3: Core structures of the $1/2\langle 111\rangle$ metastable superpartials dissociated in a $\{110\}$ plane separated by 1nm APB. Crystallographic direction: horizontal axis - $[11\bar{2}]$, vertical axis - $[1\bar{1}0]$.

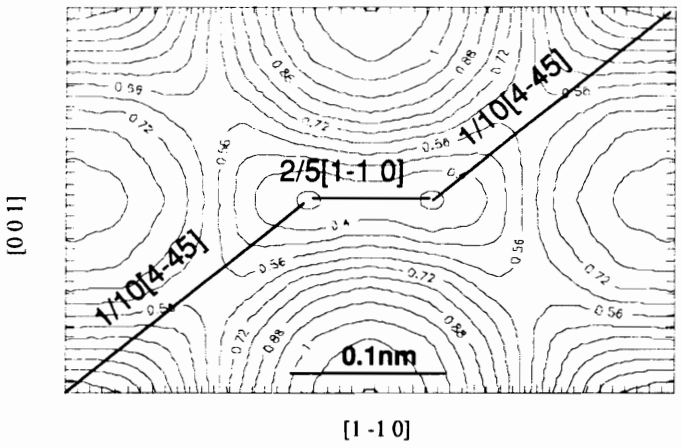

Figure 5.4: Alternative splitting of the [111] screw dislocation in {110} type planes.

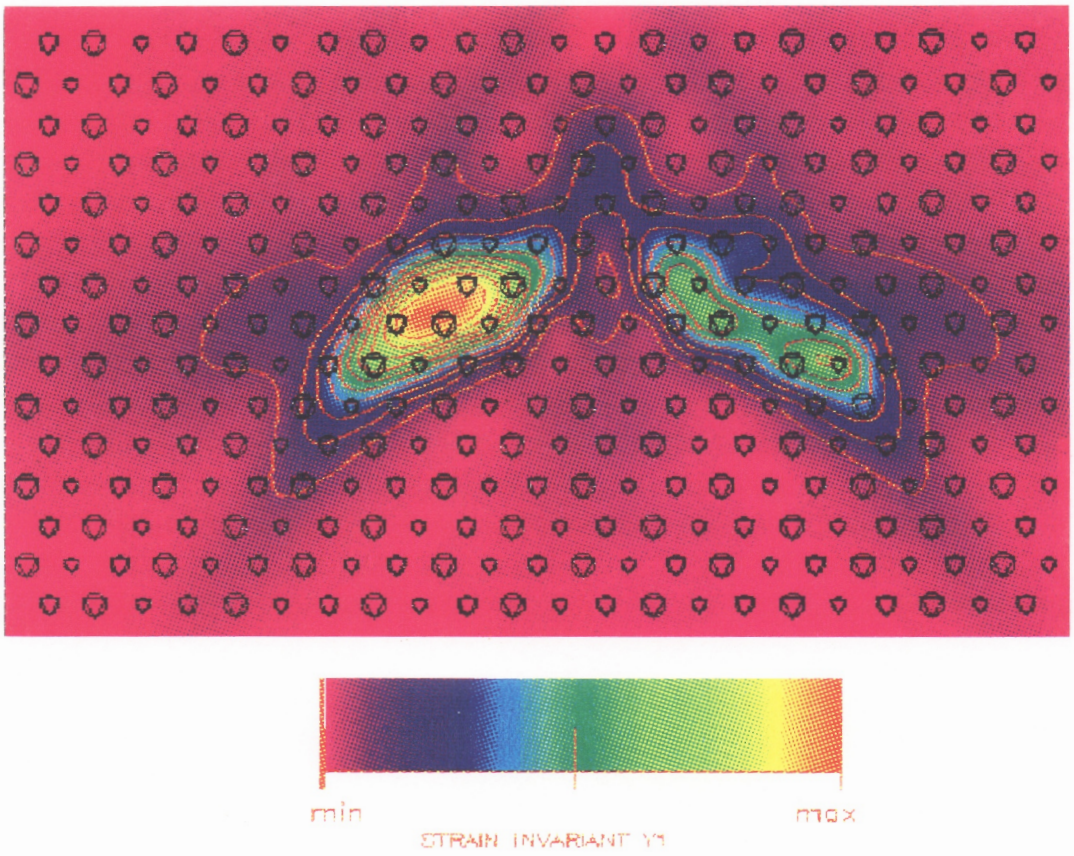

Figure 5.5: Structure of 1/10[445]+2/10[110]+1/10[445] screw superpartials separated by 1nm APB along a {110} plane. Crystallographic direction: horizontal axis - $[11\bar{2}]$, vertical axis - $[1\bar{1}0]$.

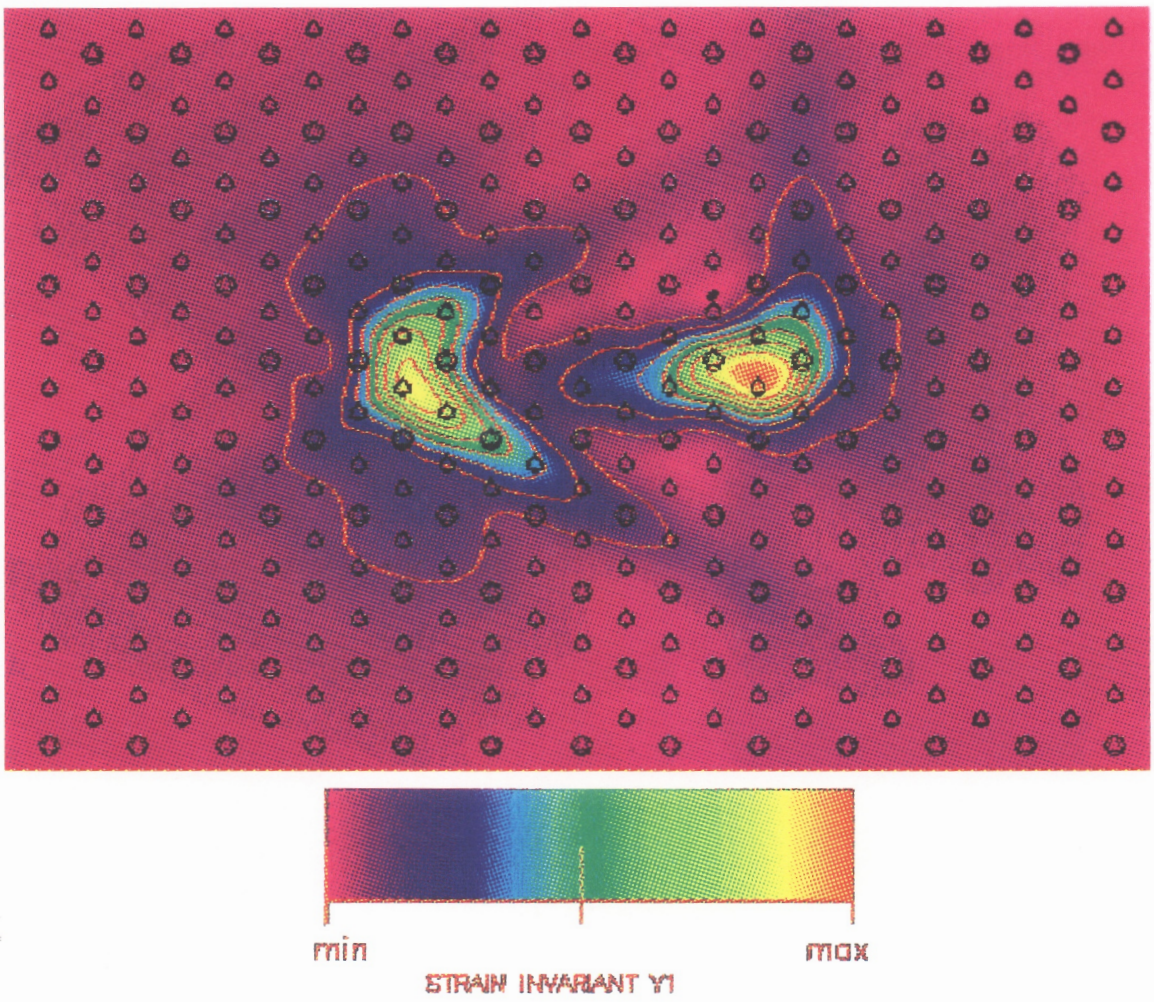

Figure 5.6: Structure of 1/2[111] screw superpartials separated by 2.2nm APB along a {112} plane. Crystallographic direction: horizontal axis - $[1\bar{1}0]$, vertical axis - $[11\bar{2}]$.

is shown in Figure 5.6 for a separation of 2.2nm.

The superpartial pair which creates a $\{112\}$ APB fault is expected to be less stable than the pair which involves the $\{110\}$ APB because the $\{112\}$ APB has higher energy than the $\{110\}$ plane [51]. One of the superpartials spreads in two $\{110\}$ planes and the other spreads in the $\{112\}$ APB. The partials become more planar when separation increases.

According to the γ surface results the exact minimum for the APB fault is obtained for the Burgers vectors $5/11a\langle 111\rangle$ in the twinning sense and $6/11\langle 111\rangle$ in the antitwinning sense in the $\{112\}$ planes. The $1/2\langle 111\rangle$ superpartials are in one case too large and in the other too small. As a result, the core of one superpartial is spread in the $\{112\}$ plane. Inversely, the other partial is constricted along the APB plane. These observations correspond to the adjustment of the lattice to the real minimum of the APB fault.

The alternative splitting that creates a fault that is stable according to the γ surface in this plane is given by the reaction:

$$[111] \Rightarrow 6/11[111] + 5/11[111] \tag{5.2}$$

This splitting is depicted in γ surface (Figure 5.7). Figure 5.8 shows the two superpartial core structures obtained for this alternative splitting.

The core structure changes versus the distance between the two superpartials are evaluated. In the simulations, the centers of the superpartials shifted from their initial elastic centers due to their metastable nature. For large distances of separation, the superpartials are attracted and move to minimize their separation. When the dislocations move, their core structures are spread in the $\langle 110\rangle$ or $\langle 112\rangle$ directions. For small distances of separation, the core structures are less extended and the superpartials have a tendency to repulse each other. Elastic theory predicts an equilibrium position for a distance of 1.7 nm between the superpartials. A local minimum seems to exist in the vicinity of this value in the energy of the superpartials system.

The variation of energy as a function of the final position of the two superpartials can be obtained by subtracting the energy of the system containing the complete [111] dislocation from the system containing the two superpartials. The pair of $1/2[111]$ superpartials always has higher energy than the system constituted of $6/11a[111]$ and $5/11a[111]$ Burgers vectors.

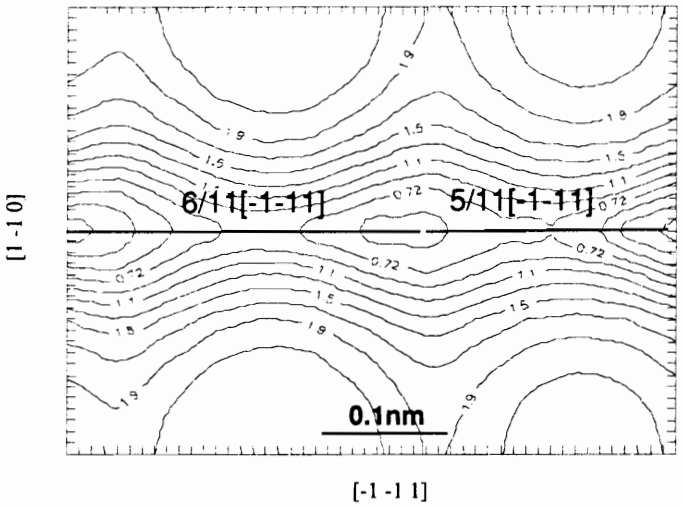

Figure 5.7: Alternative splitting of the [111] dislocation in {112} type planes.

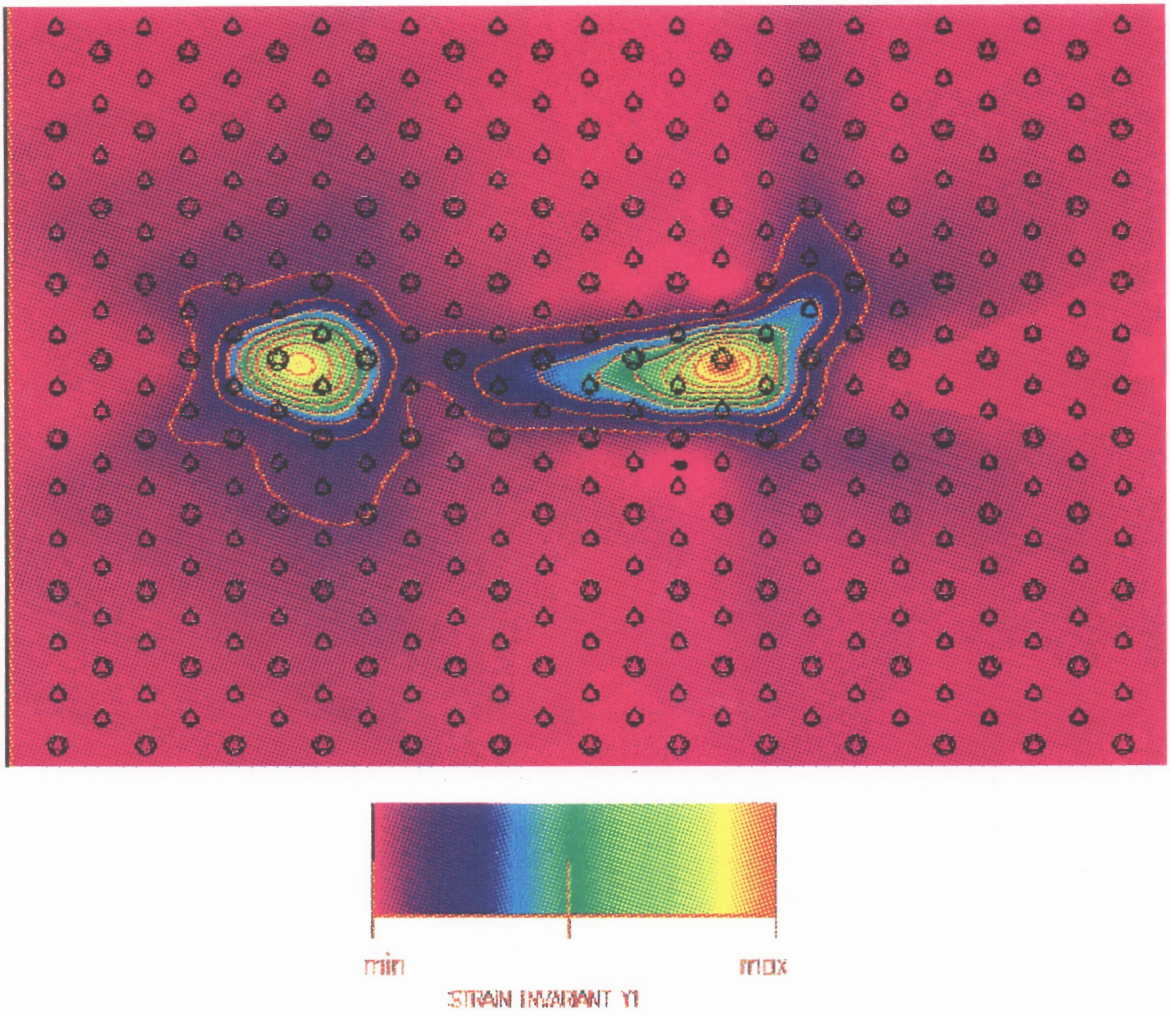

Figure 5.8: Structure of 6/11 [111] + 5/11 [111] screw superpartials in the {112} plane with 2.2nm separation. Crystallographic direction: horizontal axis - $[1\bar{1}0]$, vertical axis - $[11\bar{2}]$.

However, both pairs of superpartials are still unstable because they do not show any stable position with respect to the low energy configuration of the complete [111].

The core spreading of the simulated metastable 1/2[111] superpartials depends upon the distance which separates the superpartials. However, low level deformation always exhibits core spreading in the {110} planes This can be understood also in terms of the γ surface results and elasticity theory.

According to the computation of the γ surfaces in the (110) and (112) planes, two alternative splittings of the $[1\bar{1}1]$ dislocation are proposed. First, the (110) γ surface shows two stable energy minima around the $1/2a[1\bar{1}1]$ fault. Second, the (112) γ surface presents a stable energy minimum deviated of the $1/2a[\bar{1}\bar{1}1]$ fault in the twinning sense. These alternative dissociation reactions were simulated and the results show that the energetics of both these dissociations are indeed more favorable than the dissociation that leaves an exact APB between the partials. However, the dissociated configuration is still unstable with respect to the complete dislocation.

The present results for the core structure of $1/2\langle 111\rangle$ dislocations in B2 alloys are different from the results obtained for the same Burgers vectors in bcc materials [32] and the results obtained for the same crystal structure with model pair potentials [52] [53]. In these cases the dislocation core was always spread in the three {110} type planes and the spreading in {112} planes only occurred under stress. This may be due to the different interatomic potential used in the present work but not to the metastable nature of the superpartials in NiAl. For the superpartials with {110} APB, when the distance between the two superpartials is large, both cores begin to spread more in the {110} APB plane (see Figure 5.3 and Figure 5.9b). This spreading is not observed for closer superpartials. There is a tendency that the dislocations prefer to slip in the {112} planes. Actually, Figure 5.9 shows that the dislocations bonding an APB in {110} planes tend to move in the {112} type planes under the applied stresses.

5.5 Concluding Remarks

The core structure of the complete $\langle 111\rangle$ dislocations in NiAl is highly non planar and difficult to move. The complete dislocation is stable with respect to splitting into exact $1/2\langle 111\rangle$ partials and also with respect to alternative splittings that correspond to the stable

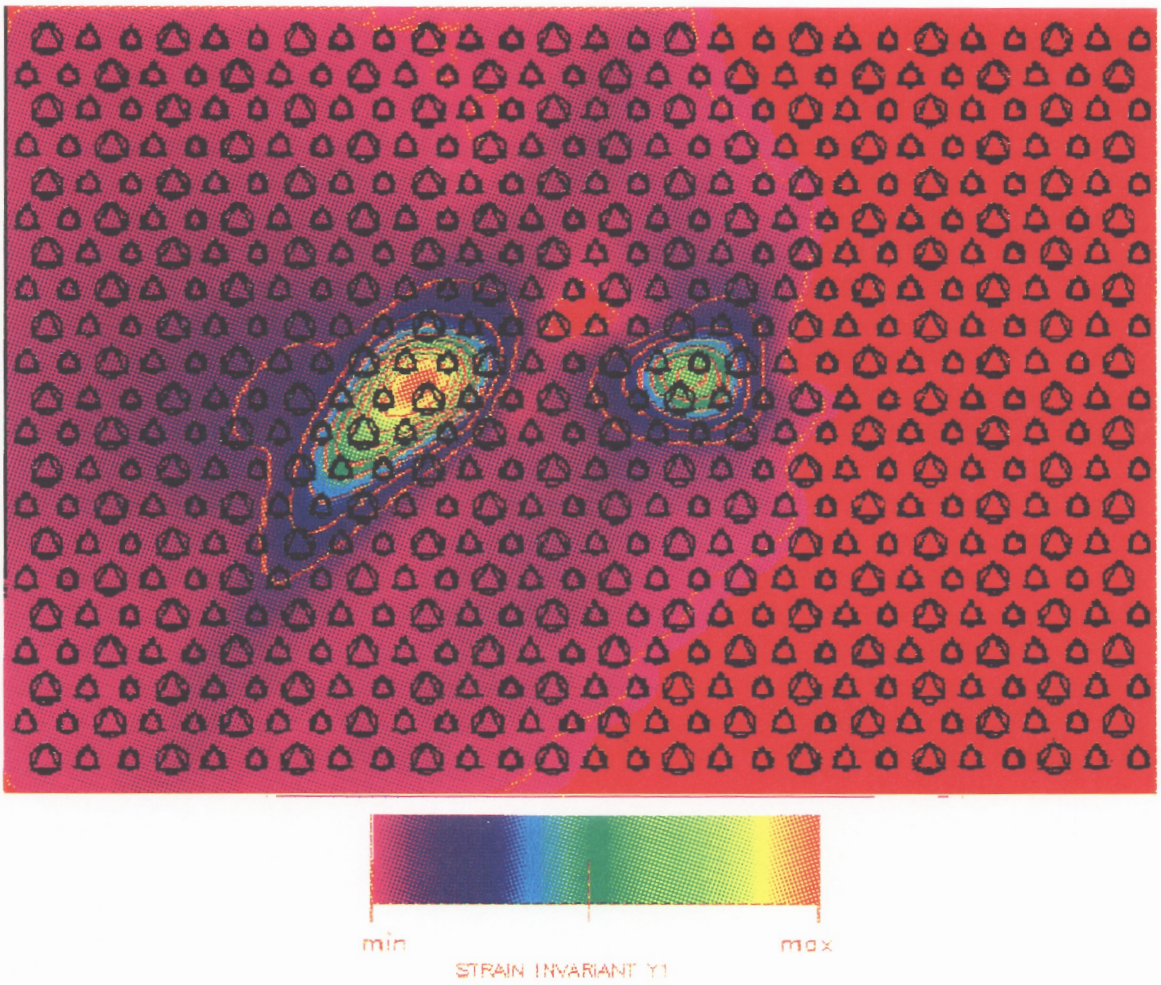

Figure 5.9(a)

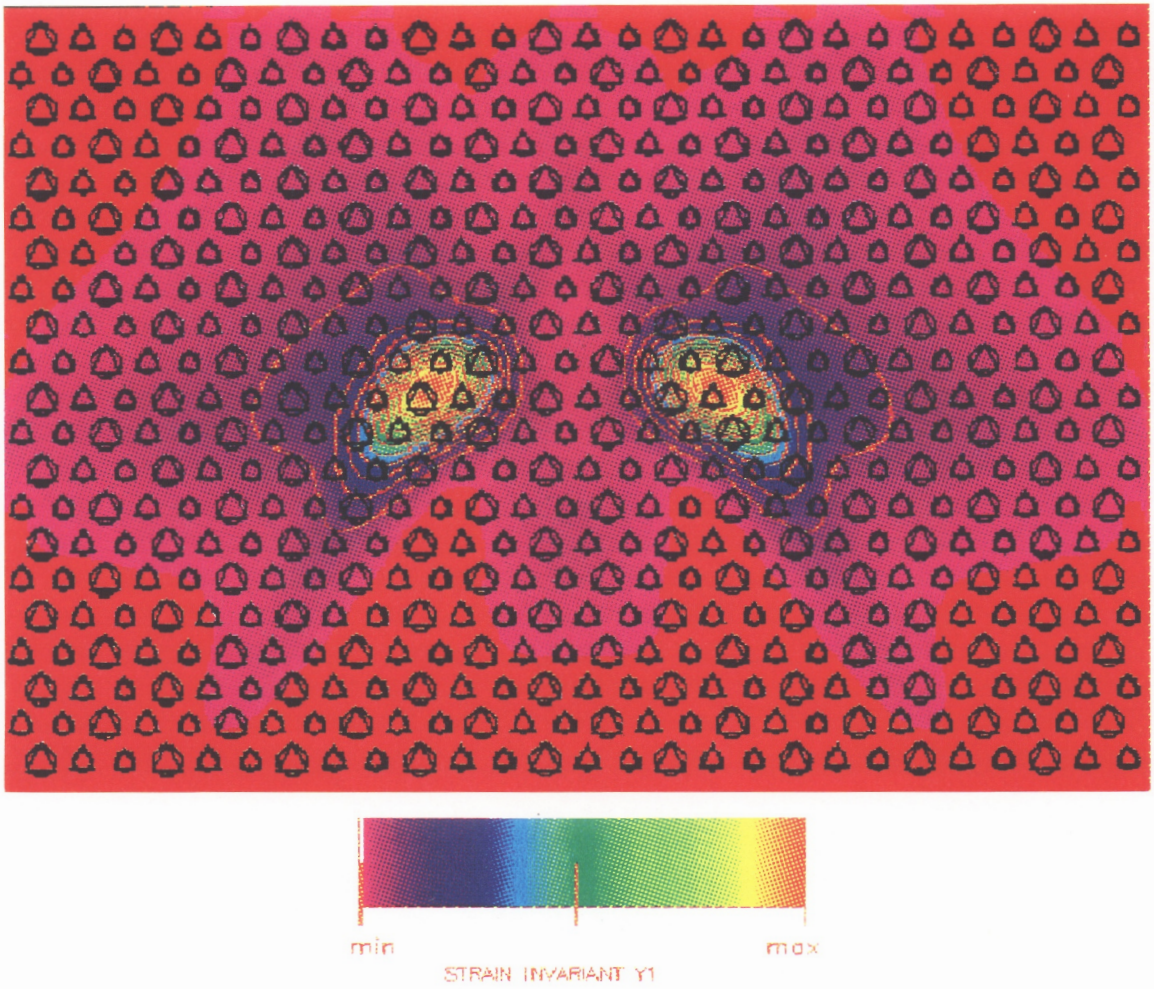

Figure 5.9(b)

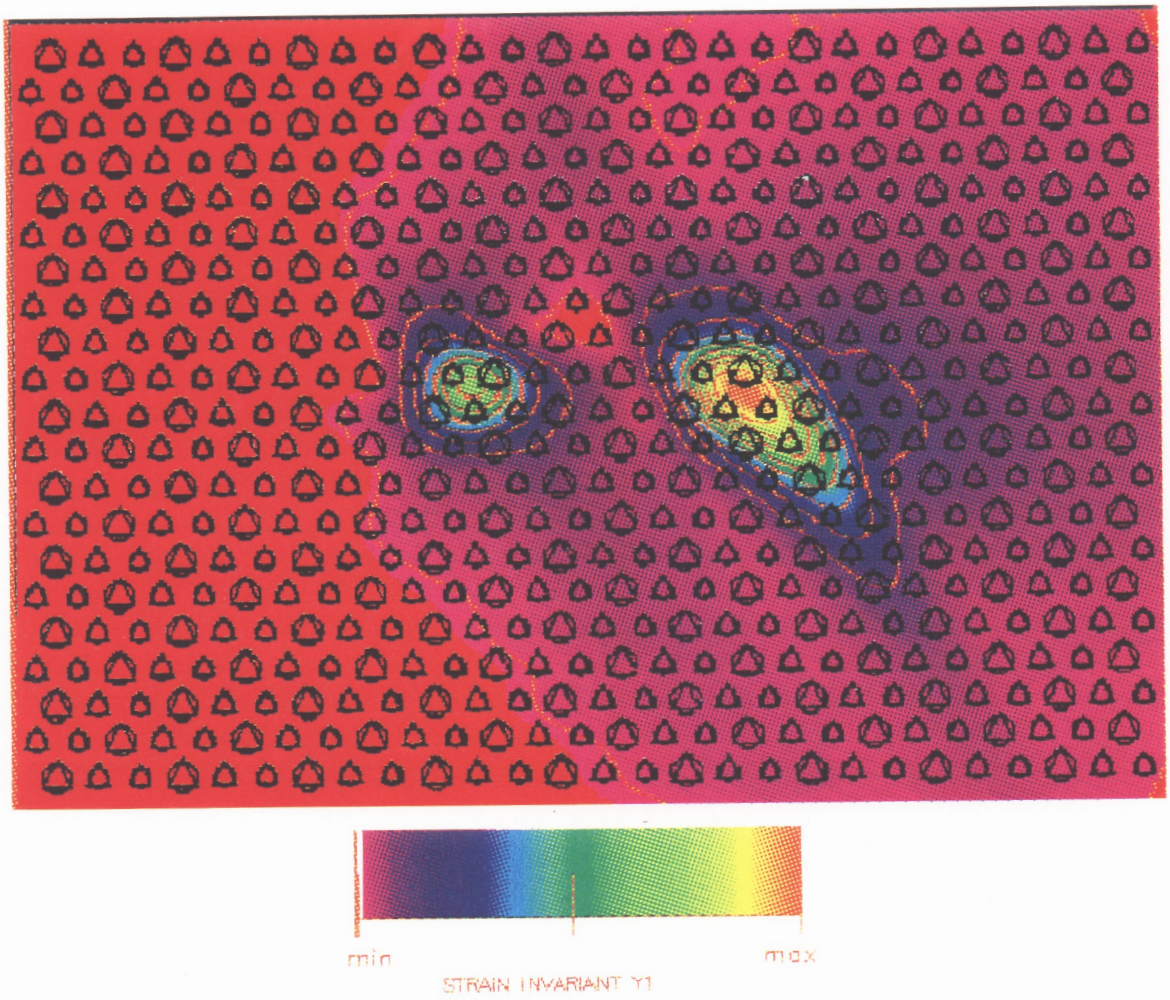

(c)

Figure 5.9: Effects of stress on the core structure of 1/2[111] screw superpartials with 1.5nm {110} APB. (a) stress that induces glide toward the left, (b) without stress, and (c) stress that induces glide toward the right. Crystallographic direction: horizontal axis - $[11\bar{2}]$, vertical axis - $[1\bar{1}0]$.

fault in the vicinity of the APB, in both $\{110\}$ and $\{112\}$ planes. However, the alternative splitting has lower energy than the splitting in exact $1/2\langle 111\rangle$ partials. The structure of these metastable partials is also non-planar and it is different from the structure observed in bcc metals and in B2 materials described by model pair potentials.

Chapter 6

Effects of Disorder on the Dislocation Core Structures

This chapter is divided in three sections:

Structure of Vacancies in Ni-Al Intermetallics

Effects of Local Disorder on the Core Structures

Dislocation Core Structures in Off-stoichiometric NiAl

6.1 Structure of Point Defects in Ni-Al Systems *

A knowledge of the energetics and the atomic displacements around vacancies and other point defects is important for the study of several physical and mechanical properties of crystals as well as for the interpretation of various experimental studies. Structural vacancies have been experimentally observed in NiAl [56] as well as a very high rate of hardening with stoichiometric deviations in this alloy [57]. Also, only Ni-rich Ni_3Al can be ductilized by B additions [58]. The study of point defects in this system is necessary in order to understand these types of behavior. Point defects are also important in the understanding of material behavior under irradiation and diffusion mechanisms.

For the calculation of the point defects it is essential to use a method which takes into account the discrete nature of the lattice. This has been done in the past by using a semi-discrete model, in which the lattice in a small region near the defect is treated as discrete while the rest of the lattice is replaced by the continuum [59, 60]. The accuracy of this method would obviously increase with the size of discrete region. Kanzaki [61] proposed an approach to account for the overall discrete nature of the lattice in the static point defect problem based upon the Born-von Karman model of the lattice. A Green function method, basically equivalent to the Kanzaki approach, was further developed by Tewary [62]. With the availability of increasing computer power and more accurate interatomic potentials, atomistic computer simulation is now a possible straightforward method for the study.

Most of the atomistic calculations pertaining to the nature of point defects in metals up to recently were based on pairwise potentials. This section presents a study of various point defects and their interactions and the relaxation associated with them for Ni_3Al and NiAl using atomistic computer simulation with the EAM interatomic potential [16]. The simulations include vacancies, divacancies and antisite defects, as well as increasing levels of disorder by adding a random distribution of antisite pairs in the simulation. These simulations should provide a basis for further understanding of the interaction between point defects and other

*Based on "Structure and Energetics of Vacancies , Antisites, and Di-vacancy Complexes in Ni-Al System", in *High-Temperature Ordered Intermetallic Alloys V*, Eds: I. Baker *et al.*, Proc. Mater. Res. Soc. Symp. vol. 288, 1992, pp.305-311 [54], and "Atomistic Structures and Lattice Effects of Vacancies in Ni-Al Intermetallics", submitted to, *J. Mater. Res.*, by Z. Xie and D. Farkas [55].

defects, as well as the diffusional processes in this alloy system.

For point defect simulation, the crystal is divided into two regions. The atomic coordinates inside a crystal region I, containing the defects, are allowed to relax to find an energy minimum consistent with the boundary atoms position at a region II where anisotropic elasticity is used. The atoms in region II are held fixed during the relaxation process, provided region I is sufficiently large, in other words, rigid boundary conditions are adapted. The same conjugate-gradient method as used for dislocations is employed for finding the minimum of the energy for a given ensemble of atoms. As usual in this type of simulation, the size of the simulation block is large enough to ensure that the results are independent of the size.

The energies are calculated taking into account the different cohesive energy contribution to the total energy of the different type of atoms. For a mono-vacancy, vacancy formation energy $E_v^f = E_{relaxed}(n_{total} - 1) - E_{perfect}(n_{total}) + E_{coh}$, where n_{total} is the number of atoms in the region I. For a di-vacancy, the formation energy E_{2v}^f is obtained in a similar way. For example, the formation energy of Al-Ni di-vacancy $E_{2v}^f(AlNi) = E_{relaxed}(n_{total} - 2) - E_{perfect}(n_{total}) + E_{coh}(Al) + E_{coh}(Ni)$. An antisite defect is created by changing one Al (or Ni) atom in its sublattice to Ni (or Al) atom, for example $E_{ant}^f(Al \rightarrow Ni) = E_{relaxed}(n_{total}) - E_{perfect}(n_{total}) + E_{coh}(Ni)$.

6.1.1 Vacancies in Ni and Al

We first considered the vacancies for pure Ni and Al with the EAM potentials [16]. The vacancy formation energies, 1.56 ev for Ni and 0.63 ev for Al, were used in the construction of the potentials and are therefore a good fit to the experimental data in the development of the potentials [16]. For comparison, these values are shown in Table 6.1 together with the energies of other point defects simulated.

Fig. 6.1 shows the relaxation of the atoms around a mono-vacancy as a function of the distance from the vacancy. As clearly stated by Hull [60], the symmetry requirements on the actual displacements can be described by considering the fictitious concentric spherical shell with radii $\frac{a}{\sqrt{2}}\sqrt{k}$, k = 1, 2, 3, ..., centered about the origin, and a being the lattice parameter. The position of every atom in perfect lattice is on one of these shells. Furthermore, it can be

Table 6.1: Energies of vacancies and antisites in Al, Ni, Ni_3Al and NiAl

	Energy(eV) in Ni sublattice	Energy(eV) in Al
Vacancy in Al	-	0.63
Vacancy in Ni	1.56	-
Cohesive energy in Ni_3Al	4.5	4.8
Cohesive energy in NiAl	4.2	4.4
Vacancy in Ni_3Al	1.64	1.87
Antisite in Ni_3Al	0.46	-0.14
Vacancy in NiAl	1.20	1.03
Antisite in NiAl	1.98	-0.60

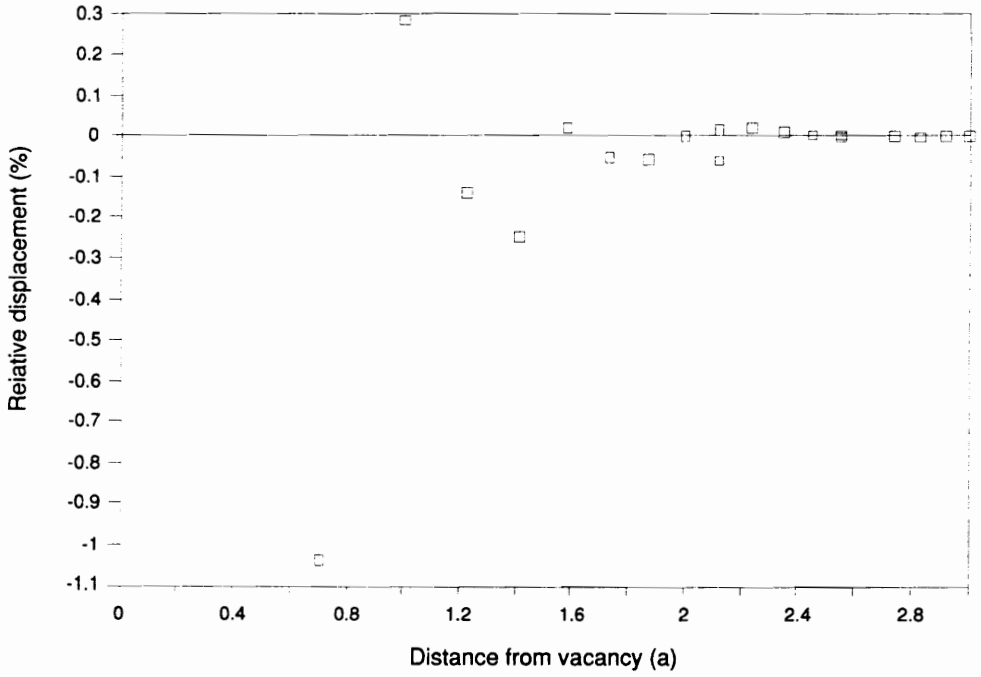
Reiative displacement (%)
0.3
0.2
0.1
0
-0.1
-0.2
-0.3
-0.4
-0.5
-0.6
-0.7
-0.8
-0.9
-1
-1.1
0
0.4
0.8
1.2
1.6
2
2.4
2.8
Distance from vacancy (a)

Figure 6.1(a)

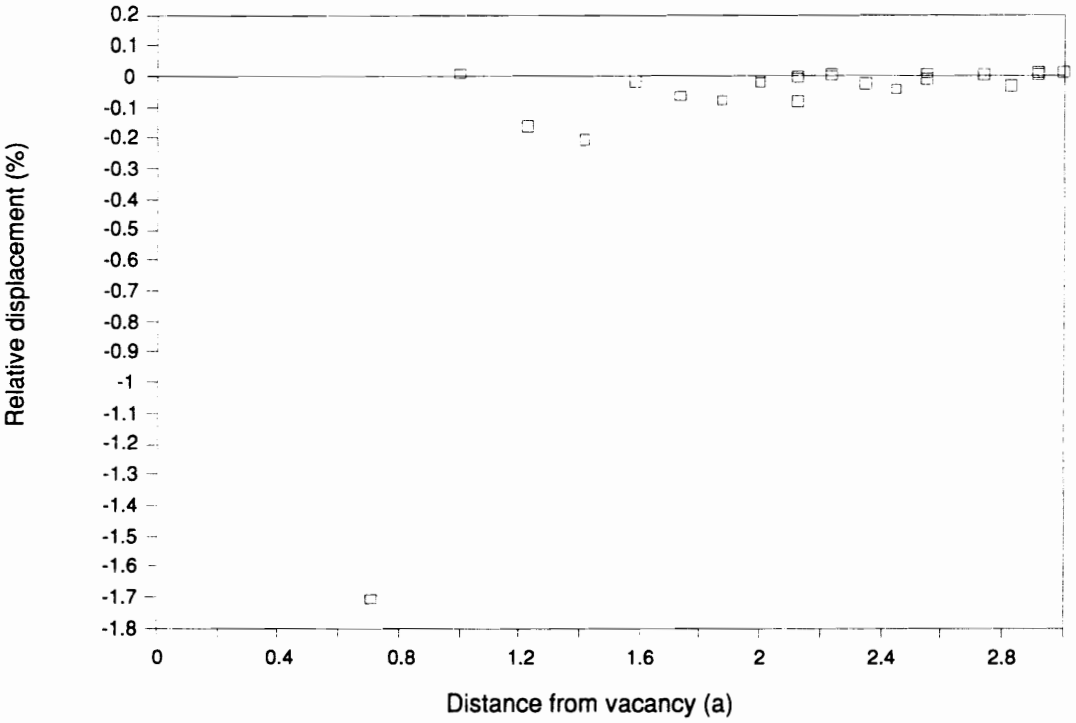

(b)

Figure 6.1: Relaxation around a mono-vacancy in the pure metals, (a) Ni, (b) Al, a is lattice parameter.

shown that there is no atom on the shells with $k = 2_{2i+1}(8j + 7)$ with i, j = 0, 1, 2, ... The atoms on any given shell are distributed on it with cubic symmetry. On the first eight shells, application of the cubic point group takes each atom at least once into all atomic positions in the same shell; i.e., there is only one "type" of atomic position in the first eight shells. The ninth shell has two types. Because of the requirement of cubic symmetry, the atoms that lie on any of the three rotation vectors [100], [110], and [111] can undergo only radial displacements, and all atoms of any one "type" in a given shell must have the same displacement.

Fig. 6.1 shows the relative displacements of different shells. The extent of relaxation is rather small, the nearest neighbors to the vacancy moving inward by 1.04% for Ni, by 2.25% for Al of their distance from the vacancy, and the second nearest neighbors moving outward by 0.28% for Ni and by 0.27% for Al (Table 6.2).

6.1.2 Vacancies in Ni_3Al

The formation energy of the vacancy, 1.64 ev for Ni and 1.87 for Al in Ni_3Al , was also used as part of the fitting procedure in the development of the potentials [16]. The calculated relaxation of the atoms around mono-vacancies in Ni_3Al is shown in Fig. 6.2. Ni_3Al has the Ll_2 ordered crystal structure, which can be described as consisting of four interpenetrating simple cubic sublattices, site (000) and equivalent being referred as sublattice 1, $(\frac{1}{2}\frac{1}{2}0)$ and equivalent as sublattice 2, $(\frac{1}{2}0\frac{1}{2})$ and equivalent as sublattice 3, and $(0\frac{1}{2}\frac{1}{2})$ and equivalent as sublattice 4 in the simulation. One of these sublattices is occupied by Al atoms, therefore, even in the perfect lattice it is not equivalent to the other three. Furthermore, each of them may respond to an applied distortion in different ways, because of the difference in symmetry. The nickel vacancy has 4 aluminum atoms and 8 nickel atoms as nearest neighbors, and 6 pure nickel atoms as the second nearest neighbors. The 4 aluminum and 8 nickel atoms move inward by 2.00%, 0.18% of their distance from the vacancy, respectively.

The second nearest neighbors are not all equivalent due to the differences in local environment. This difference is shown in Figure 6.3. The second nearest neighbors move outward 0.57% for the atoms at the positions $(\bar{1}00), (100)$, and 0.24% for the atoms at the position $(0\bar{1}0), (001), (00\bar{1})$ and (010). For the Al vacancy, the relaxation behaviour of the first shell is

Table 6.2: Relative displacement ($\frac{\Delta d}{d_p}$, %) around mono-vacancies and antisite defects in Ni_3Al

Type	1st shell	2nd	3rd	4th
pure Ni	-1.04	0.28	-0.14	-0.25
pure Al	-2.25	0.27	-0.31	-0.80
Ni in Ni_3Al	-2.00(Al)	0.24(Ni)	0.13(Ni)	-0.35(Ni)
	-0.18(Ni)	0.57(Ni)	-0.14(Al)	-0.09(Ni)
Al in Ni_3Al	-1.71(Ni)	0.01(Al)	-0.16(Ni)	-0.21(Al)
Ni substitute Al	-0.95(Ni)	-0.25(Al)	-0.16(Ni)	-0.19(Al)
Al substitute Ni	2.58(Al)	0.07(Ni)	0.19(Ni)	-0.00(Ni)
	0.57(Ni)	0.03(Ni)	0.09(Al)	0.36(Ni)

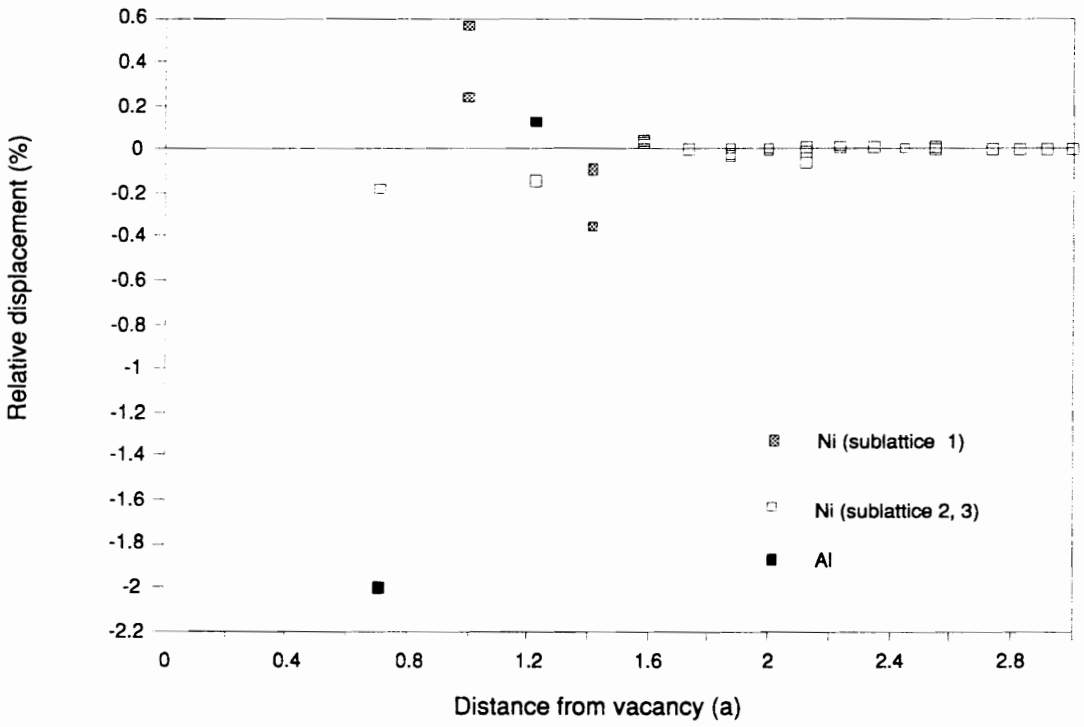
Relative displacement (%)
0.6
0.4
0.2
0
-0.2
-0.4
-0.6
-0.8
-1
-1.2
-1.4
-1.6
-1.8
-2
-2.2
0
0.4
0.8
1.2
1.6
2
2.4
2.8
Distance from vacancy (a)
Ni (sublattice 1)
Ni (sublattice 2, 3)
Al

Figure 6.2(a)

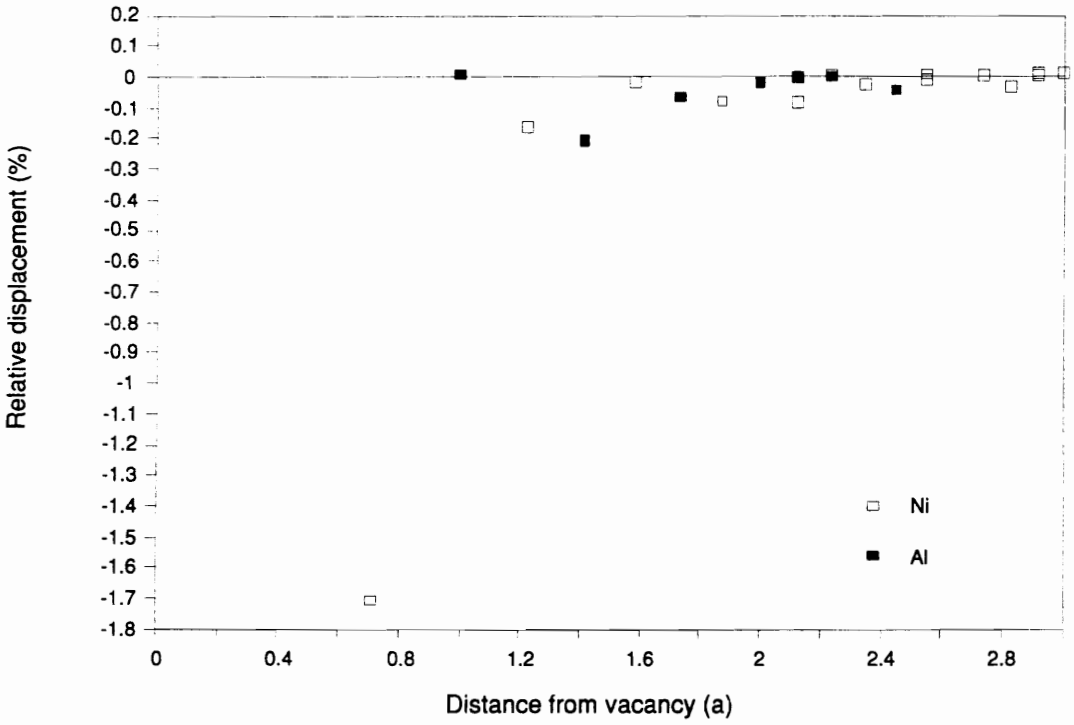
Relative displacement (%)
0.2
0.1
0
-0.1
-0.2
-0.3
-0.4
-0.5
-0.6
-0.7
-0.8
-0.9
-1
-1.1
-1.2
-1.3
-1.4
-1.5
-1.6
-1.7
-1.8
0
0.4
0.8
1.2
1.6
2
2.4
2.8
Distance from vacancy (a)
Ni
Al

Figure 6.2(b)

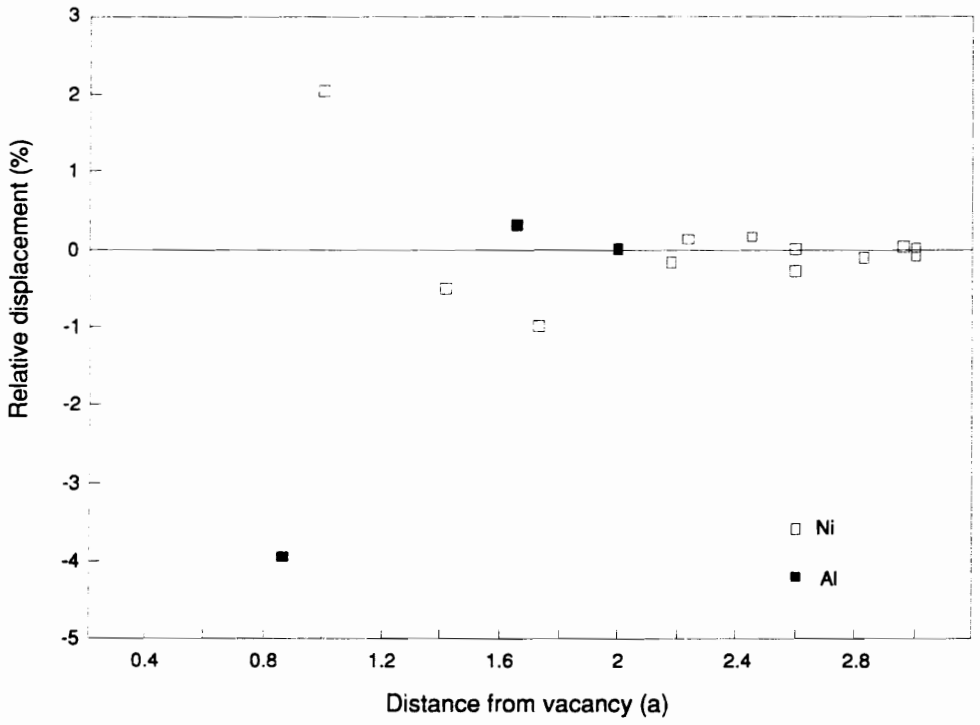
Relative displacement (%)
3
2
1
0
-1
-2
-3
-4
-5
0.4
0.8
1.2
1.6
2
2.4
2.8
Distance from vacancy (a)
Ni
Al

Figure 6.2(c)

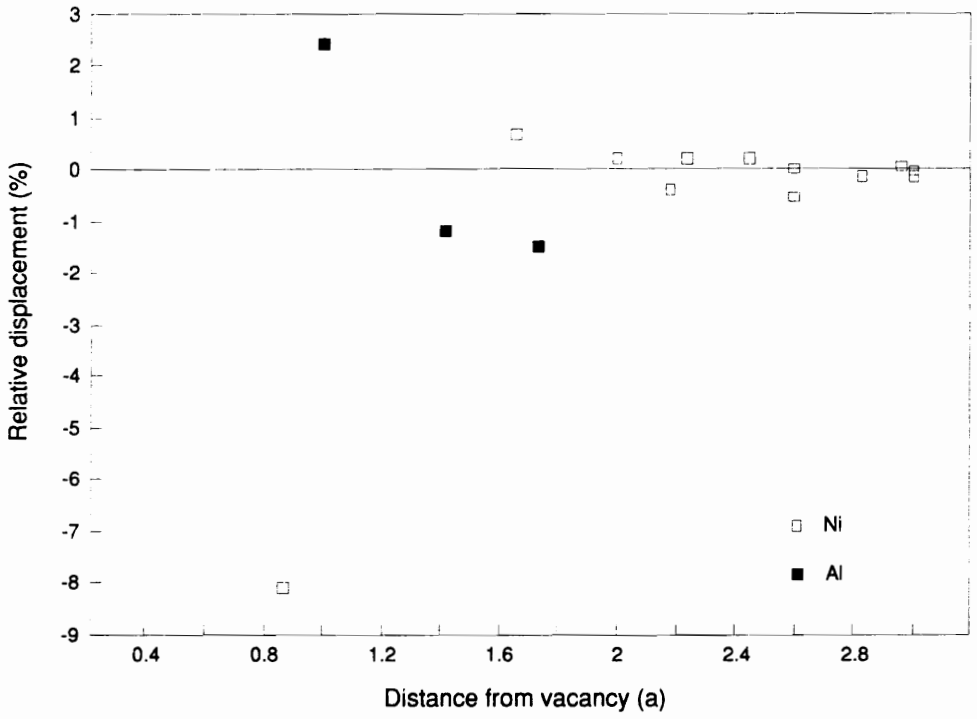

(d)

Figure 6.2: Relaxation around vacancies in Ni_3Al and NiAl. (a) Ni vacancy, (b) Al vacancy in Ni_3Al ; (c) Ni vacancy, (d) Al vacancy in NiAl. The atom types are only indicated for the atoms with an appreciable displacement.

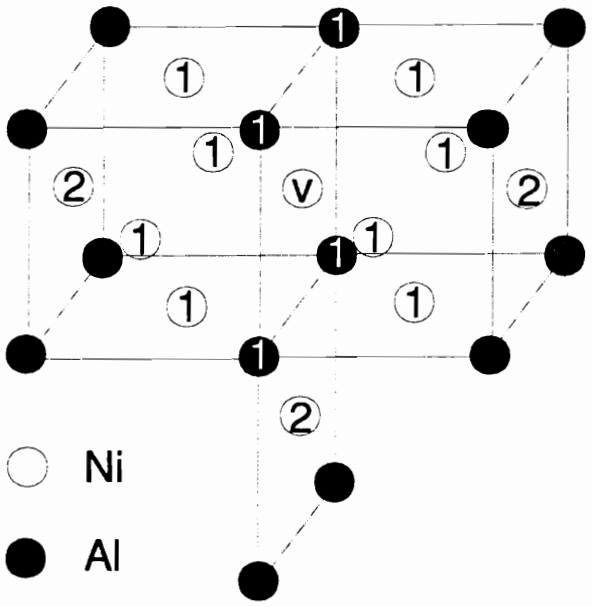

Figure 6.3: Different types of first and second neighbors for the Ni vacancy in Ni_3Al . v – Vacancy, 1 – the first nearest neighbor of the vacancy, 2 – the second nearest neighbor.

relatively simple as shown in Figure 6.2(b).

From these results it can be seen that the average inward displacement of the first shell is larger for the Al vacancy than for the Ni vacancy. A similar effect was also found in the relaxation behavior in surface defects [63, 64], where the missing bonds with Al atoms always produced the largest relaxations.

6.1.3 Vacancies in NiAl

The energies of vacancies in NiAl were not used in the procedure for the development of the interatomic potentials. The values obtained are 1.03 eV for the Al vacancy and 1.20 eV for the Ni vacancy. The formation energy of the Ni vacancy can be estimated from the experimental concentrations of Ni vacancies compiled recently by Kim [65]. If the experimental concentrations are analyzed with a simple $e^{\Delta H_{vac}/kT}$ rule the formation energy for the Ni vacancy results in 0.57 eV. If these values are analyzed with the more complex theory suggested by Kim [65] the formation energy ΔH_{vac} results in 2.16 eV, based on the best fit values for the pair interaction energies. The formation energy obtained here form the interatomic potentials is intermediate between these two estimates.

NiAl has a B2 structure, which can be considered as consisting of two simple cubic sublattices. The relaxation patterns (Figure 6.2(c) and (d)) are less complicated than the ones of Ni_3Al . Again the Al vacancy produces the larger inward displacements for the first shell than the Ni vacancy.

The energetics and relaxation around simple point defects in the two compounds NiAl and Ni_3Al were calculated using atomistic computer simulation. A difference between the present simulation and the calculations of elasticity[60] and the ones using certain types of pair potentials[59], such as Morse potentials, is that the relaxation shows oscillatory behavior instead of every symmetric shell relaxing inward[59]. In the perfect lattice, symmetry imposes the cancellation of forces for a finite range interatomic potential. When a vacancy is present, the first nearest neighbor atoms lack some interactions with the missing atom at the vacant site. This determines a net force on the atoms due to the no-cancellation of the pairwise term. Also, there is a change in the local electron density, which occurs within a very small area around the

Table 6.3: Relative displacement ($\frac{\Delta d}{d_p}$, %) around mono-vacancies and antisite defects in NiAl

Type	1st shell	2nd	3rd	4th	5th
Ni in NiAl	-3.94(Al)	2.04(Ni)	-0.51(Ni)	0.32(Al)	-0.99(Ni)
Al in NiAl	-8.09(Ni)	2.41(Al)	-1.21(Al)	0.67(Ni)	-1.50(Al)
Ni substitute Al	-1.40(Ni)	-0.52(Al)	-0.24(Al)	0.09(Ni)	-0.34(Al)
Al substitute Ni	3.38(Al)	-0.84(Ni)	0.56(Ni)	-0.01(Al)	0.85(Ni)

vacancy. This in turn determines the existence of an additional force, the atom arising from the unbalanced many body interaction. The second nearest neighbors are still subject to a force because they interact with the nearest neighbor atoms. It is the combination of pair and local volume forces that determines the general distortion pattern around the vacancy. These results are analogous to the case of surface relaxation [63]. In comparison with the free surface the change of the local electron density for the case of a vacancy is relatively small. Therefore, the oscillatory behavior of surface relaxation extends longer range than that for the vacancy case. For example, the displacements were shown to oscillate significantly up to 10 interatomic planes from the Ni(110) surface [64]. For mono-vacancy, the appreciable oscillatory displacement is only limited to the second nearest neighbor shell (Fig. 6.1 and Fig. 6.2). Even though the oscillatory displacements around defects are consistently found with EAM potentials, we note that the oscillatory displacements for a mono-vacancy were also obtained using a Lennard-Jones potential [60], which belongs to the van der Waals interaction type of inverse power dependence and accounts for the long range attractive part of interatomic potential better than an exponential Morse potential[14]. In general, the extent of the relaxation around the vacancies is of the order of a few percent and the vacancies at the Al sublattice always produce larger distortion in the lattices.

6.1.4 Antisite Defects in Ni_3Al and NiAl

The energy of antisite defects in Ni_3Al was calculated to be -0.14 eV for the substitution of Ni for Al and 0.46 eV for the substitution of Al for Ni in Ni_3Al (Table 6.1). The substitution of Al for Ni results in an increase in energy, while the substitution of Ni for Al is energetically more favorable. For NiAl, antisite energy is -0.60 eV for Ni replacing Al and 1.98 eV for Al replacing Ni. Such a great value (1.98 eV) makes it very unlikely for extra Al atom to occupy the Ni sublattices without the other compensational actions in NiAl. The relaxations around the antisite defects are shown in Fig. 6.4.

The substitution of Al in Ni sites involves the creation of more the nearest neighbor Al-Al bonds resulting in an energy increase. However, the substitution of Ni for Al is favored. This implies that ordered Ni_3Al and NiAl accommodate extra Ni in the Al sublattice more easily

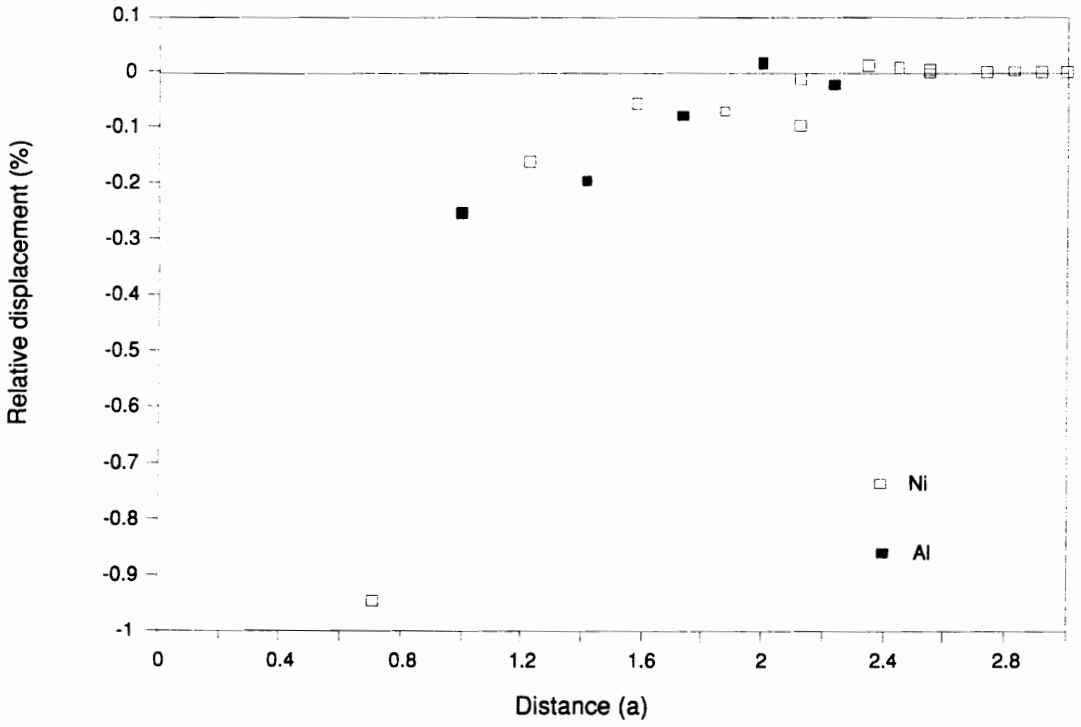
0.1
0
-0.1
-0.2
-0.3
-0.4
-0.5
-0.6
-0.7
-0.8
-0.9
-1
Relative displacement (%)
0
0.4
0.8
1.2
1.6
2
2.4
2.8
Distance (a)
Ni
Al

Figure 6.4(a)

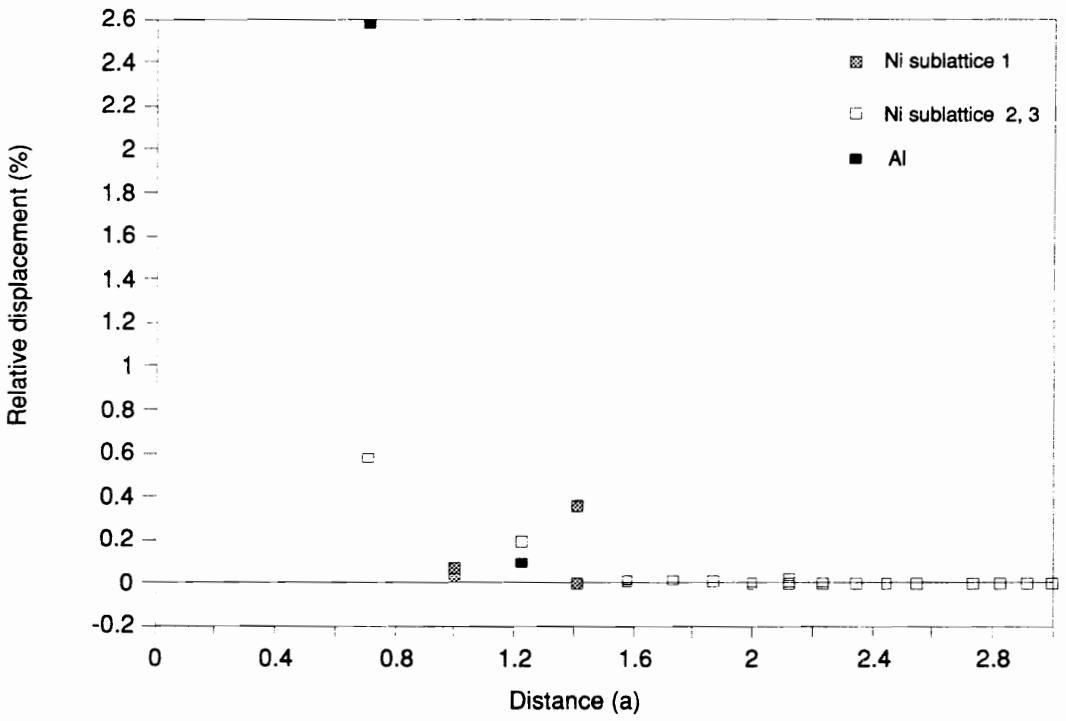
Relative displacement (%)
2.6
2.4
2.2
2
1.8
1.6
1.4
1.2
1
0.8
0.6
0.4
0.2
0
-0.2
0
0.4
0.8
1.2
1.6
2
2.4
2.8
Distance (a)
Ni sublattice 1
Ni sublattice 2, 3
Al

Figure 6.4(b)

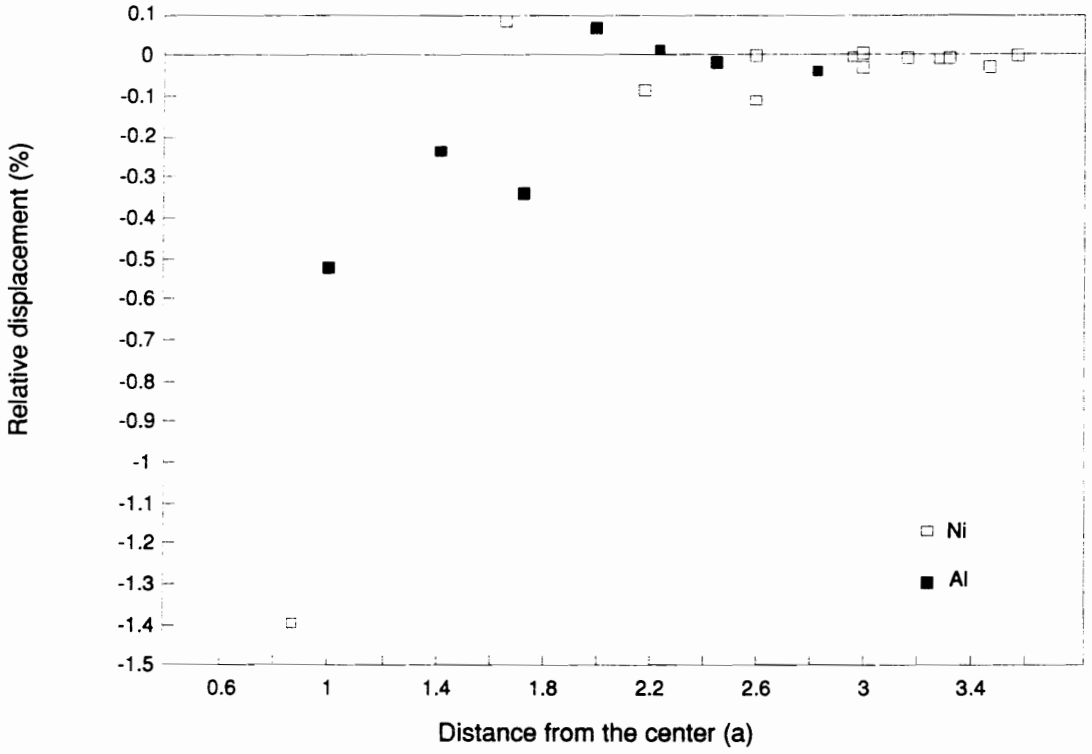
Relative displacement (%)
0.1
0
-0.1
-0.2
-0.3
-0.4
-0.5
-0.6
-0.7
-0.8
-0.9
-1
-1.1
-1.2
-1.3
-1.4
-1.5
0.6
1
1.4
1.8
2.2
2.6
3
3.4
Distance from the center (a)
Ni
Al

Figure 6.4(c)

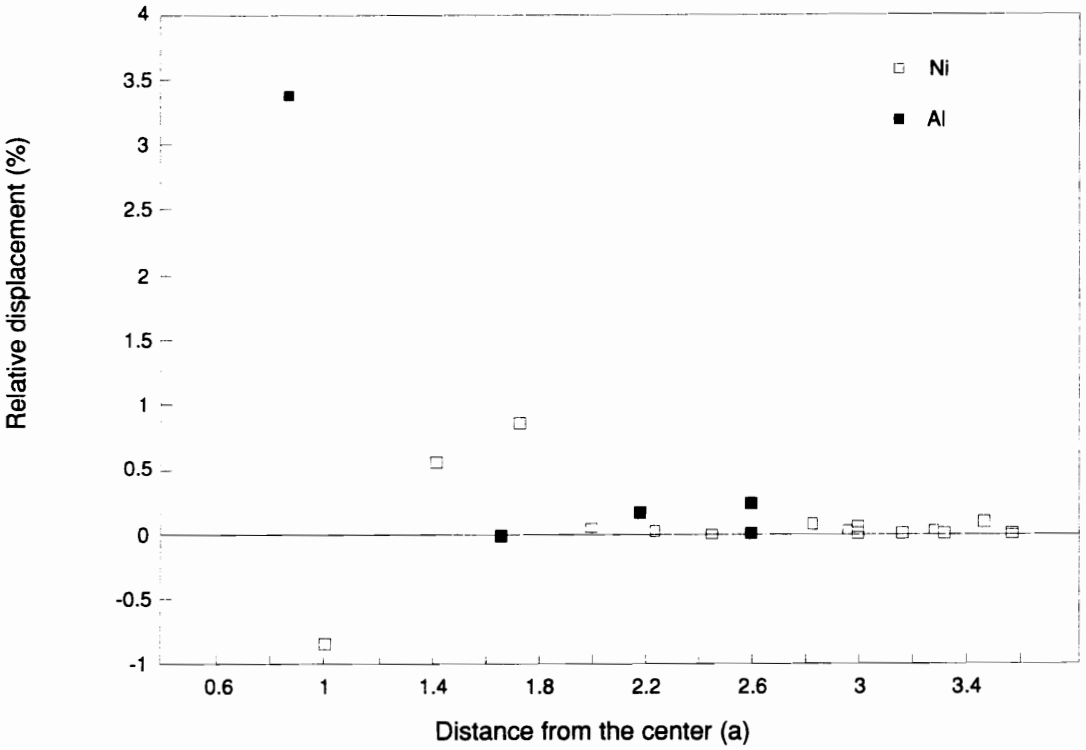

(d)

Figure 6.4: Relaxation around antisite defects in Ni_3Al and NiAl. (a) Ni replaces Al, (b) Al replaces Ni in Ni_3Al ; (c) Ni replaces Al, (d) Al replaces Ni in NiAl. The atom types are only indicated for the atoms with an appreciable displacement.

than it accommodates extra Al in the Ni sublattice. For the latter case in NiAl, it is reported that the excess Al atoms generally fill normal Al sites and the predominant point defects are vacant Ni sites[66]. In this respect, it is interesting to note that the structure of the compound Ni_2Al_3 can be described as a basic B2 structure by removing one Ni atom for every three unit cells in the NiAl structure, which can be easily seen in the (110) projection of both phases[67]. In other words, the local accumulation of vacancies may play a part in the phase transformation of NiAl to Ni_2Al_3.

6.1.5 Effects of Randomly Located Disorder

We computed the effects of a random number of antisite pairs introduced in the lattice on the equilibrium lattice parameter. The antisite pairs were introduced using a random number generator routine in order to simulate the effects of having a long range order (LRO) parameter different from 1. For each given concentration of random antisites, the value of the lattice parameter corresponding to the minimum energy of the total block was calculated.

Fig. 6.5 shows the lattice parameter as a function of the LRO parameter for both NiAl and Ni_3Al . The definition of the order parameter used in these figures is as follows:

$$\eta = \frac{f_{A\alpha} - \gamma_A}{1 - \gamma_A} \tag{6.1}$$

where $f_{A\alpha}$ is the fraction of sites of α sublattice occupied by A atoms, and γ_A is the fraction of A atoms in the crystal. In a stoichiometric crystal, γ_A is 1/4 in Ni_3Al and 1/2 in NiAl, with A being aluminium.

These results can be compared with experimental determinations of the order parameter increase that are available for Ni_3Al [68]. Experimental evidence of total disorder was found in alloys with approximately 0.4% increase in the lattice parameter, in agreement with the present calculations [68]. The present calculations for Ni_3Al are not in agreement with the results derived in terms of the bond lengths d [68]:

$$a_\eta = 1/8(3+\eta)d_{Ni-Al} + 1/16[(9-\eta)d_{Ni-Ni} + (1-\eta)d_{Al-Al}] \tag{6.2}$$

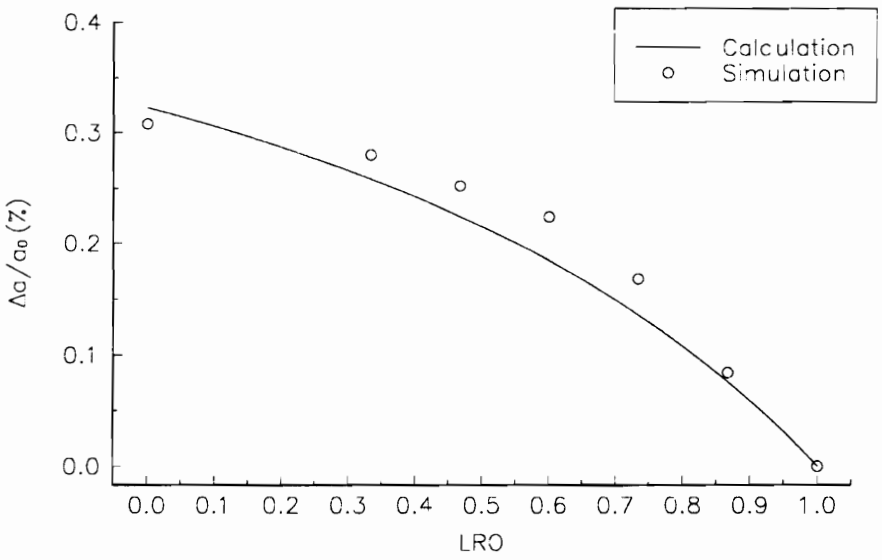
Calculation
Simulation
0.4
0.3
0.2
0.1
0.0
Δa/a₀ (%)
0.0 0.1 0.2 0.3 0.4 0.5 0.6 0.7 0.8 0.9 1.0
LRO

Figure 6.5(a)

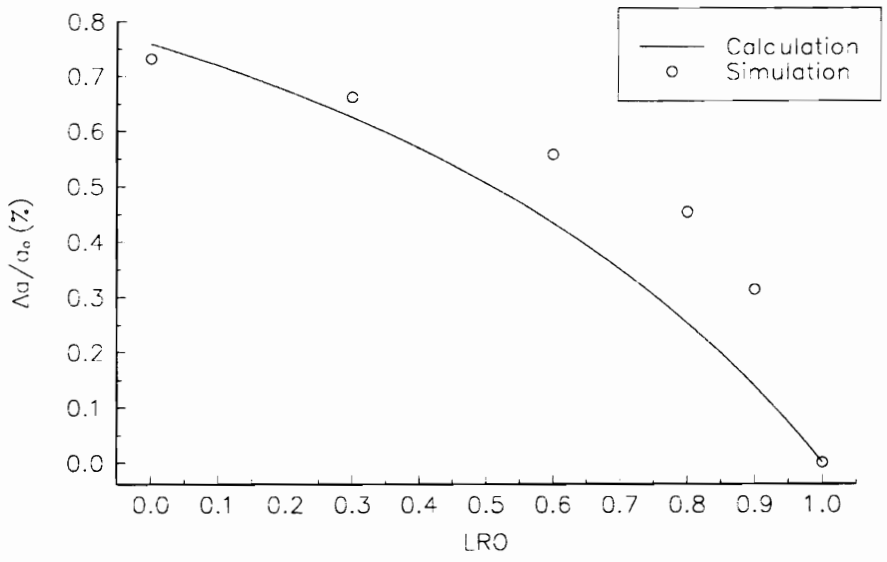

(b)

Figure 6.5: Equilibrium lattice parameter as a function of the long range order parameter, (a) Ni_3Al , (b) NiAl.

using d values of 3.52, 4.05 and 3.63 for Ni-Ni, Al-Al and Ni-Al respectively. The results are correct for the complete ordered alloy but the functional form and the amount of the lattice expansion upon disordering are very different from those obtained in the simulations.

The simulation results can be better interpreted in terms of the observed relaxation for the antisite causing the largest distortion. This is the Al substituting in the Ni sublattice. If we assume that each pair of antisite defects generates this distortion, the lattice parameter can be approximated as follows:

$$a_\eta = a_0(1 + \alpha \times c) \tag{6.3}$$

where α is the first shell expansion caused by Al placed in the Ni sublattice, 2.58% for Ni_3Al (Table 6.2), 3.38% for NiAl (Table 6.3), and c denotes the concentration of the antisite pairs. The order parameter can be given in terms of the concentration c as:

$$\eta = \frac{1 - 8c}{1 - 4c} \tag{6.4}$$

$$\eta = \frac{1 - 4c}{1 - 2c} \tag{6.5}$$

for Ni_3Al and NiAl respectively.

Figure 6.5 shows the calculated results of this simple model, in good agreement with the simulations for both systems.

The changes in the lattice parameter with increasing disorder obviously do not follow the calculation[68] which is actually on the basis of Vegard's law. In fact, the nearest neighbor distances in the two compounds considered here are about the same as those in pure Ni. It was found that the basic contribution to the disordering energy in these compounds is that of the location of Al atoms in Ni sites. The maximum increase of the lattice parameter with the LRO parameter is 0.31% for Ni_3Al and 0.73% for NiAl at complete disorder. Such small changes are not expected to promote lattice destabilization [69]. The results can be rationalized in terms of the important effect of the larger size of the Al atom. For $\eta = 0$, the fraction of Al-Al bonds is 6% in Ni_3Al and 25% in NiAl, therefore larger lattice dilation is found in NiAl upon disordering. The larger size of the Al atom has also been observed to dictate the relaxation structure of the antiphase boundary (APB) in this system, where the largest relaxation

Table 6.4: Di-vacancy formation energy E^f_{2v} (ev) in Ni_3Al

Type	Distance	E^f_{2v}	ϵ
Ni(000)-Ni($\frac{1}{2}0\frac{1}{2}$)	$\frac{\sqrt{2}}{2}a$	3.011	-0.207
-Ni(100)	a	3.170	-0.048
-Ni(010)		3.176	-0.042
-Ni(101)	$\sqrt{2}a$	3.215	0.003
-Ni(011)		3.234	-0.016
-Ni($\frac{3}{2}0\frac{1}{2}$)	$\frac{\sqrt{10}}{2}a$	3.199	-0.019
-Ni($\frac{1}{2}0\frac{3}{2}$)		3.212	-0.006
-Ni(111)	$\sqrt{3}a$	3.207	-0.011
Al(000)-Ni($\frac{1}{2}0\frac{1}{2}$)	$\frac{\sqrt{2}}{2}a$	3.237	-0.151
-Ni($1\frac{1}{2}\frac{1}{2}$)	$\frac{\sqrt{6}}{2}a$	3.335	-0.053
-Ni($0\frac{3}{2}\frac{1}{2}$)	$\frac{\sqrt{10}}{2}a$	3.373	-0.015
Al(000)-Al(100)	a	3.506	-0.052
-Al(101)	$\sqrt{2}a$	3.556	-0.002
-Al(111)	$\sqrt{3}a$	3.541	-0.017

Table 6.5: Relative displacement around di-vacancies in Ni_3Al

Type	d_p, Å	$\frac{\Delta d}{d_p}$, %
Ni(000)-	2.188 (1st shell)	-1.03(Ni)
Ni($\frac{1}{2}0\frac{1}{2}$)		-5.54(Al)
	2.825 (2nd)	0.64(Ni)
		0.53(Ni)
	3.342 (3rd)	-1.28(Al)
Al(000)-	2.188 (1st shell)	-3.71(Ni)
Ni($\frac{1}{2}0\frac{1}{2}$)	2.825 (2nd)	-0.76(Ni)
		-1.46(Al)
	3.342 (3rd)	-1.20(Ni)
		-0.01(Ni)
Al(000)-	1.787 (1st shell)	-2.92(Ni)
Al(100)	3.094 (2nd)	-1.60(Ni)
	3.994 (3rd)	-1.04(Ni)
		-0.25(Ni)
		-0.22(Al)

Table 6.6: Relative displacement around di-vacancies in NiAl

Type	d_p, Å	$\frac{\Delta d}{d_p}$, %
Ni(000)-	2.030(1st shell)	-6.16(Al)
Ni(100)	3.210(2nd)	1.18(Ni)
	3.516(3rd)	-2.61(Al)
	4.305(4th)	1.41(Ni)
		-1.29(Ni)
Al(000)-	0.829(1st shell)	-4.46(Al)
Ni($\frac{1}{2}\frac{1}{2}\frac{1}{2}$)		-2.31(Ni)
	1.090(2nd)	-5.54(Ni)
		-3.04(Al)
	1.299(3rd)	-5.42(Ni)
		-2.54(Al)
		1.85(Al)
		1.73(Ni)
Al(000)-	2.030(1st shell)	-12.82(Ni)
Al(100)	3.210(2nd)	0.30(Al)
	3.516(3rd)	-4.89(Al)
	4.306(4th)	1.62(Al)
		-2.39(Al)

Table 6.7: Di-vacancy formation energy E_{2v}^{f} (ev) in NiAl

Type	Distance	E_{2v}^{f}	ϵ
Ni(000)-Ni(100)	a	2.356	-0.114
-Ni(110)	$\sqrt{2}a$	2.568	0.098
-Ni(200)	$2a$	2.451	-0.019
-Ni(210)	$\sqrt{5}a$	2.437	-0.033
Al(000)-Ni($\frac{1}{2}\frac{1}{2}\frac{1}{2}$)	$\frac{\sqrt{3}}{2}a$	2.377	0.016
-Ni($\frac{1}{2}\frac{1}{2}\frac{3}{2}$)	$\frac{\sqrt{11}}{2}a$	2.293	-0.068
-Ni($\frac{3}{2}\frac{3}{2}\frac{1}{2}$)	$\frac{\sqrt{19}}{2}a$	2.358	-0.003
Al(000)-Al(100)	a	2.116	-0.135
-Al(110)	$\sqrt{2}a$	2.317	0.065
-Al(200)	$2a$	2.143	-0.109
-Ni(210)	$\sqrt{5}a$	2.135	-0.117

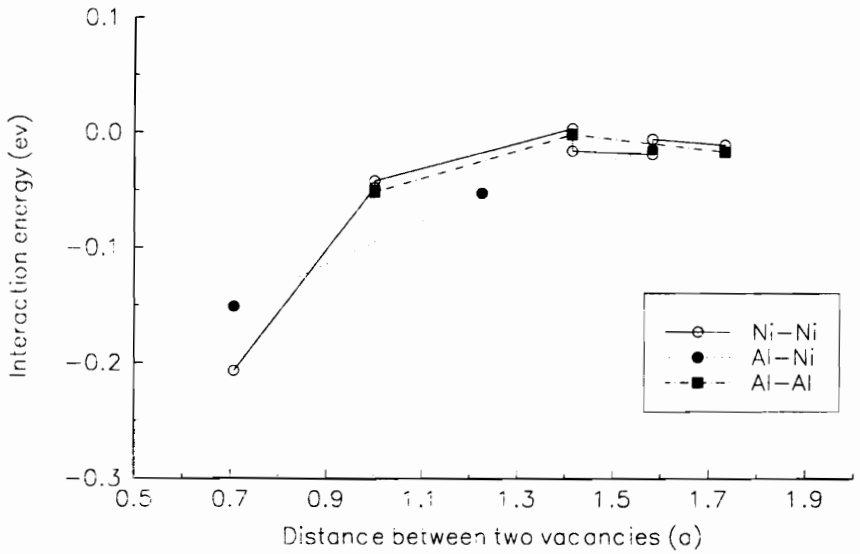

Figure 6.6: Interaction energy of two vacancies as a function of the distance between the vacancies in Ni_3Al .

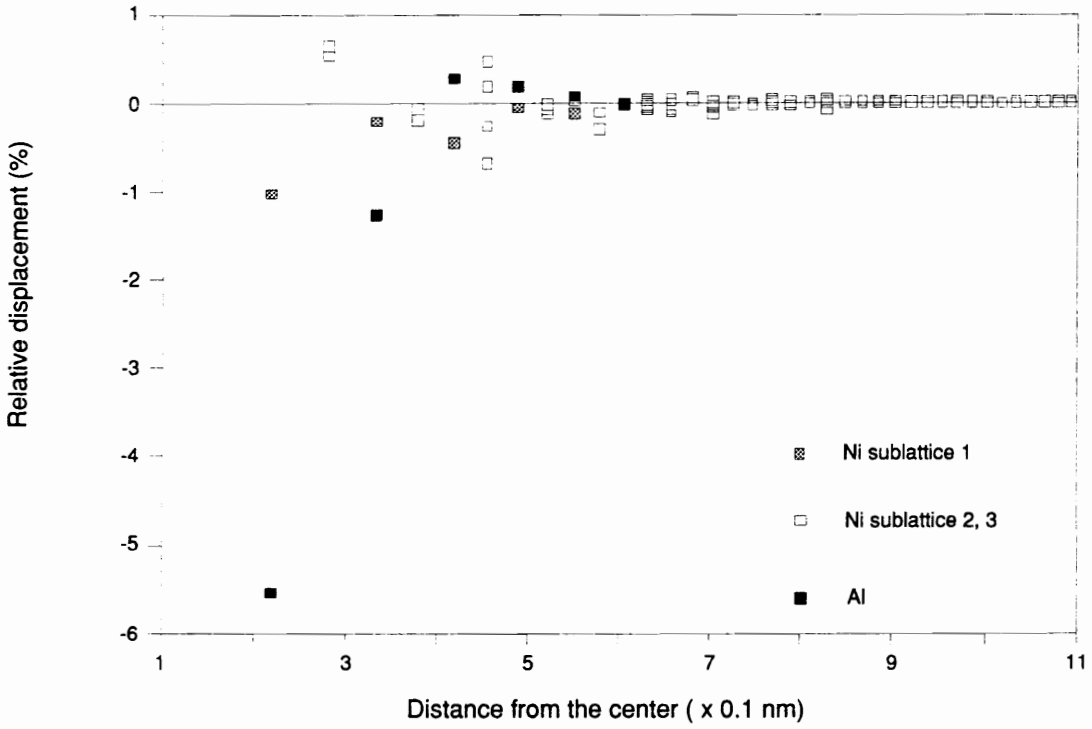
Relative displacement (%)
1
0
-1
-2
-3
-4
-5
-6
1
3
5
7
9
11
Distance from the center (x 0.1 nm)
Ni sublattice 1
Ni sublattice 2, 3
Al

Figure 6.7(a)

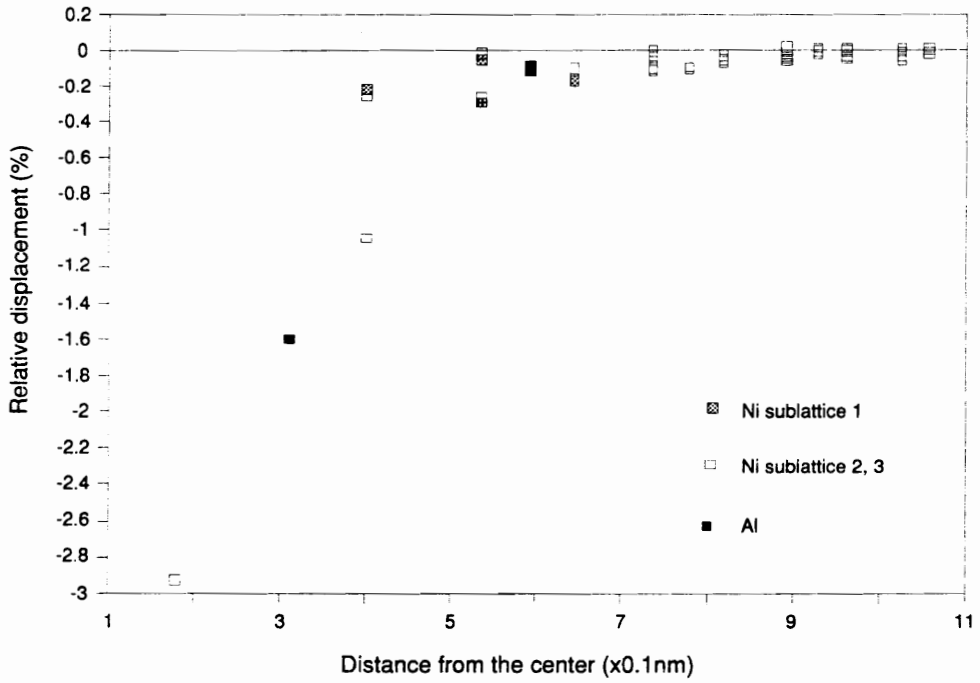
0.2
0
-0.2
-0.4
-0.6
-0.8
-1
-1.2
-1.4
-1.6
-1.8
-2
-2.2
-2.4
-2.6
-2.8
-3
Relative displacement (%)
1
3
5
7
9
11
Distance from the center (x0.1nm)
Ni sublattice 1
Ni sublattice 2, 3
Al

Figure 6.7(b)

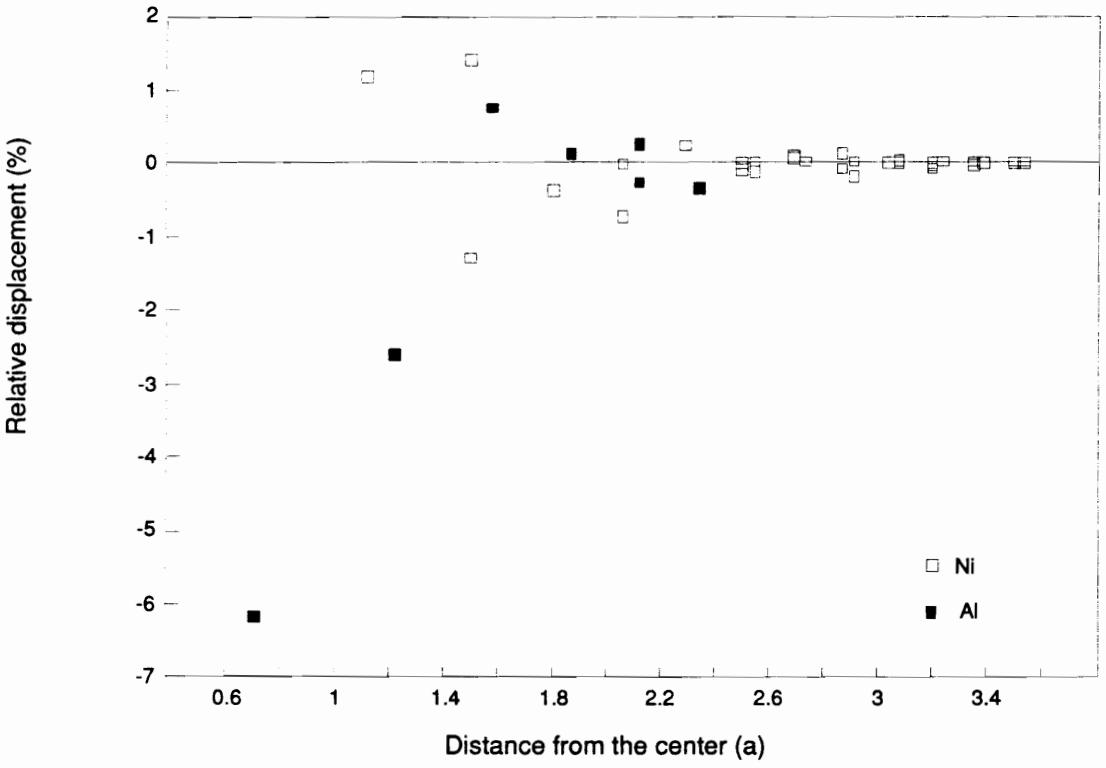
Relative displacement (%)
2
1
0
-1
-2
-3
-4
-5
-6
-7
0.6
1
1.4
1.8
2.2
2.6
3
3.4
Distance from the center (a)
Ni
Al

Figure 6.7(c)

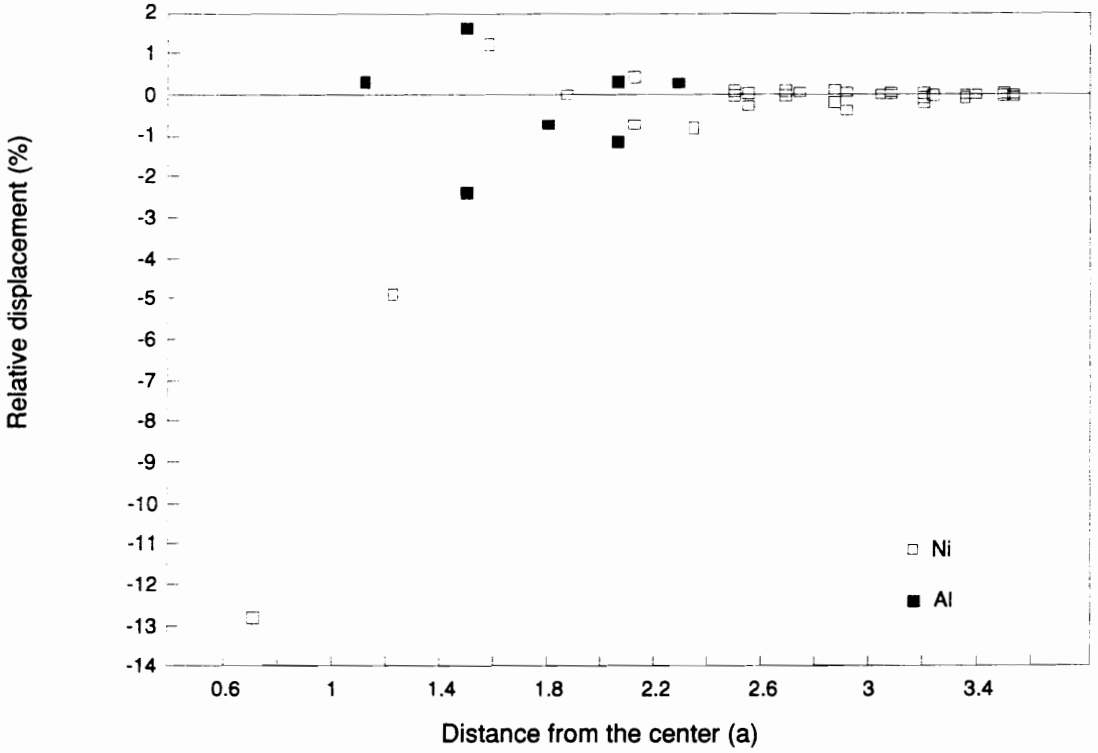

(d)

Figure 6.7: Displacements around the center of di-vacancies as a function of the distance from the defect center, (a) Ni-Ni, (b) Al-Al in Ni_3Al ; (c) Ni-Ni, (d) Al-Al in NiAl. The atom types are only indicated for the atoms with an appreciable displacement.

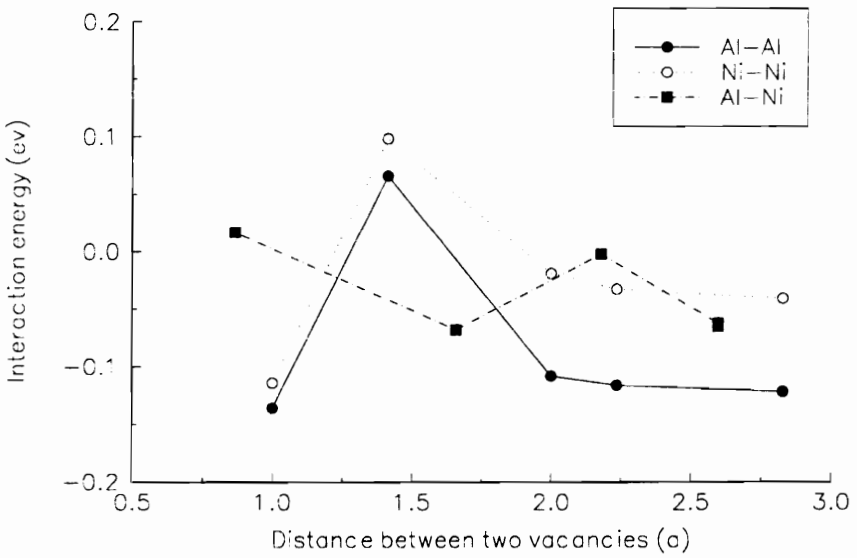

Figure 6.8: Interaction energy of two vacancies as a function of the distance between the vacancies in NiAl.

displacements are those of the nearest neighbor Al-Al bonds created in the APB region [70].

6.1.6 Defect Interaction

Table 6.4 shows the formation energies for various divacancies in Ni_3Al . The most stable divacancy is the one in which two vacancies are at the first neighboring Ni sublattices. Two vacancies show an attractive interaction, which decays rapidly with increasing the distance between vacancies, as shown in Fig. 6.6. Figure 6.7 shows these relaxation displacements as a function of the distance to the center of the di-vacancy for some of the cases studied. The actual values for the atoms in the shells nearest the di-vacancy center are shown in Table 6.5 for Ni_3Al and in Table 6.6 for NiAl. These results can be understood if the local chemical environment of the atoms in different shells around the center of the di-vacancy is considered.

Table 6.7 shows the formation energies observed for various divacancies in NiAl. Although the relaxation pattern around the di-vacancy in NiAl is quite similar, the interaction between vacancies behaves very differently. Instead of a general tendency of attraction, some cases show a repulsive interaction, as seen in Fig. 6.8, even in the first neighboring Al-Al vacancies. This repulsive behavior is also obtained by the first principle calculations [71] for NiAl. The interaction behaviors of vacancies in Ni_3Al and NiAl are quite different. In contrast to the general attraction in Ni_3Al (Fig. 6.6), some two vacancies in NiAl show a repulsive interaction (Fig. 6.8). The most stable divacancy in NiAl is that two vacancies sit in the Al sublattice as the second nearest neighbors, therefore, the probability of recombination of the vacancies is very small at zero temperature in this highly symmetrical structure. This accounts for the existence of the structural vacancies (in opposition to thermal vacancies caused by temperature). In fact, vacancies are always present in ordered B2 TAl compounds (T = Ni, Fe, Co), even at exact stoichiometry[72].

6.1.7 Concluding Remarks

Atomistic computer simulation with embedded atom method potentials has been performed to study the energetics and structures of point defects in $L1_2$ Ni_3Al and B2 NiAl. The large size of Al atom plays a dominant role in the relaxed atomic configurations in the system. In both,

Ni_3Al and NiAl it was found that excess Ni can be accommodated by Ni in Al sites, whereas such an accommodation of excess Al by Al in Ni sites is not energetically favorable.

The most stable divacancy is that two vacancies are the first nearest neighbors at Ni sublattices for Ni_3Al and the second nearest neighbors at Al sublattices for NiAl. The effects of different degrees of random disorder on the lattice parameters were evaluated.

The interaction behavior of vacancies in Ni_3Al and NiAl is quite different. In contrast to the general attraction in Ni_3Al (Fig. 6.6), some two vacancies in NiAl show a repulsive interaction (Fig. 6.8). The most stable divacancy in NiAl is that two vacancies sit in the Al sublattice as the second nearest neighbors. The probability of recombination of the vacancies is very small at zero temperature in this highly symmetrical structure. This is consistent with the existence of the structural vacancies.

6.2 Effects of Local Disorder on Core Structures †

6.2.1 Slip and Ductility

A great deal research effort has been devoted in recent years to the study of possible methods to improve ductility in ordered NiAl. These methods include second phase formation[73] and utilizing the role of surface and interface dislocations [46]. One primary reason for the poor ductility of NiAl is believed to be the lack of sufficient slip systems which is a consequence of the fact that NiAl deforms through ⟨100⟩ slip. Other compounds, such as CuZn with the same B2 structure that deform through ⟨111⟩ slip do exhibit ductile behavior. It follows that in order to improve ductility one might investigate the possibilities of stabilizing ⟨111⟩ slip in this material.

It has been shown that when the crystal orientation is such that the applied stress on the existing ⟨100⟩dislocations is zero, the material indeed deforms through ⟨111⟩slip [42]. As a matter of fact, the occurrence of ⟨111⟩slip has also been proposed as an explanation for the limited ductility of NiAl observed at room temperature [74]. The instability of ⟨111⟩slip is certainly connected to the fact that the ordering energy is high as well as the fact that the ⟨111⟩dislocations apparently do not split into partials (Chapter 5).

In agreement with experimental observations, computer simulation also shows that the stable form for screw ⟨111⟩ dislocations is for these dislocations to remain complete. In more ductile B2 materials the stable form is that of two superpartials of 1/2⟨111⟩Burguers vector

†Based on "Possibilities of Slip Modification in B2 NiAl", by D. Farkas and Z. Xie, in *High-Temperature Ordered Intermetallic Alloys V*, Eds: I. Baker *et al.*, Proc. Mater. Res. Soc. Symp. vol. 288, 1992, pp.435-441

with an APB in between. The energetics and stability of the dissociated structure is largely influenced by the value of the APB energy. As mentioned in Chapter 4, γ surfaces in different planes including (110) and (112) with particular interest in the vicinity of the APB, show that the minimum in the APB region is deviated from the $1/2\langle 111\rangle$ position in both (110) and (112) planes. For the $\{110\}\gamma$ surface the $1/2\langle 111\rangle$ fault is an unstable maximum. Two minima occur on both sides of the $1/2a[1\bar{1}1]$ fault, deviated in the $[1\bar{1}0]$ direction. The γ surface in the (112) plane shows that the minimum corresponding to the APB is shifted in the $[\bar{1}\bar{1}1]$ direction from the perfect $1/2a[\bar{1}\bar{1}1]$ position. Chapter 5 presented the study of metastable dissociations of the complete $\langle 111\rangle$ dislocation into $1/2\langle 111\rangle$ partials and the alternative splitting suggested by the γ surface calculations having a stable fault between the two partials. Even using this alternative splitting, the complete $\langle 111\rangle$dislocation was still stable with respect to the dissociation into partials.

In this section, we will analyze the possibilities of stabilizing $\langle 111\rangle$ slip in NiAl based on the atomistic structure of dislocation cores. The dislocation core structures as affected by the interaction with point defects in the center of the core region will be demonstrated.

6.2.2 $\langle 100\rangle$ Dislocation

The core structures of $\langle 100\rangle$ and $\langle 111\rangle$ dislocations as affected by the interaction with various point defects present in the material were simulated. The point defects considered are, in the first place, those that result from stoichiometry deviations. These are vacancies in Ni sites, vacancies in Al sites, extra Ni in Al sites, and extra Al in Ni sites. We also considered the effect of disorder, which will occur increasingly with temperature. Disorder is represented by a pair of antisite defects (a sublattice exchange).

Due to the periodic boundary conditions used in the simulations along the dislocation line, the point defects were added as a row of defects parallel to the dislocation line. As discussed in the previous section, the interaction of point defects is in very short range. In order to avoid this interaction among the defects two unit cells in the direction of the dislocation line were employed. The point defects were located in the center of the dislocation core. The configuration included one unit cell containing a point defect and one without a point defect

in the periodic direction. In order to asses the extent of the influence that these point defects may have on the core structure of ⟨100⟩, ⟨110⟩, and ⟨111⟩ dislocations, the variations of the core structure of the dislocations considered in Chapter 4 and Chapter 5 with local disorder are examined. The effects of overall composition change on dislocation core structures will appear in the next section (Section 6.3).

Figure 6.9 shows the effect of the various point defects on the core structure of the edge ⟨100⟩dislocation. The calculation method and interatomic potentials used are the same as those used in the proceeding chapters. The core structures are represented using the invariants of the strain tensor, with perfect lattice points superposed. The most significant effects occur for the case of excess Al atoms. The effects are confined to the region of very high deformation level. This is probably due do the fact that the point defects were located in that region.

From these results, it is clear that the basic core structure remains largely unaffected. This is probably also due to the fact that the shape of the core is greatly influenced by elasticity itself and therefore the effect of point defects on core structure are of lesser importance. Same procedure of introducing local point defects was also applied to all the ⟨100⟩ and ⟨110⟩ dislocations considered in Chapter 4. Since core changes upon the introduction of local point defects are very similar, Figure 6.9 is shown here as a typical example.

6.2.3 ⟨111⟩ Dislocation

Figure 6.10 shows the effect of the various point defects on the core structure of the screw ⟨111⟩dislocation.

In this case the effects are more important than for the the case of ⟨100⟩ dislocations. In particular, the shape of the core changes. In ⟨100⟩ dislocations, the affected area is about one lattice parameter, which can not promote any true dissociation of the dislocation core, whereas for ⟨111⟩ dislocation the affected area is much larger. This is probably related to the fact that for ⟨111⟩fault vectors, the gamma surface calculation shows that faults in various planes containing the ⟨111⟩direction have very similar energies [49]. The shape of the dislocation core still remains highly non-planar and very difficult to move. No spontaneous splitting of this dislocation occurred in the simulations.

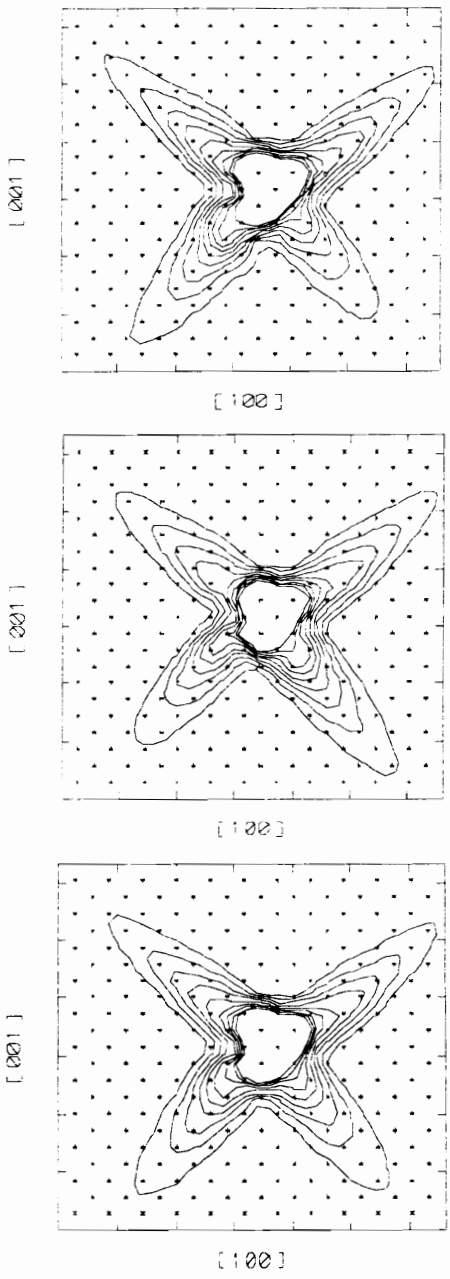

Figure 6.9(a)

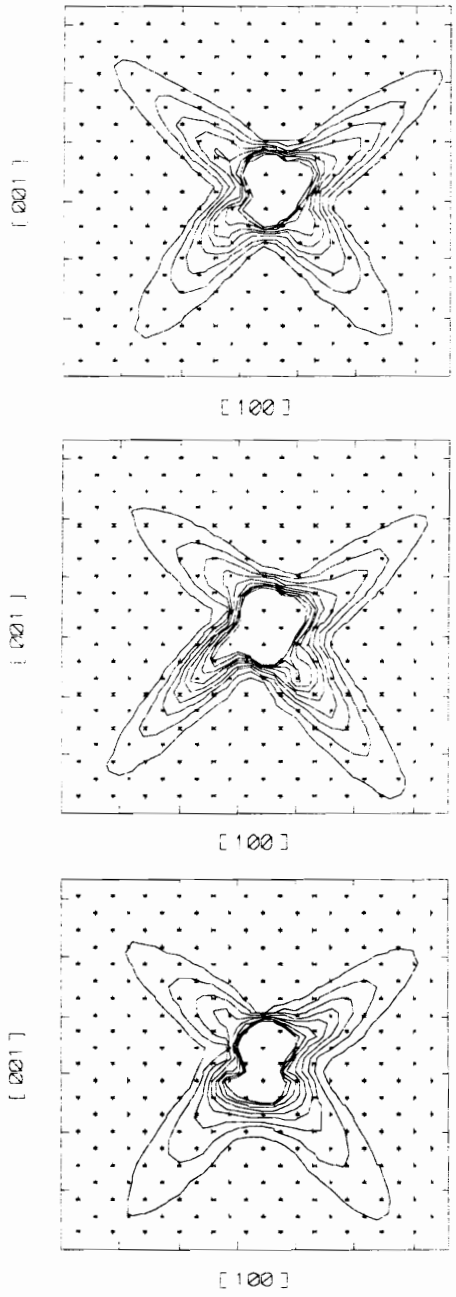

(b)

Figure 6.9: Core structure of a pure edge [100] dislocation along [001] with point defects. From top to bottom, (a) without disorder, with a row of Al vacancies, with a row of Ni vacancies; (b) with a row of extra Al, core with a row of extra Ni, with a row of interchange between Ni and Al.

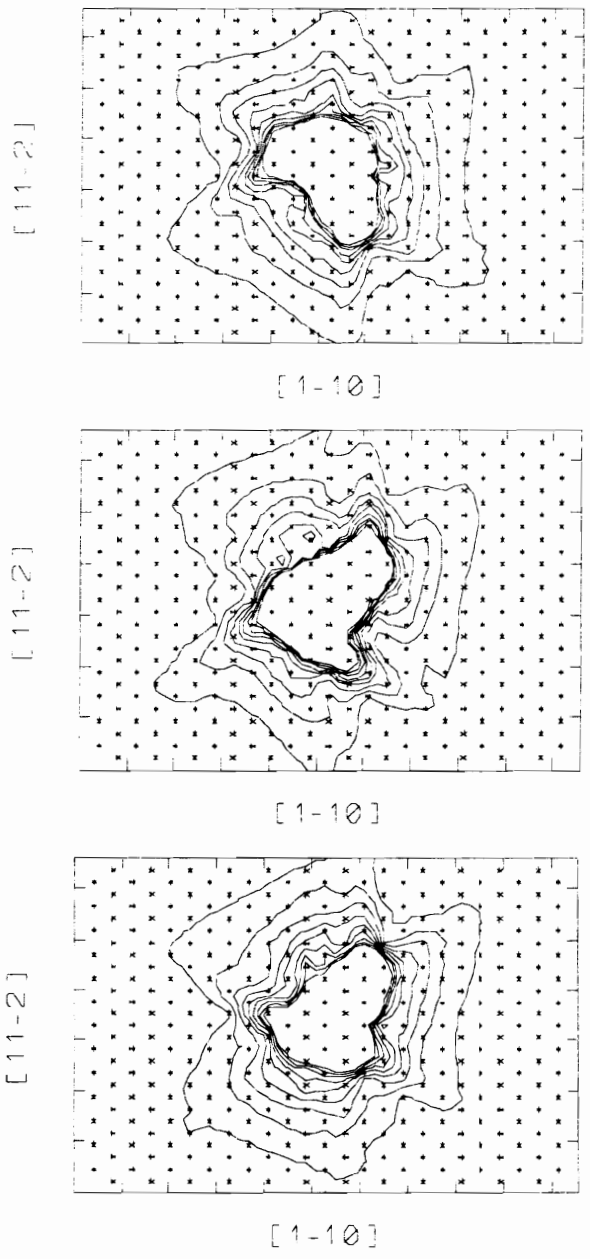

Figure 6.10(a)

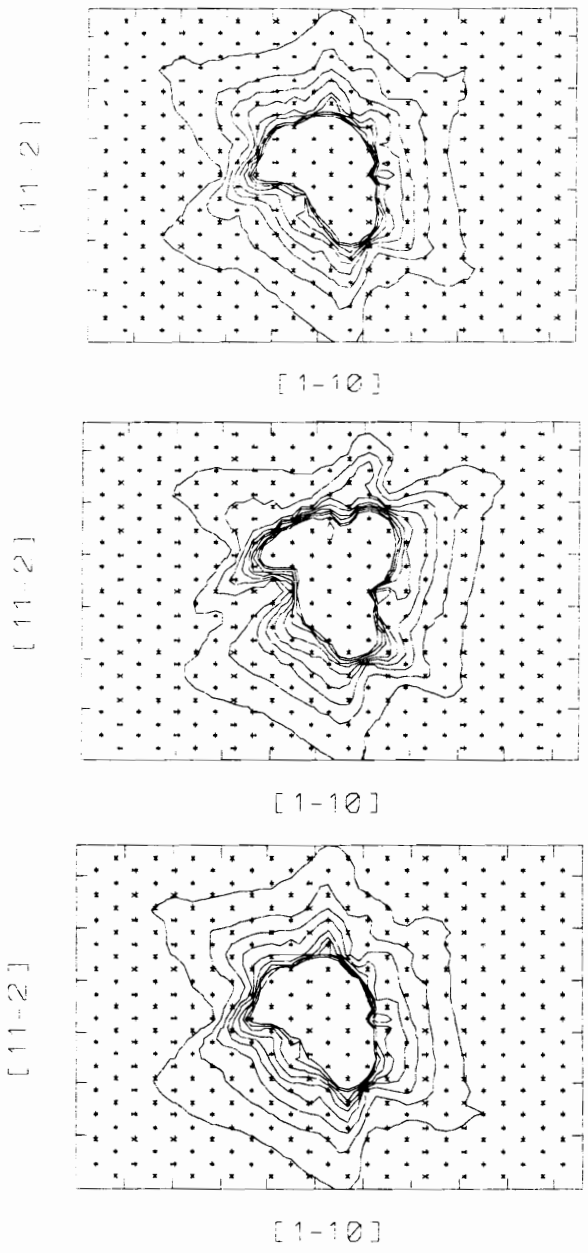

(b)

Figure 6.10: Core structure of a pure screw [111] dislocation along [111] with point defects. From top to bottom, (a) without disorder, with a row of Al vacancies, with a row of Ni vacancies; (b) with a row of extra Al, core with a row of extra Ni, with a row of interchange between Ni and Al.

Figure 6.10 also includes the effects of Al located on Ni sublattices and of Al vacancies on the core structure of both dislocations. Although these point defects are higher energy defects, the results are very similar to those obtained for Ni in Al sites and Ni vacancies. The possibility of stabilizing ⟨111⟩slip in NiAl through core changes due to point defects is predicted to be slim on the basis of atomistic simulations of dislocation core structure. The effects of the point defects on the structures of the cores are very localized to the immediate vicinity of the point defect. In most cases these effects do not alter the basic shape and characteristic of the dislocation core. The observed effects may explain the very high rate of increase of the yield strain with stoichiometry deviations [74]. This rate was reported to be much higher than what could be explained on the basis of solution hardening theories. It seems possible that core effects contribute to the hardening process in off-stoichiometric alloys. In an experimental observation of dislocation cores of edge ⟨100⟩dislocations [75] the core was found to be more extended in the off-stoichiometric alloys than in the stoichiometric material. The basic structure of the core which is extended in two {110} type planes, remained the same and in agreement with the present simulations.

In analyzing several compounds with the B2 structure it is clear that ⟨100⟩ slip is preferred for compounds with higher values of the ordering energy whereas ⟨111⟩slip is preferred for compounds with relatively lower values of the ordering energy. In compounds with intermediate values of the ordering energy both slip systems are observed in different temperature regimes. This fact is probably related to the fact that the complete ⟨111⟩dislocation is very non-planar and difficult to move, as shown in our simulations. At lower values of the APB energy the dislocations split into partials that are easier to move and leave the APB in between. As indicated in Figure 5.9 in Chapter 5, the metastable core structures, 1/2 ⟨111⟩dislocations transformed to a more planar core structure under applied stress. It follows that in order to stabilize the ⟨111⟩slip system one probably needs to have the partials stable with respect to the complete ⟨111⟩dislocation. In the light of the present simulations, it is probably difficult to accomplish through stoichiometry deviation. This is in agreement with the known fact that the ⟨100⟩slip system is still stable for off-stoichiometric alloys. The details of the core structures of dislocations in off-stoichiometric NiAl will be given in Section 6.3.

The present results suggest that alloying is more likely to introduce qualitative changes in mechanical behavior through changes in the planar fault energies, (the APB in this case) than through local changes in core structure. Furthermore, the question always remains as to the possibility of the atmosphere of point defects following the dislocation line as it moves in the deformation process.

It seems that in order to stabilize $\langle 111 \rangle$slip it is necessary to decrease the value of the APB energy. This can be attempted through alloying with a third element that would substitute for Al. In our previous studies of planar faults in the Ni-Al system it was found that the primary relaxation observed in the APB is the movement from the Al-Al first neighbors created due to the fault away from each other. This suggests that there is a simple size effect in this system, with Al being larger than Ni. One possible suggestion for decreasing the APB energy would be alloying with a third element that would substitute for Al and be a smaller atom.

6.2.4 Concluding Remarks

The effects of various possible local disorder on core structure have been simulated. Significant contributions merely occur in the core range immediate vicinity of the point defect. It is unlikely that local disorder changes could be used to successfully stabilize $\langle 111 \rangle$ slip. As a consequence, alloying efforts should be directed towards changing the APB energy of the NiAl-based alloy to a lower value to stabilize $\langle 111 \rangle$ slip.

6.3 Dislocation Core Structures in Off-stoichiometric NiAl

6.3.1 Deviation from Stoichiometry

It is well established that deviations from stoichiometry lead to large increases in the strength of B2 NiAl alloys. This was first noted by Westbrook [76] as an increase in hardness of both Ni-rich and Al-rich NiAl relative to stoichiometric NiAl. The strengthening was attributed to defect hardening due to either substitutional or vacancy effects which increase with deviations from perfect stoichiometry. Following Westbrook's initial reports, Ball and Smallman [37] and Pascoe and Newey [77] found that deviations from stoichiometry dramatically increase the compressive yield strength of NiAl. Again, the strengthening was attributed to increases in point defect concentrations with non-stoichiometric Ni or Al additions. These studies led Hahn and Vedula [57] to examine the tensile behavior of NiAl as a function of stoichiometry. The result was that limited tensile ductility (approximately 2%) could be achieved in essentially stoichiometric NiAl (50.3$\pm$0.2 at%) while off-stoichiometric alloys were essentially brittle.

This section contributes to the simulations of the dislocation core structures in off-stoichiometric NiAl, with particular focus on Ni-48Al. Changes in stoichiometry were accomplished by introducing randomly distributed antisite defects. A good random number generator routine is generally machine dependent. Several routines from different sources (e.g. Cornell University, Sandia National Lab, CCP5) have been tested for the off stoichiometry simulation. The one based on linear congruential generators and the shuffling routine suggested by Knuth [17] is incorporated into the program. The new program allows the off stoichiometry change for both Al and Ni atoms. Same as the introduction of point defects at

the core, because of the periodic boundary conditions along dislocation line z, two unit cells in the direction of the dislocation line were employed to avoid the interaction between antisite defects. In this way, antisite defects were actually generated as a randomly distributed row of antisite defects parallel to the dislocation line.

6.3.2 ⟨100⟩ Dislocations

Figure 6.11 shows the core structures of the edge ⟨100⟩(010) dislocation in off stoichiometric NiAl. It shows clearly that the dislocations in off stoichiometric NiAl are more spread than that in the stoichiometric alloy. These core structures can be understood by considering the interactions between the dislocation and the antisite defects. As discussed before (Section 6.1), Ni antisite defects produce less distortion than Al antisites. The core structure in Ni-52Al is more extended than the one for Ni-48Al. The former has Al antisite defects and the latter has Ni antisite defects. In order to see what happens when more antisite defects are introduced, the core structure in Ni-42Al is shown in Figure 6.11(d). Although the core structures in all cases change substantially, the spreading on compact planes (110) for this dislocation remains.

Figure 6.12 shows the core structures of the ⟨100⟩(110) pure edge dislocation, which is the dislocation with lowest Peierls stress. From the comparison of Figure 6.12(b) and (c), which are for the same overall composition (Ni-48Al) but different atom arrangement near the core, it is notable that the core structures are different. This means that the core structures are sensitive to their local atomic arrangement near the core region in this near stoichiometric composition. The core structures of pure screw ⟨100⟩ dislocation are shown in Figure 6.13

6.3.3 ⟨110⟩ Dislocations

The core spreading of ⟨110⟩ dislocations in stoichiometric NiAl is constrained in (110) planes, which is quite different from the cores of ⟨100⟩ and ⟨111⟩ dislocations. However, it can not be considered as a planar core, because for planar cores, the distortions in the core region occur only in one or two atomic planes. Actually, there is no planar core found in B2 NiAl. Figure 6.15 shows the core structures of pure screw ⟨110⟩ dislocation. Figure 6.14 is for the case of pure edge ⟨110⟩ dislocation. Again, the core structures become more extended they

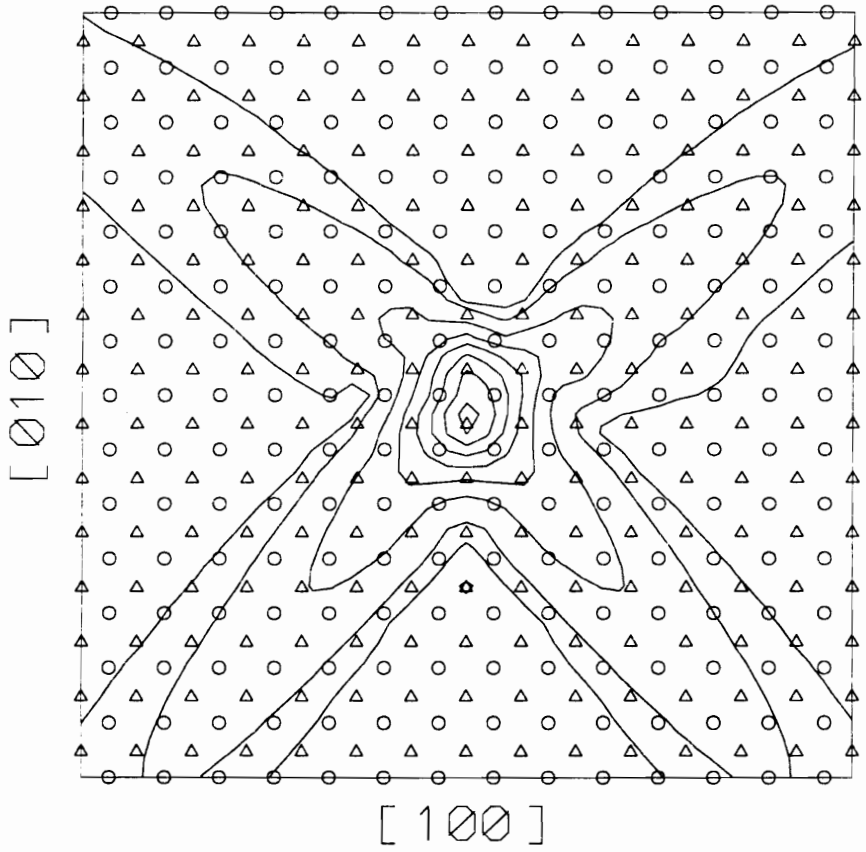

Figure 6.11(a)

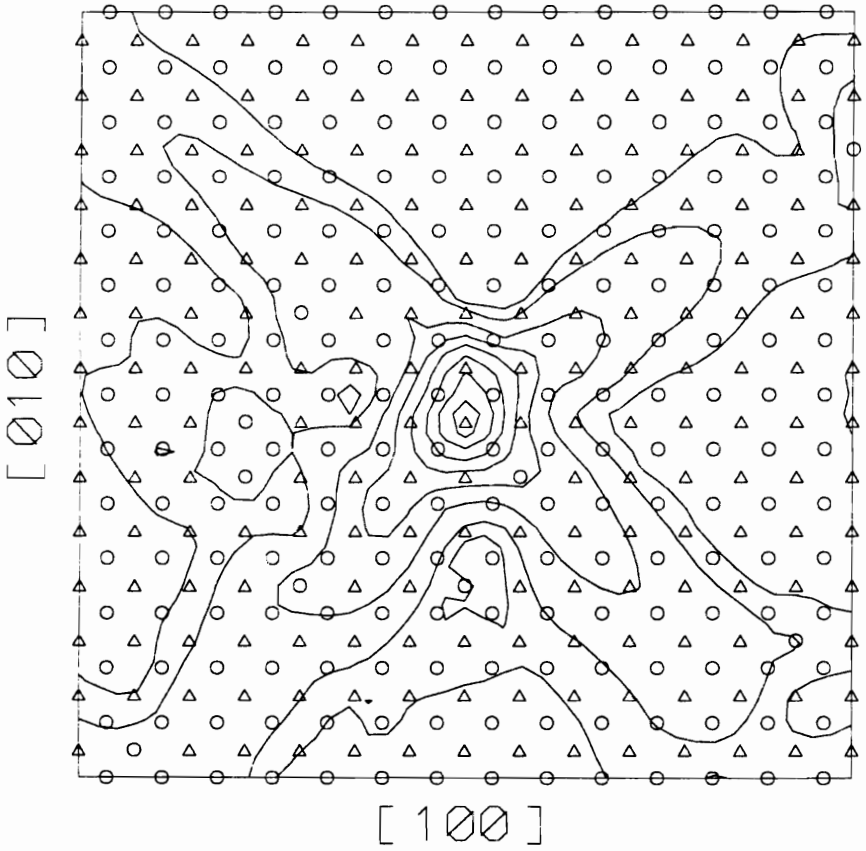

Figure 6.11(b)

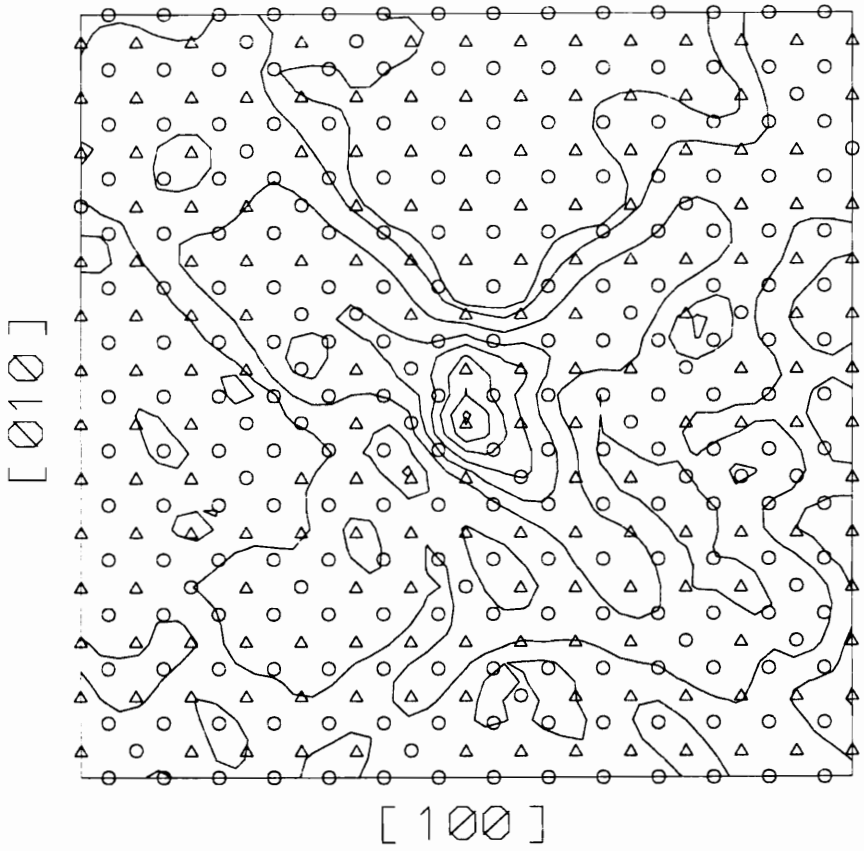

Figure 6.11(c)

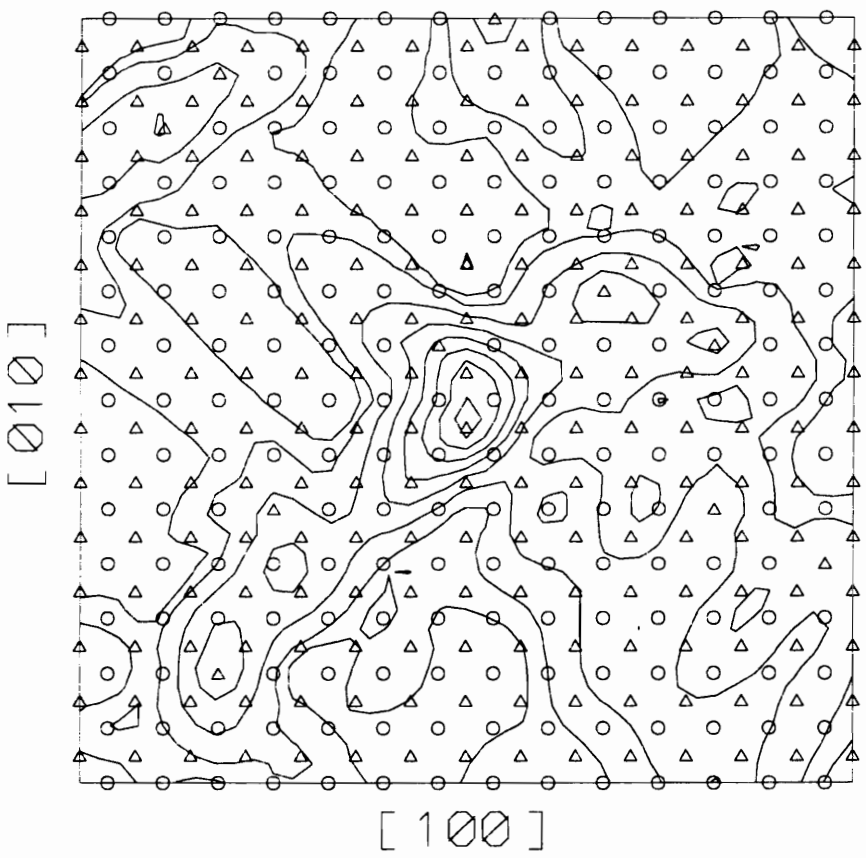

(d)

Figure 6.11: Core structures of ⟨100⟩(010) edge dislocations in (a) stoichiometric NiAl, (b) Ni-48Al, (c) Ni-42Al, and (d) Ni-52Al. △-Al atom, ○-Ni, rms strain levels $\epsilon = \sqrt{Y}/2$ increase towards the figure center according to the series 1%, 2%, 4%,..., 20%, same as the figures in Chapter 4

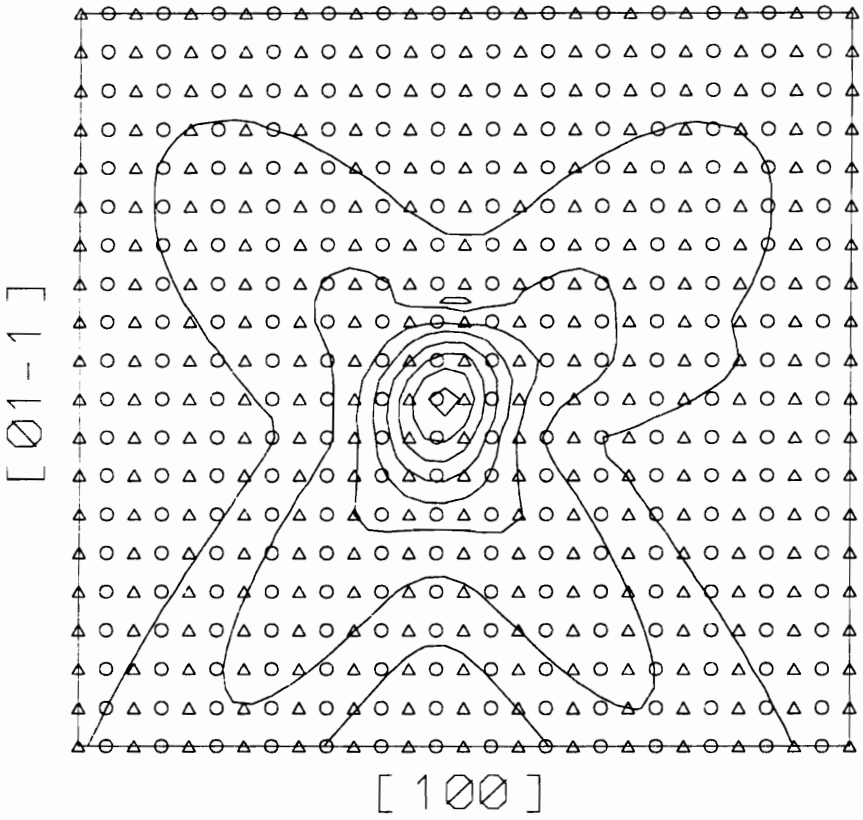

Figure 6.12(a)

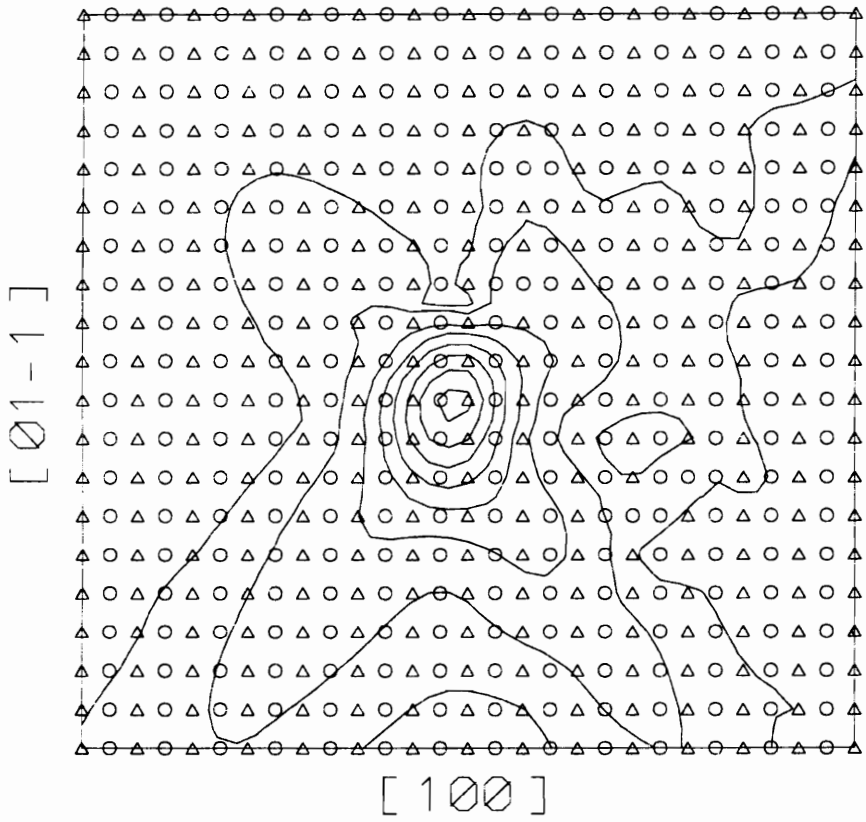

Figure 6.12(b)

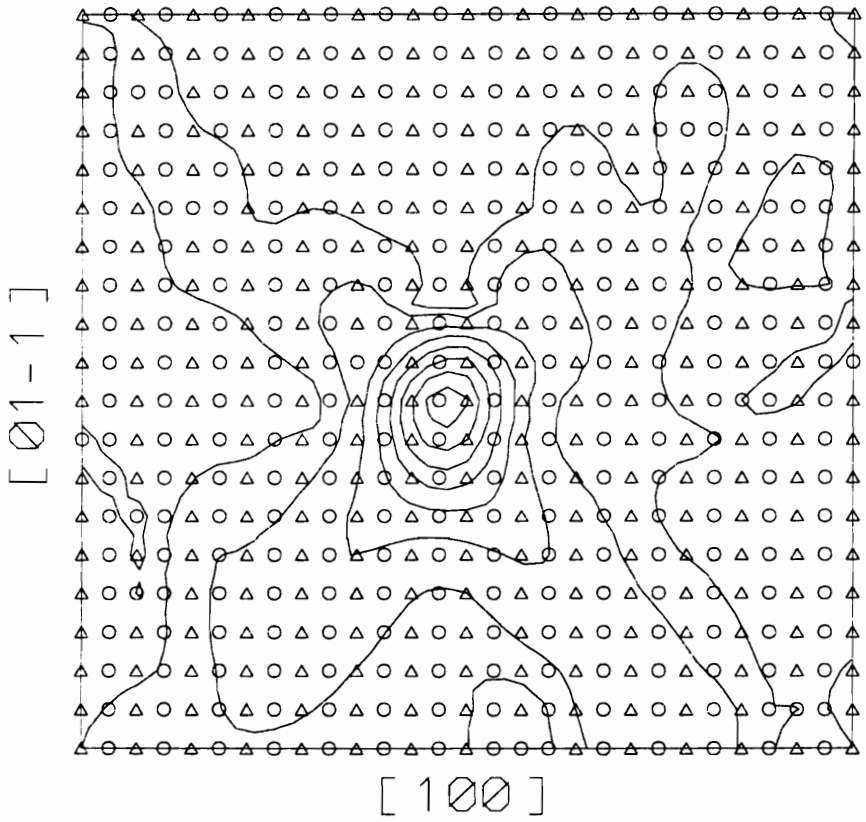

(c)

Figure 6.12: Core structures of ⟨100⟩(110) edge dislocations in (a) stoichiometric NiAl, (b) Ni-48Al, (c) Ni-48Ni with the different local atomic arrangement from (b). △-Al atom, ◯-Ni, rms strain levels are the same as Figure 6.11

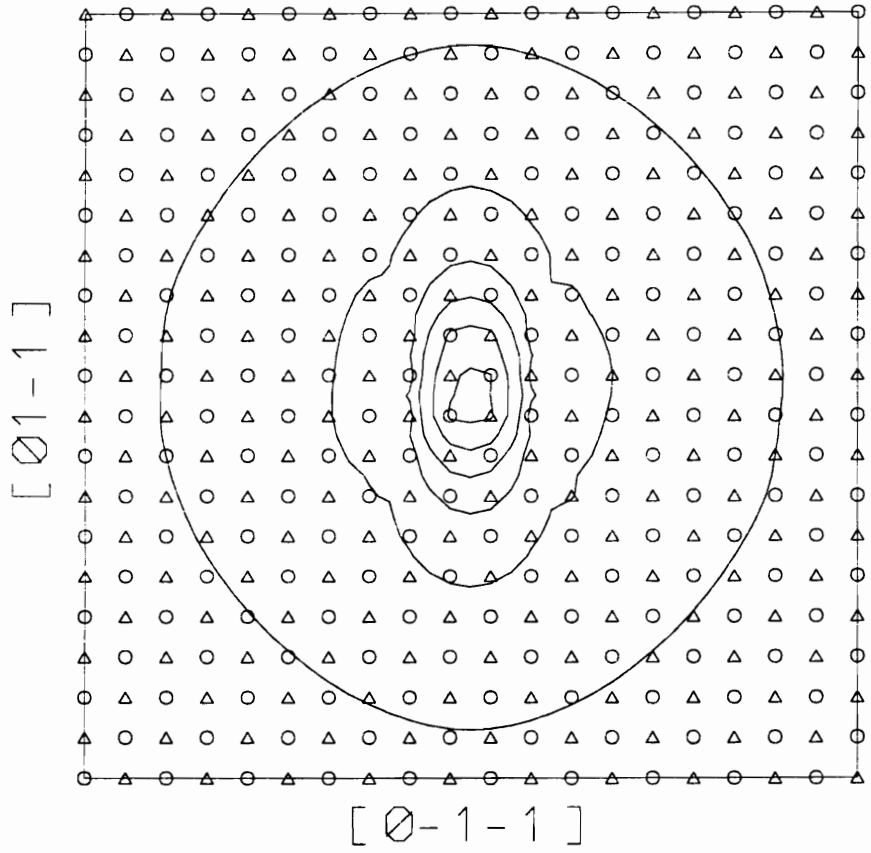

Figure 6.13(a)

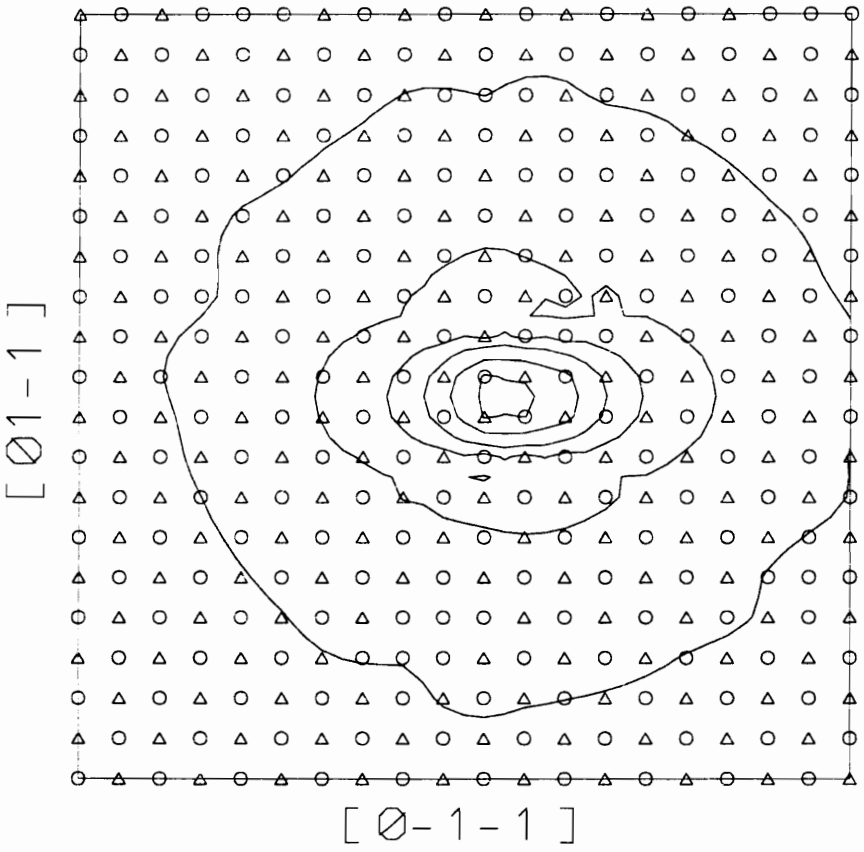

(d)

Figure 6.13: Core structures of ½00 screw dislocations in (a) stoichiometric NiAl, (b) Ni-48Al. △-Al atom, ◯-Ni, rms strain levels are the same as Figure 6.11

are in off stoichiometry.

6.3.4 ⟨111⟩ Dislocations

⟨111⟩ dislocations were expected to be stabilized and to be operative in the deformation processes, since ⟨100⟩ dislocations do not provide enough slip systems, as discussed in Section 6.2. Figure 6.10 shows the core structures of pure ⟨111⟩ dislocations in stoichiometric and off stoichiometric NiAl. The core extends much wider than the one with locally introduced point defects. Again, no energetically stable dissociation was found. It is unlikely that the dissociation into two partials could be stabilized through the deviation from stoichiometry.

6.3.5 Effects of Off-stoichiometry on Peierls Stresses

The same procedures as for the stoichiometric cases were applied to calculate the Peierls stresses of the dislocations in off stoichiometry NiAl. As mentioned in Chapter 4, the absolute values are less important. However, the relative values or the comparison of the values provide the information of dislocation mobility. Besides, getting exact number of Peierls stresses is time-consuming. For these reasons, we apply the same value of the Peierls stress for the dislocation in stoichiometric NiAl to the corresponding dislocation so that we can judge whether the Peierls stress increases or decreases. The results are shown in Table 6.8.

It is interesting to note that for the dislocations with relatively low values, the Peierls stresses increase upon off stoichiometry, while for the dislocations with relatively high values, the Peierls stresses decrease.

6.3.6 Concluding Remarks

⟨100⟩, ⟨110⟩, and ⟨111⟩dislocations in off stoichiometric NiAl (mostly, in Ni-48Al) have been simulated. The dislocation core structures in off stoichiometric NiAl became more extended than the ones in the stoichiometric NiAl. The core structures are not only dependent on the overall composition but also on their local atomic arrangement near the core region. The Peierls stresses increase for the dislocations that are relatively easy to move in stoichiometric

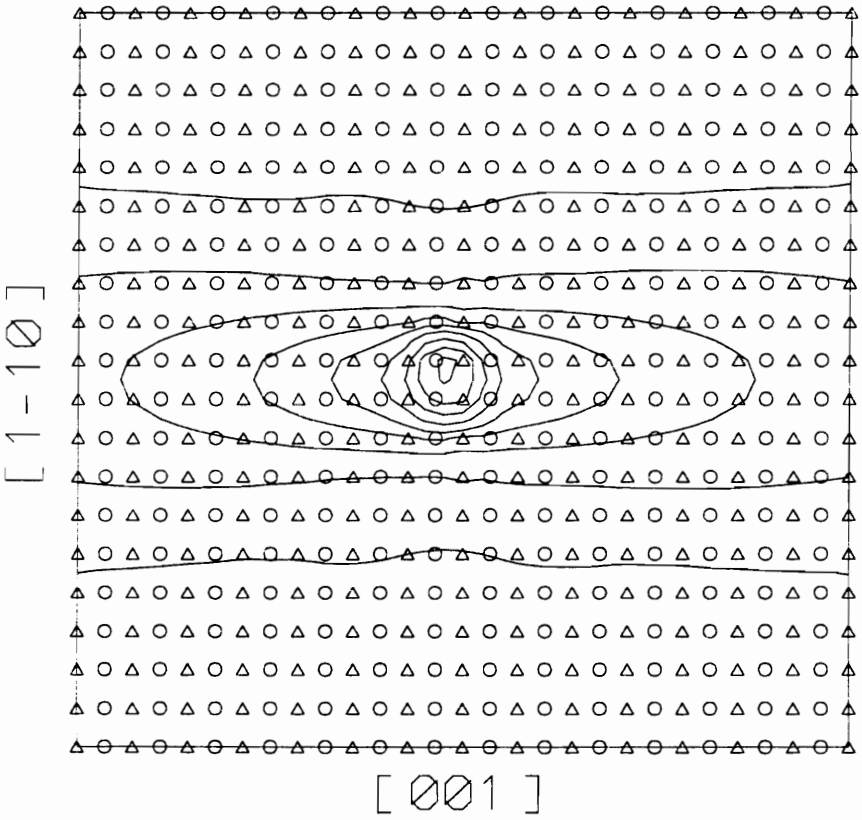

Figure 6.14(a)

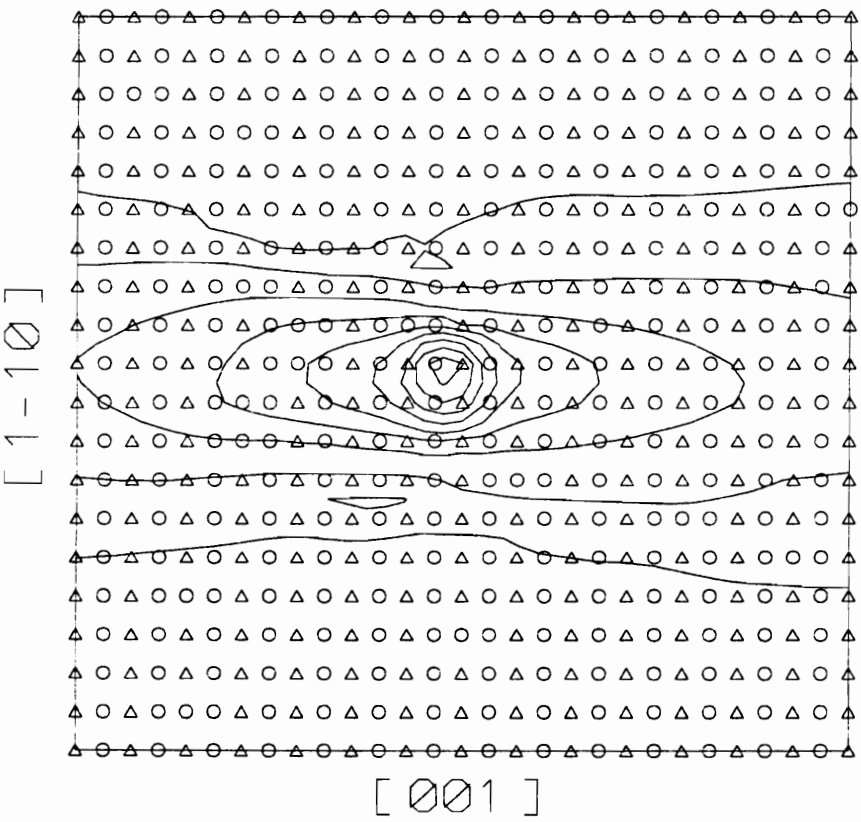

(b)

Figure 6.14: Core structures of ⟨110⟩screw dislocations in (a) stoichiometric NiAl, (b) Ni-48Al. △-Al atom, ◯-Ni, rms strain levels are the same as Figure 6.11

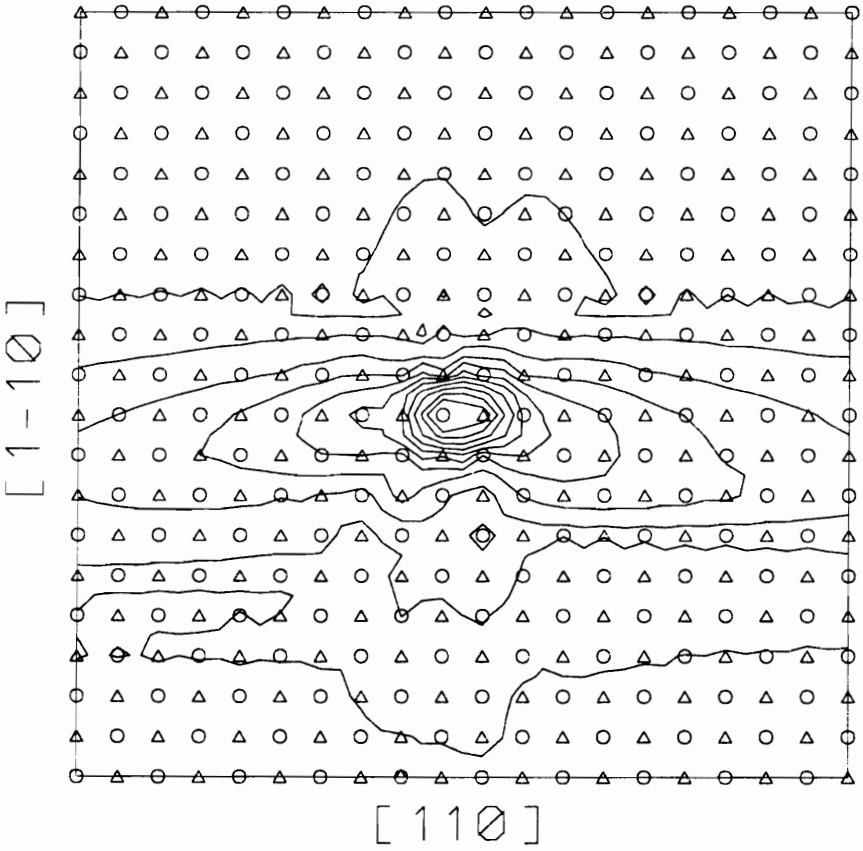

Figure 6.15(a)

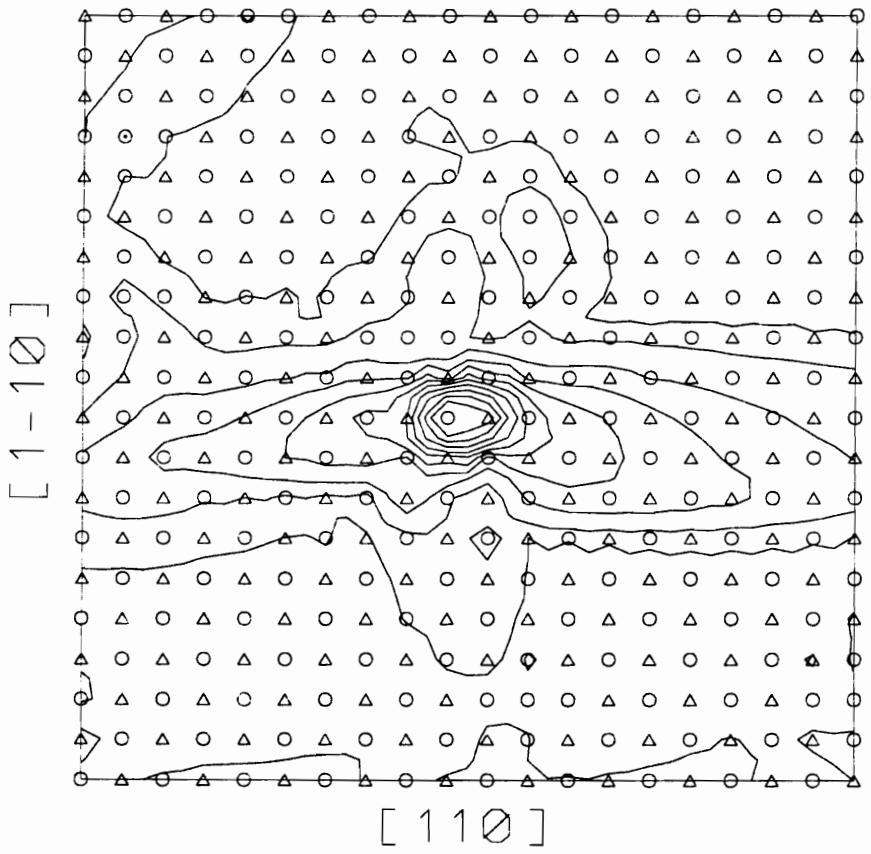

(b)

Figure 6.15: Core structures of ⟨110⟩edge dislocations in (a) stoichiometric NiAl, (b) Ni-48Al. △-Al atom, ◯-Ni, rms strain levels are the same as Figure 6.11

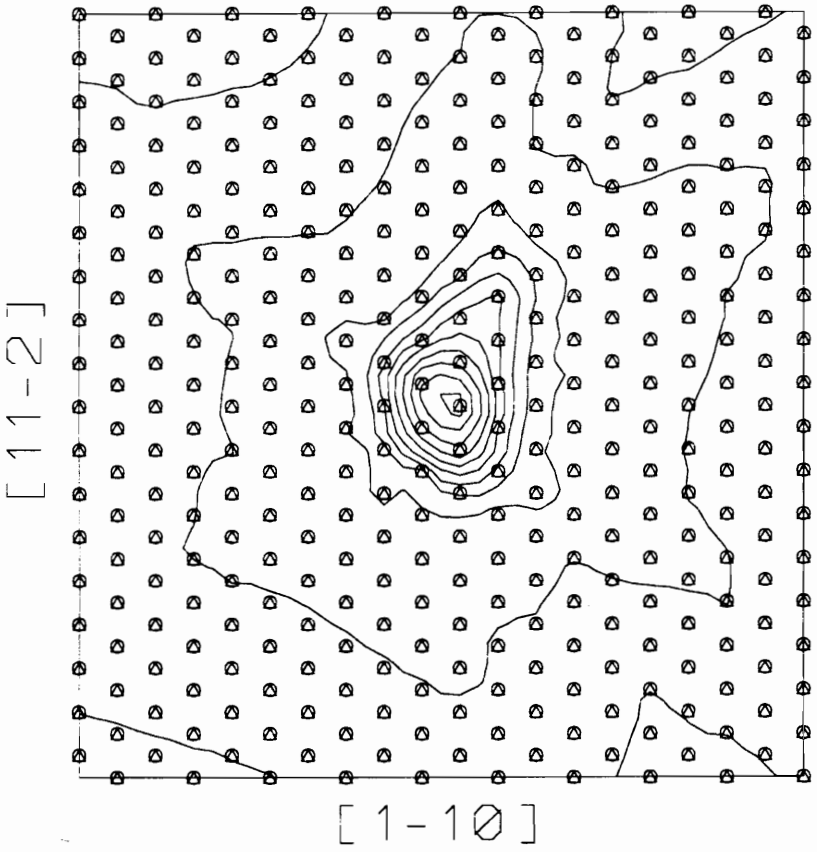

Figure 6.16(a)

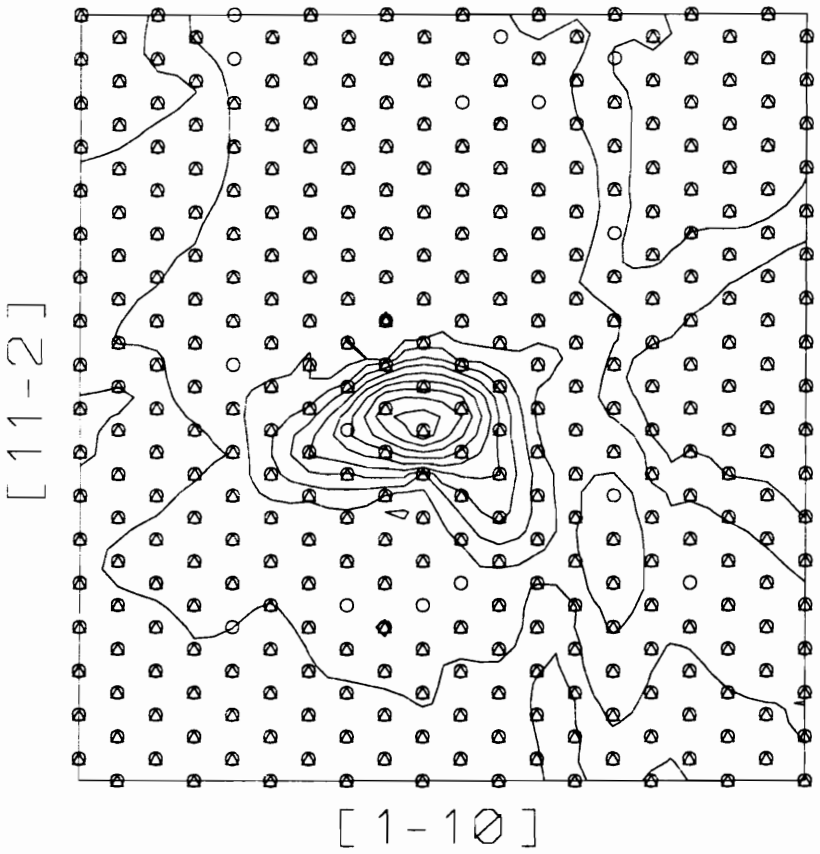

(b)

Figure 6.16: Core structures of ⟨111⟩ screw dislocations in (a) stoichiometric NiAl, (b) Ni-48Al. △-Al atom, ◯-Ni, rms strain levels are the same as Figure 6.11

Table 6.8: Changes of the computed Peierls stresses for Ni-48Al

b	x	y	z	$\sigma(\times 10^{-2}\mu)$	$\sigma(MPa)$	Ni-48Al
[100]	[100]	[001]	[0$\bar{1}$0]	1.11	1387.5	↓
[100]	[$\bar{2}$10]	[001]	[120]	0.79	987.5	↑
[100]	[110]	[001]	[1$\bar{1}$0]	1.57	1962.5	↓
[100]	[$\bar{1}$20]	[001]	[210]	2.36	2950.0	↓
[001]	[100]	[010]	[001]	0.47	1562.5	↓
[100]	[100]	[01$\bar{1}$]	[011]	0.36	450.0	↑
[100]	[$\bar{4}$11]	[01$\bar{1}$]	[$\bar{1}$22]	0.44	550.0	↓
[100]	[$\bar{2}$11]	[01$\bar{1}$]	[111]	1.54	1925.0	↓
[100]	[$\bar{1}$11]	[01$\bar{1}$]	[211]	0.83	1037.5	↓
[100]	[0$\bar{1}\bar{1}$]	[01$\bar{1}$]	[100]	0.38	475.0	↑
[110]	[001]	[1$\bar{1}$0]	[110]	7.86	9825.0	↑
[110]	[110]	[1$\bar{1}$0]	[00$\bar{1}$]	8.18	10225.0	↓
[111]	[1$\bar{1}$0]	[11$\bar{2}$]	[111]	6.29	7862.5	↑
[111]	[11$\bar{2}$]	[1$\bar{1}$0]	[111]	7.18	9003.0	↑

NiAl.

Chapter 7

Discussion and Summary

In this chapter, we compare the present results with other similar simulations using different methods and interatomic potentials, and experimental observations in the literature. If the agreement is reasonable, such a comparison will serve as a means of developing an understanding of the mechanisms underlying the slip response of NiAl.

Of the experimental observations that are available in the literature, two kinds of information are directly relevant to the present work and can be used in comparison with the present results. They are (1) the critical resolved shear stress for the different slip systems in NiAl and (2) detailed transmission electron microscopy (TEM) characterization of the type and morphology of the dislocation substructure in strained specimens. Additionally, in some investigations slip line trace analyses have been conducted and the results have been used to infer the slip plane and the occurrence of cross-slip if any. Other relevant information that can be indirectly related to the present work deals with the effects of surface films and the pre-existing substructure on the ductility and fracture behavior of NiAl. More recently, high resolution transmission electron microscopy (HRTEM) has been used to examine the core structure of dislocations in NiAl [44, 75]. It becomes available for a direct comparison of the simulated core with the HRTEM lattice image of the dislocations.

7.1 Comparison of Simulated Core Structures with HRTEM Results

HRTEM has been used to observe the core structures of ⟨100⟩ edge dislocations in bicrystals of stoichiometric NiAl [44], and ⟨100⟩edge dislocations in deformed stoichiometric and off stoichiometric (Ni-48Al). Shown in Figure 7.1 (a) is an HRTEM image of the core of a ⟨100⟩ dislocation. As discussed in Chapter 4, there are two kinds cores of this dislocation from the simulation. The lowest energy [100] core simulated is shown in Figure 7.1 (b), and the bright dots are the actual relaxed atomic positions. Usually, a comparison is made between direct HRTEM images and the simulated HRTEM ones generated by the multi-slice method using the Electron Microscopy Software (EMS) package of Stadelmann [78] based on the relaxed coordinates from computer simulation. Under the conditions of the microscope parameters used in Ref. [44] (a spherical aberration coefficient of 10 nm, a Gaussian spread of defocus of 1.0 nm, and semi-angular beam divergence of 0.7 mrad) and Ref. [75] (near Scherzer conditions: a foil thickness of 5.74 nm and a defocus of 60 nm), the simulated image intensities exactly coincide with the atomic positions. For this reason, the comparison is directly made for the HRTEM images and the relaxed atomic coordinates from the computer simulations.

The HRTEM image in Figure 7.1 is from Ref. [75]. It is apparent that the fine details near the core region from HRTEM are not as clearly defined as in the surrounding crystal. This could be due to (1) surface relaxations due to the effect of the thin foil, (2) the presence of kinks along the dislocation. By overlaying HRTEM images and the atomic position from the simulation, it is found that both images match very well. This match is striking considering that the conditions used in the simulations are very dissimilar to the ones used in the experimental HRTEM. For example, in the simulation, it is presumed that zero absolute temperature and a single infinite straight dislocation in infinitely perfect crystals. It can be concluded that with the EAM potentials [16] and the present boundary conditions and the minimization technique, the present simulation has been able to determine the overall core structures of the dislocations in NiAl.

The HRTEM image and the simulation result of [100] dislocation in Ni-48Al are shown

in Figure 7.2. The core structure in Ni-48Al appears to be similar in nature but the spreading of the core is substantially wider than the one in stoichiometric NiAl, as can be seen in both HRTEM and the simulation. When the fine details are compared, keep in mind that the core structure is not only dependent on the overall composition but also the actual local atomic arrangement as mentioned in the preceding chapter, therefore the agreement is quite reasonable.

Experimental work on the dislocation substructure that develops during deformation has been mostly TEM observations on specimens strained at different temperatures. In these experiments, the Burgers vector and the plane containing the dislocation are determined. The morphology and frequency of occurrence of dislocations are used to infer the relative mobility of the dislocation and to verify qualitatively if the mobility of a dislocation varies with character.

In the case of NiAl, for $\langle 100 \rangle$ slip, the relative populations of the various line directions of the $\langle 100 \rangle$ dislocations on the $\{110\}$ planes [46] have been examined, and it has been found that the $\sim 54°$mixed dislocation ($\langle 111 \rangle$ line direction) is the most frequent with a density which is four times that of the edge character ($\langle 110 \rangle$ line direction). The screw character was the least frequently observed. The low density of the screws has been attributed to the elastic instability of this character; however cross-slip is often observed and the effect of stress on the stability is not known. The observed variation of the density of the dislocation with its character is consistent with the relative mobility calculated in the present study. The edge dislocation is the most mobile and the mixed dislocation with the $\langle 111 \rangle$ line direction is the least mobile. Although the core structure of the mixed dislocation provides a clue as to why the mixed dislocation has low mobility, it is not clear why the stress is significantly higher than those for the edge and the screw.

A similar observation has been made for the $\langle 111 \rangle$ dislocations when they occur in NiAl. Several investigators (e.g., Loretto and Wasilewski 1971 [42], Noebe *et al.* 1990 [46], Schneibel *et al.* 1993 [43]) have observed that the $\langle 111 \rangle$ dislocations with the screw orientation are usually long and straight and are most frequently observed.

An interesting and important observation in NiAl has been the lack of significant tensile ductility (<2%) in the single crystal form tested in the soft orientation at room temperature (Field *et al.* 1991 [79]). Further, the strain to failure has also been shown to be sensitive to the

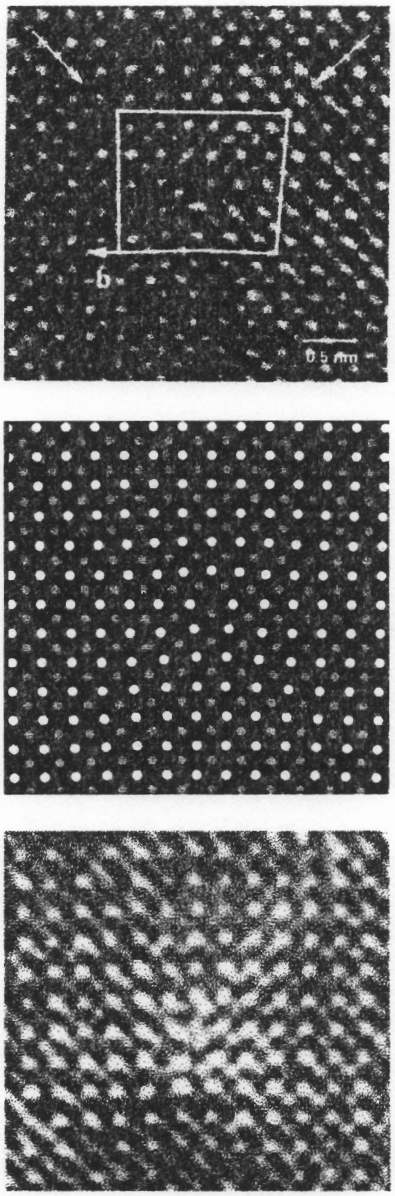

Figure 7.1: Comparison of HRTEM image with the simulation of [100] dislocation in stoichiometric NiAl. From top to bottom, HRTEM image from Ref. [44], the result of computer simulation, HRTEM image from Ref. [75]

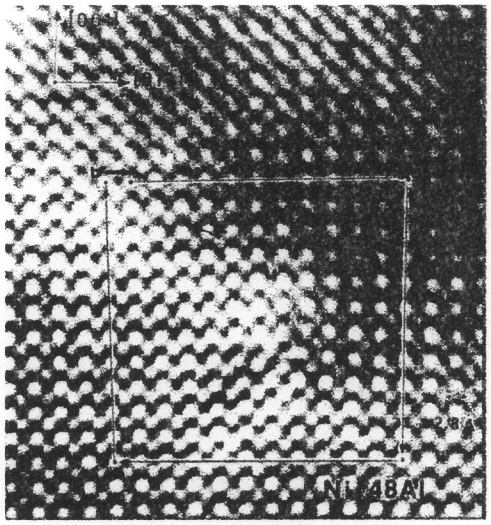

(a)

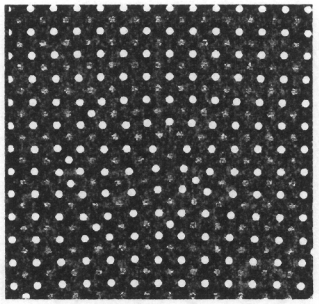

(b)

Figure 7.2: Comparison of HRTEM image with the simulation of [100] dislocation in Ni-48Al. (a) HRTEM image from Ref. [75], (b) the result of computer simulation.

presence of surface oxide films [46]. A plausible rationalization of these observations based on the results of the present simulations is as follows. The ⟨100⟩ dislocations show an anisotropy with respect to the ease of glide for the different line directions. This raises the possibility that the mobile segments of the ⟨100⟩ dislocations provide the initial flow, but when they are exhausted the immobile segments are left behind. Thus in post deformed specimens a large proportion of the relatively immobile segments are seen. The Peierls stress for this segment being significantly higher, fracture intervenes before further deformation can occur. This is also consistent with the softening induced by the injection of mobile segments of the ⟨100⟩ dislocations as observed in Ref. [46]. The descriptions of these phenomena will have to be expanded to include the effects of a net increase in the dislocation density, and the subsequent effects on ductility and toughness as observed experimentally.

The deformation behavior of [101] oriented single crystal Ni-48Al and stoichiometric NiAl has also been investigated by slip trace analysis and standard diffraction contrast Burgers vector analysis by Crimp *et al.* in Ref. [75]. Their slip trace analysis revealed the {100} and {110} planes to be the active slip planes. The most important features are that while the {110} planes appeared more dominant for the stoichiometric NiAl, the {100} planes became more active in Ni-48Al [75]. The calculated Peierls stresses show that the most active $\langle 100 \rangle (01\bar{1})$ dislocation contributing to the deformation processes became more difficult to move when off stoichiometry, with the values changing from 450 MPa to 900 MPa, which is very comparable with the experimental results as compiled by Miracle [12] as shown in Figure 7.3. In contrast, the minimum stress required to move ⟨100⟩(010) dislocations is lowered when the compositional deviations from stoichiometry are introduced (see Table 6.8). This is consistent with the results that ⟨100⟩(001) dislocations became more active in Ni-48Al.

7.2 Core Structure and Motion Behavior

There are no non-planar cores found in ⟨100⟩, ⟨110⟩, and ⟨111⟩ dislocations in B2 NiAl. The core spreading of ⟨100⟩ dislocations in NiAl (Chapter 4), can occur along a variety of planes with a very high probability of non planar behavior. ⟨110⟩ dislocation posses a multilayer structure spreading in {110} planes.

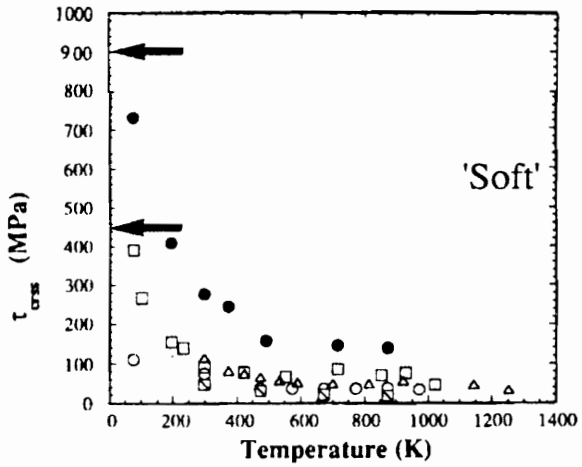

Figure 7.3: The critical resolved shear stress for ⟨100⟩ slip in "soft" direction [12]. Solid dots are for Ni-48Al, the rest for nominally stoichiometric NiAl; the arrows are from the present work, the upper arrow for Ni-48Al, the lower arrow for NiAl.

The dislocation $[100](01\bar{1})$ experiences the lowest Peierls stress. It must be pointed out that for most $\langle 100 \rangle$ and $\langle 110 \rangle$ dislocations reported in Chapter 4, there is no significant change in the core shape when stresses were applied. This is even true when the stress applied is slightly below the critical stress. Shown in Figure 7.4 is an example.

Two energetically equivalent configurations exist when two orthogonal $\{110\}$ planes intersect in the direction of dislocation line. This is especially interesting for a $\langle 100 \rangle$ screw dislocation, although the screw dislocation is elastically unstable. As reported [7, 37], when the stress is applied on the plane inclined more than 60° to the plane in which the core is spread, a transformation to core spreading onto another $\{110\}$ plane which is perpendicular to the original $\{110\}$ plane occurs. Therefore, the $\langle 100 \rangle \{0kl\}$ slip in B2 NiAl may be explained in terms of the continual cross-slip of $\langle 100 \rangle$ screw dislocations on two orthogonal $\{110\}$ planes.

In very early models[80], the dislocation core was assumed to be spread in a single crystallographic plane, identified with the slip plane, and the Peierls stress was derived to be

$$\tau_p = (2G/\alpha) \exp(-4\pi\zeta/b) \tag{7.1}$$

Where G is the shear modulus, ζ the width of the core and b the magnitude of the Burgers vector of the dislocation; $\alpha = 1$ for the screw and $1 - \nu$ for the edge dislocation, where ν is the Poisson ratio. τ_p clearly decreases with increasing ζ but even for rather narrow cores e.g. when $\zeta = b$, $\tau_p \sim 10^{-5}G$ when taking $\nu = 1/3$. From these models, the width of the core is largest for the most closely packed planes. Hence it was concluded that these planes are the most likely slip planes since they possess the lowest lattice friction stress. This prediction appears to be in agreement with experiments in which the studies on single crystals were carried out at that time mainly on pure fcc metals, such as Cu, and some hcp metals, e.g. Zn. In the former case the slip was found to be always confined to $\{111\}$ planes and in the latter case usually to the basal planes. The reason for this agreement is that the core of the dislocations and their partials are planar, confined to the (111) plane for fcc metals and to the basal plane for hcp metals, as confirmed by several atomistic calculations [80]. This planarity of the core is responsible for a very low Peierls stress. For bcc based B2 crystal structure NiAl, the planarity of the core totally disappeared. The validity of the original Peierls-Nabarro relation (Eq. 7.1) for B2 NiAl

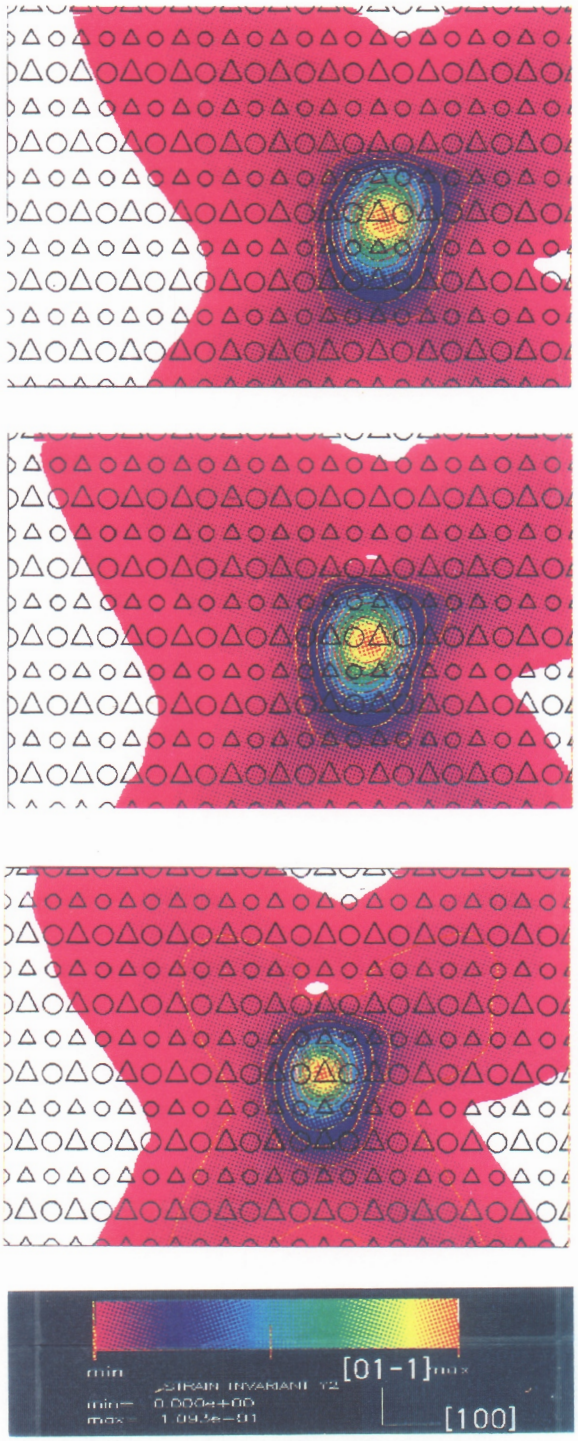

Figure 7.4: Core structures of $[100](01\bar{1})$ edge dislocations under stresses. Top: without stress, middle: stress slightly below the critical, and bottom: under the critical stress.

is questionable. Several attempts have been made to correlate the Peierls stresses and the core size parameters, such as, projections in the slip plane and perpendicular to the slip plane of core spreading maximum corresponding to different strain levels, the product of these two projections, width of the spreading in the slip plane, width of the spreading perpendicular to the slip plane. The outcome is that there are no definite correlations between the Peierls stresses and the core size parameters considered. Figure 7.5 shows an example, where the core sizes are measured for the $\langle 100 \rangle$ dislocations presented in Chapter 4 corresponding to 2% strain level.

It is interesting to compare the present results with those obtained in Ref. [81] where different interatomic potentials, fixed boundary conditions, and the steepest descents minimization technique were used. Figure 7.6 and Figure 7.7 are for an [100] pure edge dislocation. It can be seen that the essential feature of this dislocation is a non-planar core spread on the two intersecting $\{110\}$ planes for both the present work and for the work done in Ref. [81]. The Peierls stress for this dislocation in the (010) plane is 1387.5 MPa from the present work and 2580 MPa from Ref. [81], and in the $(01\bar{1})$ plane is 450 MPa from the present work and 320 MPa from Ref. [81]. The potentials in Ref. [81] were developed within the same regime of EAM as the potentials we used. However, the authors [81] claimed that their potentials were better because they yielded a better fit to the elastic constants of NiAl. That the core structures from the two investigations are similar but the Peierls stresses are different implies that core structures are not sensitive to the details of interatomic potentials but that the Peierls stresses are. These conclusions are consistent with the conclusions from the recent review by Vitek [82] on interatomic potentials in relation to the theory of dislocations. It appears that the core structures are not the only controlling factor to affect the movement in the slip plane for non-planar core cases. It is notable that the present value of Peierls stress for the $(01\bar{1})$ slip is larger than the one from Ref. [81] whereas the present value for the (010) slip is smaller than the one from Ref. [81]. As discussed in Chapter 2, fixed boundary conditions give no reliable result of Peierls stress for (010) slip (see Table 2.2). It is possible that the difference of Peierls stresses for (010) slip is due to the fixed boundary conditions imposed in Ref. [81] rather than the interatomic potentials. Their Peierls stress for $(01\bar{1})$ slip deviates from the present value by 28%, within the acceptable deviation range of shear modulus from different interatomic

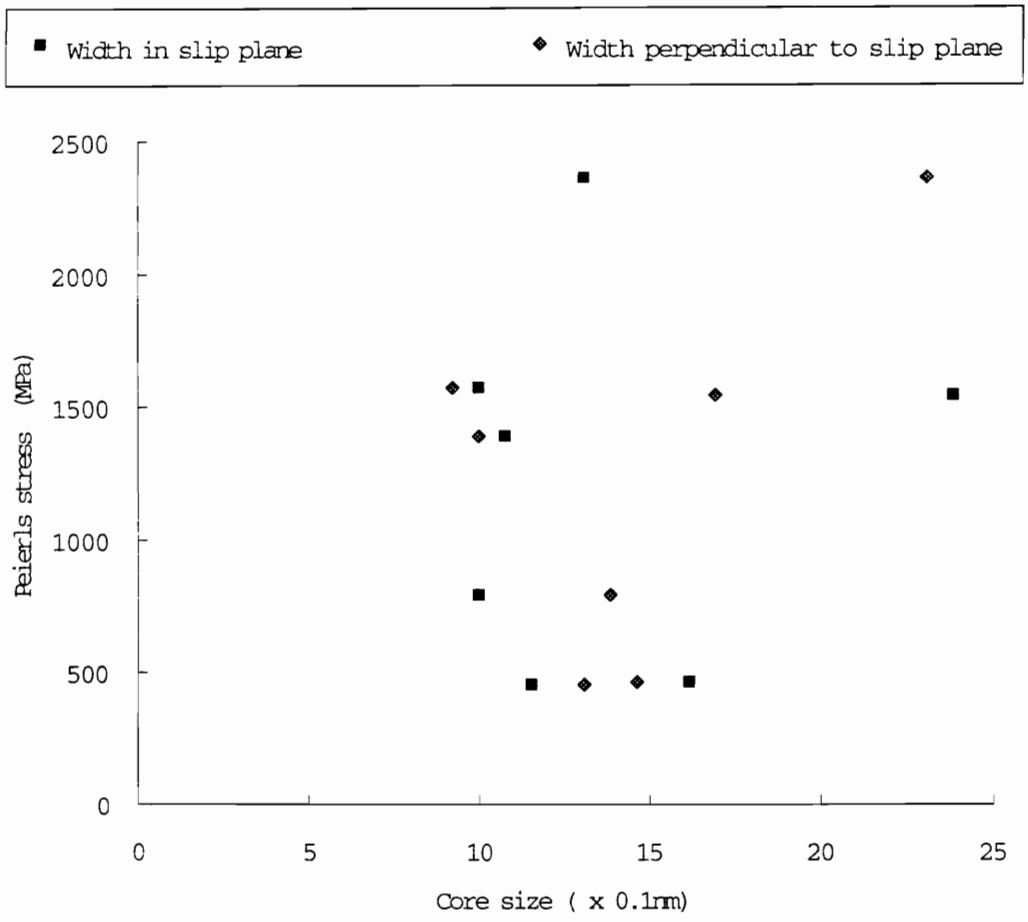

Figure 7.5: Core size of ⟨100⟩ dislocations and the Peierls stresses.

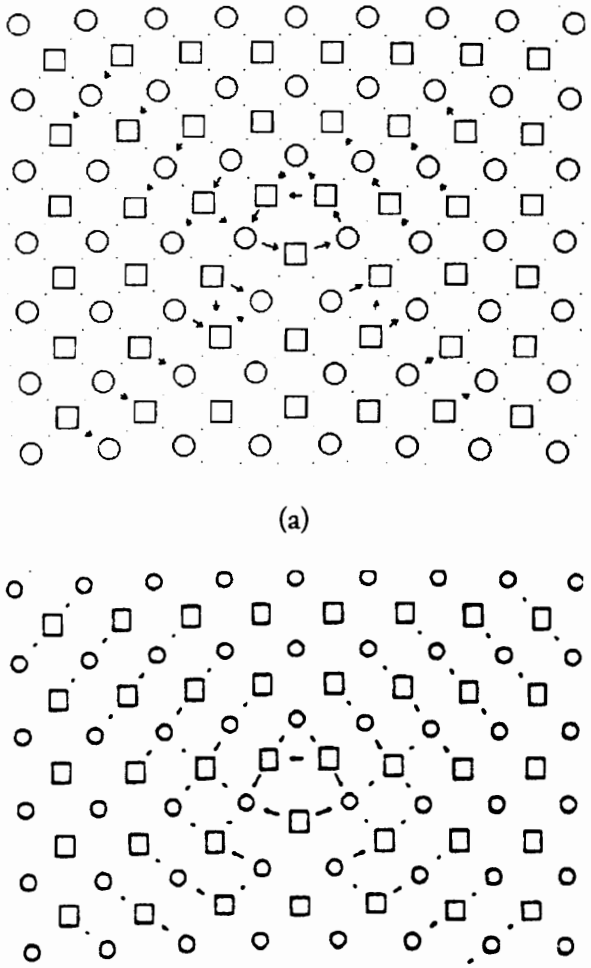

Figure 7.6: Comparison of the present [100](010) dislocation core structure with the one from Ref. [81]. Crystallographic direction: horizontal axis-[100], vertical-[010]. (a) The present simulation with Peierls stress: 1387.5 MPa, (b) From Parthasarathy *et al.* [81] with Peierls stress: 2580 MPa.

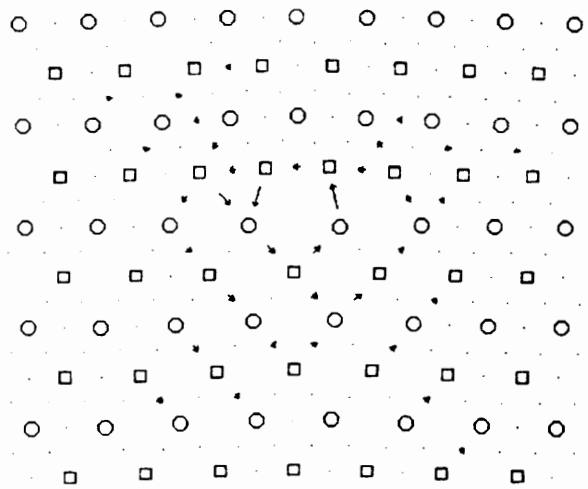

(a)

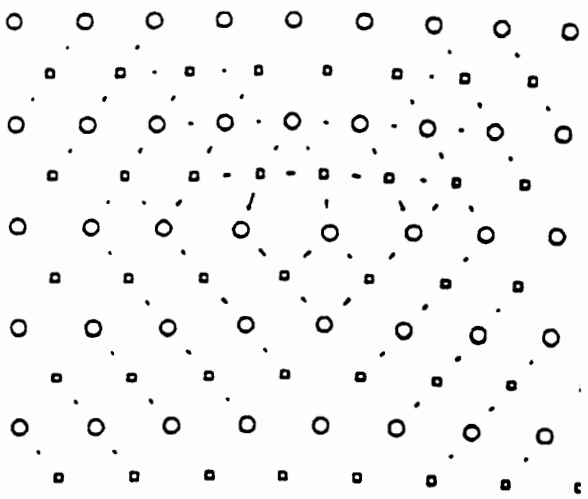

(b)

Figure 7.7: Comparison of the present [100](01$\bar{1}$) dislocation core structure with the one from Ref. [81]. Crystallographic direction: horizontal axis-[100], vertical-[01$\bar{1}$]. (a) The present simulation with Peierls stress: 450 MPa, (b) From Parthasarathy *et al.* [81] with Peierls stress: 320 MPa.

potentials.

The $\langle 111 \rangle$ screw dislocation is stable with respect to the two dissociated $1/2\langle 111 \rangle$ superpartials with an APB in between in the present simulation. However, this dissociated configuration is metastable and could be stabilized through alloying additions. There are two core configurations for complete $\langle 111 \rangle$ (see Figure 5.2) which are no longer energetically equivalent as the case for bcc lattice. The effect of an external shear stress upon the $\langle 111 \rangle$ superlattice screw dislocations in the B2 structure have also been shown in Chapter 5. As shown in Figure 5.9, the superpartials show a strong tendency to slip along the twinning $\{112\}$ planes. Differences are usually found in the behaviour of the two superpartials. The trailing partial seems more difficult to move than the leading one. The two most important factors controlling the motion of $\langle 111 \rangle$ dislocations are their core structure and its transformations under the effect of the applied shear stress. In particular, it is the restoring force of the faults created under the effect of the applied shear stress which governs the core transformation [7].

7.3 Comparison of Peierls Stresses with CRSS

In comparing the data on critical resolved shear stress with the present results, only qualitative information is expected. The reasons are as follows. First, the simulations (molecular statics) were performed effectively at 0K and an extrapolation of the experimental data (77K and above) to 0K is not straightforward. Second, the simulations were performed on straight dislocations that move uniformly through their length, while in reality kinks play a significant role. It is also likely that for the most planar and glissile core configurations, extrinsic obstacles (solute atoms) will contribute to the critical resolved shear stress determined experimentally. Third, as shown by the work (Duesbury,1984 [83]) on bcc structures, non-glide stresses may have significant effects on the minimum stress to initiate motion of dislocations in a B2 structure and these components will be present in the experiments with real materials. Fourth, as seen from the present results the stress required to initiate motion of a dislocation depends not only on the Burgers vector and slip plane normal (which define the slip system), but also the line direction of the dislocation. This makes it difficult to specify the critical resolved shear stress for a particular slip system. One possibility is that the more "mobile" segments determine the

critical resolved shear stress, and as these segments get exhausted, the less "mobile" segments are stored as substructure. On the other hand it is possible that the flow is limited by the relatively immobile segments. Such distinctions between glide systems acting in series and those acting in parallel are not established at any temperature for NiAl. For these reasons, it is reasonable to expect only a qualitative agreement in terms of a ranking of the various slip systems in the order of their relative mobility, and the relative probabilities for contribution to plastic deformation.

With regard to the dislocation substructures in strained specimens observed in TEM, the most abundant dislocation type is usually given importance and reported on. The Burgers vector and the slip plane normal of the dominant dislocation are taken to be the operative slip vector and slip plane respectively. Further, the character of the dislocation that is most abundant is suggested to be the least mobile especially if the dislocation is long and straight, although the straightness at the microscopic level is not usually given importance. Thus, in terms of comparison with simulation results, it appears that for a given slip system the least mobile character of the dislocation will correlate with the most abundant character observed experimentally, although it is expected that many unobserved dislocation processes have taken place which lead to the observed substructure.

Based on the above, a discussion of the simulation results and the corresponding experimental work reported in the literature is presented below. Table 7.1 shows the Peierls stresses of the screw and edge dislocations of the various slip systems. Considering the screw and edge dislocations of the various systems studied in the present work, the $\langle 100 \rangle$ dislocations on the $\{110\}$ planes are the easiest to move, as can be seen from Table 7.1. This slip system has been experimentally observed to be the most favored [37, 46, 42]. The critical resolved shear stress at 77K is about 400 MPa ([77]) for $\langle 100 \rangle$ slip in stoichiometric NiAl, and it is about 750 MPa in off stoichiometric Ni-48Al[77, 79]. It has not been possible to deduce this preference for $\langle 100 \rangle$ slip from elasticity calculations (e.g., Ball and Smallman [37]), which predict $\langle 111 \rangle$ and $\langle 110 \rangle$ slip to be easier than $\langle 100 \rangle$ slip. The preference for the $\langle 100 \rangle$ slip as against $\langle 111 \rangle$ slip can be expected to scale with the APB energy, since $\langle 111 \rangle$ is the preferred slip direction in bcc structures and $\langle 111 \rangle$ is preferred in B2 structures with lower APB energy. For example, in FeAl, which has a lower APB energy (240 mJ/m^2) than NiAl (>400 mJ/m^2), $\langle 111 \rangle$ slip is

Table 7.1: Calculated critical stresses for pure edge and screw dislocations

Slip system	Dislocation type	$\sigma(\times 10^{-2}\mu)$	$\sigma(MPa)$	Ni-48Al
$\langle 100\rangle(01\bar{1})$	edge	0.36	450.0	$\uparrow$
	screw	0.31	380.0	$\uparrow$
$\langle 100\rangle(001)$	edge	1.11	1387.5	$\downarrow$
	screw	1.00	1250.0	$\downarrow$
$\langle 111\rangle(11\bar{2})$	screw	5.03	6290.0	$\uparrow$
$\langle 111\rangle(01\bar{1})$	screw	5.76	7202.4	$\uparrow$
$\langle 110\rangle(01\bar{1})$	screw	6.28	7860.0	$\uparrow$
	edge	6.54	8180.0	$\downarrow$

known to be favored.

The present simulations predict $\langle 111 \rangle$ slip on $\{112\}$ planes to be slightly easier than $\langle 111 \rangle$ slip on $\{110\}$ planes. However, at elevated temperatures, the effect of the APB becomes rather important and therefore slip on the $\{110\}$ plane where the APB energy is the lowest may become dominant. Experimentally, in NiAl $\langle 111 \rangle$ slip has been observed on both $\{110\}$ and $\{112\}$ planes and cross-slip between these two planes have been observed [42, 46]. The values of Peierls stress of $\langle 111 \rangle$ dislocations in Table 7.1 are for the complete $\langle 111 \rangle$ dislocations. The core structures changed significantly when dissociation was assumed (see Figure 5.3 and 5.6). The stress to initiate the motion of the dissociated superpartials may change substantially. For $\langle 110 \rangle$dislocations, the $\langle 110 \rangle\{110\}$ slip system has not been observed experimentally to operate except for the "hard" orientation and only above 300°C to 400°C (Field *et al.* [79]). This is consistent with expectations from the simulation results. Mills and Miracle [44], suggested several probable dissociations of this dislocation. Non one of them is energetically stable. The present simulation results are for the complete $\langle 110 \rangle$ Dissociations of this dislocation has not been considered in the present work.

7.4 Limitations of the Present Simulation

The present simulations are molecular statics in nature, therefore, thermal activation processes can not be included in the simulations. The present work has not included the effects of non glide stresses and complex defect configurations. As discussed earlier, studies that include these effects may yield even better correlation with experimental observations.

7.5 Summary

Atomistic simulations, using an EAM potential and recently developed boundary conditions, were conducted to study the core structures of the $\langle 100 \rangle$, $\langle 110 \rangle$, and $\langle 111 \rangle$ dislocations in NiAl.

An important improvement to the simulation codes used in the present work is that the boundary atoms can be displaced according to the field given by a dipole moment tensor created

at the elastic center of the dislocation . The total energy of the block of atoms is then minimized with respect to the coordinates of all the atoms in the free move zone and the mismatch forces are offset by the components of the dipole moment tensor. These codes permitted the use of smaller atomic arrays than rigid boundary codes, gave better descriptions of core non-linear effects and allowed fair assessments of the Peierls stress for dislocation motion.

An advantage of graphic representation of dislocations using the strain invariants extrapolated from the computer simulation is the easy identification of core spreading corresponding to the various crystallographic planes and directions. Theoretically important is that these strain invariants are derived from continuum mechanics concepts. Therefore, they are more suited to bridge the gap between a discrete atomic picture and continuum models, which were so well developed for dislocations, and open to analysis of the core structure using other possible invariants, as visualization techniques for second order tensors will allow. The methods also allow the visualization of the motion of dislocation under applied stresses in a video form, where stresses are cast into time[30].

By applying the method of representing strain tensor invariants, we have been able to discuss consistently the dislocation core structures. The core spreading of $\langle 100 \rangle$ dislocations in NiAl, can occur along a variety of planes with a very high probability of non planar structures. The strain spreading is not necessarily along compact planes or relatively low Miller indices. The planes involved depend on dislocation slip plane and line orientation. The elastic solution generally determines the shape of the contour lines for the lattice strain field far from the dislocation core. The discrete character of the lattice imposes two main differences between "elastic" and "discrete" strains. First, the high strain levels imposed by the continuum solution at the dislocation core are lowered considerably in the relaxed structures. Second, the strain in the simulated results extends asymmetrically with respect to the origin, in contrast to the symmetry of the elastic solution. This is the lattice effect analogous to the twinning-antitwinning asymmetry on glide reported earlier for the 1/2[111] screw dislocation in bcc metals.

The core structure of the $\langle 110 \rangle$ dislocations is mutilayered with spreading on $\{110\}$ plane. The extent of the same strain level compared with $\langle 100 \rangle$ and $\langle 111 \rangle$ dislocations is much larger,

therefore, ⟨110⟩dislocations are very difficult to move. The complete ⟨111⟩ dislocations in NiAl are highly non planar and are stable with respect to splitting into exact $1/2\langle 111\rangle$ partials as well as with respect to alternative splittings that correspond to the stable fault in the vicinity of the APB, in both $\{110\}$ and $\{112\}$ planes. However, the alternative splitting has lower energy than the splitting in exact $1/2\langle 111\rangle$ partials. The structure of these metastable partials is also non-planar and it is different from the structure observed in bcc metals and in B2 materials described by model pair potentials.

Atomistic computer simulation has also been performed to study the energetics and structures of point defects in $L1_2$ Ni_3Al and B2 NiAl. The large size of Al atom plays a dominant role in the relaxed atomic configurations in the system. In both, Ni_3Al and NiAl it was found that excess Ni can be accommodated by Ni in Al sites, whereas such an accommodation of excess Al by Al in Ni sites is not energetically favorable. The effects of different degrees of random disorder on the lattice parameters were evaluated. The interaction behavior of vacancies in Ni_3Al and NiAl is quite different. In contrast to the general attraction in Ni_3Al , some two vacancies in NiAl show a repulsive interaction. The most stable divacancy in NiAl is that two vacancies sit in the Al sublattice as the second nearest neighbors. The probability of recombination of the vacancies is very small at zero temperature in this highly symmetrical structure. This explained the existence of the structural vacancies.

The effects of various possible local disorder on core structure have been simulated. Significant contributions only occur in the core in the immediate vicinity of the point defect. It is unlikely that local disorder changes could be used to successfully stabilize ⟨111⟩ slip. As a consequence, alloying efforts should be directed towards changing the APB energy of the NiAl-based alloy to a lower value.

⟨100⟩, ⟨110⟩, and ⟨111⟩dislocations in off stoichiometric NiAl (mostly, in Ni-48Al) have been simulated. The dislocation core structures in off stoichiometric NiAl became more extended than the ones in the stoichiometric NiAl. The core structures are not only dependent on the overall composition but also on their local atomic arrangement near the core region.

Peierls stresses of the dislocations have been calculated and have been compared for their relative ease of motion. Although the core structures generally experience more spreading

when compositional deviation from stoichiometry is introduced, the response to the applied stress is different for the various slip systems. In off stoichiometric B2 NiAl simulations, the Peierls stresses for the usually easiest moving $\langle 100 \rangle \{110\}$ dislocations increased and for the $\langle 100 \rangle \{100\}$ dislocations decreased, and the latter are expected to be more active in the deformation process.

Bibliography

[1] K. Aoki and O. Izumi. *J. Japan Inst. Metals*, 43:1190, 1979.

[2] C. T. Liu, C. L. White, and J. A. Horton. *Acta Metall. Mater.*, 33:213, 1985.

[3] For example. *High Temperature Orederd Intermetallic Alloys I–V.* MRS Procedings, 1985-1993.

[4] S. H. Whang, C. T. Liu, D. P. Pope, and J. O. Stiegler eds. *High Temperature Aluminides and Intermetallics.* TMS, Warrendale, PA 15086, 1990.

[5] *Advanced High Temperature Intermetallics (ISIJ).* Vol. 31, Special Issues Introduced by Y. Umakoshi amd M. Kato.

[6] C. T. Liu, R. W. Cahn, and G. Sauthoff eds. *Ordered Intermetallics–Physical Metallurgy amd Mechanical Behavior.* NATO ASI Series E: Applied Sciences Vol. 213.

[7] M. Yamaguchi and Y. Umakoshi. *Prog. Mater. Sci.*, 34:1, 1990.

[8] Robert W. Cahn. *The Materials Research Society Bulletin*, page 18, May 1991.

[9] M. H. Yoo, S. L. Sass, C. L. Fu, M. J. Mills, D. M. Dimiduk, and E. P. George. *Acta Metall. Mater.*, 41:987, 1993.

[10] I. Baker, R. Darolia, J. D. Whittenberger, and M. H. Yoo eds. *High Temperature Orederd Intermetallic Alloys V.* MRS Procedings, 1993.

[11] I. Baker and P.R. Munroe. In S. H. Whang, C. T. Liu, D. P. Pope, and J. O. Stiegler, editors, *High Temperature Aluminides and Intermetallics*, page 425. TMS, Warrendale, PA 15086, 1990.

[12] D. B. Miracle. *Acta Metall. Mater.*, 41:649, 1993.

[13] P. Nash, M. F. Singleton, and J. L. Murray. In P. Nash, editor, *Phase Diagrams of Binary Nickel Alloys*, volume 1. ASM, Metals Park, Ohio, 1991.

[14] I.M. Torrens. Interatomic potentials. page 49. Academic Press, 1972.

[15] M. S. Daw and M.I. Baskes. *Physical Review B*, 29:6443, 1984.

[16] A. F. Voter and S. P. Chen. In R. W. Siegel, J. R. Weertman, and R. Sinclair, editors, *Characterization of Defects in Materials*, page 175. Mat. Res. Soc. Symp. Proc. 82, 1987.

[17] W. Press, S. A. Teukolsky, W. T. Vetterling, and B. P. Flannery. *Numberical Rescipes in C.* Cambridge University Press, 1992.

[18] A. B. Lidiard and M. J. Norgett. In F. Herman, N. W. Dalton, and T. R. Keohler, editors, *Computational Solid State Physics*, page 385. Plenum, New York, 1972.

[19] M. J. Norgett, R. C. Perrin, and E. J. Savino. *Journal de Physique*, F2:L73, 1972.

[20] R. Pasianot, E. J. Savino, Z. Xie, and D. Farkas. *MRS Symposia Proceedings*, 291:85, 1993.

[21] V. Vitek. *Philosophical Magazine*, 18:773, 1968.

[22] J. E. Sinclair. *J. Appl. Phys.*, 42:5321, 1971.

[23] P. C. Gehlen, J. P. Hirth, R. G. Hoagland, and M. F. Kanninen. *J. Appl. Phys.*, 43:3921, 1972.

[24] J. E. Sinclair, P. C. Gehlen, R. G. Hoagland, and J. P. Hirth. *J. Appl. Phys.*, 49, 1978.

[25] A. N. Stroh. *Phil. Mag.*, 3:625, 1948.

[26] J. P. Hirth and J. Lothe. *Theory of Dislocations*, page 235, 1982.

[27] J. D. Eshelby, W. T. Read, and W. Shockley. *Acta Metall.*, 1:251, 1953.

[28] R. Pasianot, Z. Xie, D. Farkas, and E. J. Savino. *Scripta Met. et Mater.*, 28:319, 1993.

[29] Z. Xie, C. Vailhe, and D. Farkas. *Materials Science and Engineering A*, 170:59, 1993.

[30] Z. Xie, R. Kriz, and D. Farkas. In J. P. Hager, editor, *EPD Congress*, page 679. 1993.

[31] L.D. Landau and E.M. Lifshitz. *Theory of Elasticity.* Pergamon Press, New York, 1959.

[32] V. Vitek. *Crystal Lattice Defects*, 5:1, 1974.

[33] Z.S. Basinski, M.S. Duesbery, and R. Taylor. *Can. J. Phys.*, 49:2160, 1971.

[34] Z.S. Basinski, M.S. Duesbery, and R. Taylor. *Phil. Mag.*, 21:1201, 1970.

[35] V. Vitek, R.C. Perrin, and D.K. Bowen. *Phil. Mag.*, 21:1049, 1970.

[36] R. Pasianot, Z. Xie, D. Farkas, and E. J. Savino. *Modelling and Simulation in Materials Science and Engineering.*

[37] A. Ball and R. E. Smallman. *Acta Metall.*, 14:1517, 1966.

[38] C. H. Floyd and M. H. Loretto. *Physica Status Solidi*, 39:163, 1970.

[39] I. Baker and E. M. Schulson. *Metallurgical Transactions A*, 15A:1129, 1984.

[40] P. R. Munroe and I. Baker. *Scripta Metallurgica*, 23:495, 1989.

[41] A. Lasalmonie. *Journal of Materials Science*, 17:2419, 1982.

[42] M. H. Loretto and R. J. Wasilewski. *Philosophical Magazine*, 23:1311–1328, 1971.

[43] J. H. Schneibel, R. Darolia, D. F. Lahrman, and S. Schmauder. *Metallurgical Transactions A*, 24A:1363, 1993.

[44] M. J. Mills and D. B. Miracle. *Acta Metall. Mater.*, 41:85, 1993.

[45] D. B. Miracle. *Acta Metall. Mater.*, 39:1457, 1991.

[46] R.D. Noebe, R.R. Bowman, J.T. Kim, M. Larsen, and R. Gibala. In S.H. Whang, C.T. Liu, D.P. Pope, and J.O. Stiegler, editors, *High Temperature Aluminides and Intermetallics*, page 271. The Minerals, Metals and Materials Society, 1990.

[47] Horst Niehus, Werner Raunau, Karl Besocke, Ralf Spitzl, and George Comsa. *Surface Science Letters*, 225:8, 1990.

[48] P. Veyssiere. *Rev. Phys. Appl. Pairs*, 23:673, 1988.

[49] D. Farkas and C. Vailhe. *Journal of Materials Research*, 8, 1993. in press.

[50] V. Kumar, C.E.T. Goncalved da Silva, and J.L. Morán-López. *Physical Review B*, 23:2752, 1981.

[51] R. Pasianot, D. Farkas, and E. J. Savino. *Journal de Physique III*, 1:997, 1991.

[52] S. Takeuchi. *Philosophical Magazine A*, 41(4):541, 1980.

[53] M. Yamaguchi and Y. Umakoshi. *The Structure and Properties of Crystal Defects*, page 131, 1983.

[54] Z. Xie and D. Farkas. In *Proceedings of the Materials Research Society Symposium*, volume 288, page 305, 1993.

[55] Z. Xie and D. Farkas. *Journal of Materials Research.* in press.

[56] A. J. Bradley and A. Taylor. *Proc. R. Soc. Lond*, page 56, 1937.

[57] K. H. Hahn and K. Vedula. *Scripta Metallurgica*, 23:7, 1989.

[58] C.T. Liu. *Scripta Met.*, 25:1231, 1991. Viewpoint set No 17.

[59] R. A. Johnson. *Physical Review*, 145:423, 1966.

[60] G. L. Hall. *J. Phys. Chem. Solids*, 3:210, 1957.

[61] H. Kanzaki. *J. Phys. Chem. Solids*, 2:24, 1957.

[62] V. K. Tewary. *Adv.Phys.*, 22:757, 1973.

[63] E.J. Savino and D. Farkas. *Philosophical Magazine A*, 58, 1988.

[64] D. Farkas, E.J. Savino, P. Chidambaram, A.F. Voter, D.J. Srolovitz, and S.P. Chen. *Philosophical Magazine A*, 60:433, 1989.

[65] S. M. Kim. *Acta Metallurgica*, 40:2793, 1992.

[66] K. Vedula and P. S. Khadkikar. *High Temperature Alumides and Intermetallics*, page 197, 1990.

[67] D. Farkas and V. Rangarajan. *Acta Metallurgica*, 35:353, 1987.

[68] S. Gialanella, S. B. Newcomb, and R. W. Cahn. In A. R. Yavari, editor, *Ordering and Disordering in Alloys*, page 67. Elsevier Applied Science, 1992.

[69] P. R. Okamoto, L. E.Rehn, J. Pearson, R. Bhadra, and M. Grimsditch. *J. Less-Common Met.*, 141:349, 1974.

[70] S.P. Chen, A.F. Voter, and D.J. Srolovitz. *Physical Review Letters*, 57:1308, 1986.

[71] C. L. Fu and M. H. Yoo. In I. Baker, R. Darolia, J. D. Whittenberger, and M. H. Yoo, editors, *High Temperature Ordered Intermetallic Alloys V*, page 667. 1993.

[72] J. M. Koch and C. Koenig. *Philosophical Magazine*, 57:557, 1988.

[73] T. Khan, P. Caron, and S. Naka. In S. H. Whang, C. T. Liu, D. P. Pope, and J. O. Stiegler, editors, *High Temperature Alumides and Intermetallics*, page 219. TMS, Warrendale, PA 15086, 1990.

[74] K. Vedula and P. S. Khadkikar. In S. H. Whang, C. T. Liu, D. P. Pope, and J. O. Stiegler, editors, *High Temperature Alumides and Intermetallics*, page 197. TMS, Warrendale, PA 15086, 1990.

[75] M. Crimp, S. C. Tonn, and Y. Zhang. *Materials Science and Engineering A.* to be published.

[76] J. H. Westbrook. *J. Electro. Chem. Soc.*, 103:54, 1956.

[77] R. T. Pascoe and C. W. A. Newey. *Physica Status Solidi*, 29:357, 1968.

[78] P. Stadelmann. *Ultramicroscopy*, 21:131, 1987.

[79] R. D. Field, D. F. Lahrman, and R. Darolia. *Acta Metall. Mater.*, 39:2951, 1991.

[80] V. Vitek. In The Physical Society, editor, *Dislocations and Properties of Real Materials*, page 30. Arrowsmith, Bristol, 1985.

[81] T. A. Parthasarathy, S. I. Rao, and D. Dimiduk. *Phil. Mag.*, A 67:643, 1993.

[82] V. Vitek. *Philosophical Magazine A*, 58:193, 1988.

[83] M. S. Duesbury. *Proc. R. Soc. Lon., A*, 392:145, 1984.

Vita

The author, Zhao-Yang Xie, was born on August 28, 1958 in Shaanxi, China. He received both his B.S. degree in Physics in 1982 and M.S. degree in Metals Physics in 1985 at Northwestern Polytechnical University (NPU), Xi'an, China. Then he joined the Department of Applied Physics at NPU as a Lecturer. During eight years teaching and research at NPU, he was responsible for the undergraduate and graduate courses of the Department including quantum mechanics, thermodynamics and phase transitions in solids; and was involved in several research projects including liquid metals properties and non-equilibrium solidification, and martensitic and bainitic transformations in solids. He was awarded a Governmental Scholarship for research and study in the United States in 1989 as a Visiting Scholar. In 1990 he attended the PhD program in the Materials Engineering Science at Virginia Polytechnic Institute and State University, Blacksburg, Virginia.

The author has always believed that hard work and persistence can work wonders, and he has been trying to prove this premise with his own life. The author's career interests are in education, research, and development in physics and materials engineering.

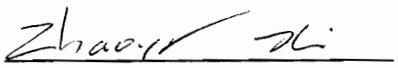

Zhao-Yang Xie